Controlling Thin-film Morphology and Incorporating Novel Semiconducting Molecules toward High Performance Organic Optoelectronic Devices

by

Byeongseop Song

A dissertation submitted in partial fulfillment
of the requirements for the degree of
Doctor of Philosophy
(Electrical Engineering)
in the University of Michigan
2018

Doctoral Committee:

Professor Jinsang Kim, Co-Chair
Professor L. Jay Guo, Co-Chair
Professor Anne J. McNeil
Professor Jamie D. Phillips

Byeongseop Song

bssong@umich.edu

ORCID iD: 0000-0002-4172-4457

ACKNOWLEDGEMENTS

First and foremost, I would like to thank my advisor, Jinsang Kim. He understood all of my academic concerns and led me to an independent researcher at the end of my Ph. D. He is not only an academic advisor but also a supportive teacher who gave me sincere advices. He showed what the enjoyable research is. Also, I am thankful to all members in Prof. Kim's group: Mounggon Kim, Jaehun Jung, Chen Li, Apoorv Shanker, Dohyun Kang, Yingying Zeng, Da Seul Yang, Ricardo Vazquez, Joonkoo Kang, Seong-Jun Yoon. Their extensive knowledge about chemistry and material science helped me to understand properties of organic materials.

Collaborations are another good way to produce excellent work: I acknowledge Dr. Chen Kong and Prof. McNeil for providing high-quality copolymer to fabricate high-efficiency polymer solar cells. They are very knowledgeable in controlling all aspects of polymer properties. And I appreciate professor L. Jay Guo, Jamie D. Phillips for serving my thesis committee.

Additionally, I appreciate Professor Stephen R. Forrest who established most of fundamentals in academic research throughout my first three years of Ph.D. His outstanding experiences and knowledge always makes me strive for thinking beyond simple experimental data. Forrest's group members including Cedric Rolin, Jeramy D. Zimmerman, Kyusang Lee, Jaesang Lee, Jongchan Kim, Quinn C. Burlingame, Xiao Liu, Yue Qu are happy to suggest new idea, analysis technique throughout my experiments.

Lastly, I appreciate to my family for their endless emotional support. And especially my wife, Doyeon Kim, sacrifices many aspects in her life here for my successful graduation. I would not be able to accomplish this without her.

Byeongseop Song

Ann Arbor, MI

January, 2018.

TABLE OF CONTENTS

ACKNOWLEDGEMENTS ...ii

LIST OF FIGURES vi

LIST OF TABLES xi

ABSTRACT xii

Chapter 1 Introduction to organic optoelectronic devices 1

1.1. Fundamental properties of organic semiconducting materials....1

1.2. Organic photovoltaics (OPV)....3

1.2.1. Structure of OPV....3

1.2.2. Current-voltage characteristics of OPV....5

1.2.3. Efficiency of OPV....7

1.3. Organic light emitting diode (OLED)....9

1.3.1. Device structure of OLED....9

1.3.2. Energy transfer....11

1.3.3. Color and efficiency of OLED....13

1.4. References....17

Chapter 2 Method 19

2.1. Growth technique of organic materials....19

2.1.1. Vacuum thermal evaporation....19

2.1.2. Organic vapor phase deposition....20

2.1.3. Spin-coating 21

2.2. Thin-film characterization method....22

2.2.1. Atomic force microscopy 22

2.2.2. X-Ray diffraction 24

2.2.3. Transmission electron microscopy....25

2.3. References……..…….28
Chapter 3 Effect of mixed layer crystallinity on the performance of organic photovoltaics…….29
3.1. Introduction…….29
3.2. Results & Discussion……..30
3.2.1. Performance of mixed heterojunction OPVs ……30
3.2.2. Morphology of DBP:C_{70} mixed layer ……..32
3.2.3. Optical and Electrical properties of DBP:C_{70} mixed layer ……..35
3.3. Conclusion ……..37
3.4. Experimental details ……...38
3.5. References ……..40
Chapter 4 Reliability of organic photovoltaics grown via organic vapor phase deposition…….44
4.1. Introduction ……44
4.2. Results & Discussion ……..45
4.2.1. Morphological degradation of Bphen ……..45
4.2.2. Performance change of mixed heterojunction OPVs with Bphen buffer …48
4.2.3. Origin of electrical shorts and V_{oc} changes in OPVs ……...50
4.3. Conclusion ……..54
4.4. Experimental details……54
4.5. References ...……...57
Chapter 5 Control of morphology in electron-conducting buffers via organic vapor phase deposition ...……..……61
5.1. Introduction ...……61
5.2. Results & Discussion ……..62
5.2.1. Morphology of BP4mPy:C_{60} electron-conducting buffer ……63
5.2.2. Electrical property of BP4mPy:C_{60} electron-conducting buffer ……..65
5.2.3. Performance of mixed heterojunction OPVs with BP4mPy:C_{60} buffer…….67
5.2.4. Molecular dynamic simulation of BP4mPy:C_{60} buffer……68
5.3. Conclusion……...72
5.4. Experimental details……73
5.5. References ……..75
Chapter 6 Effect of copolymer in polymer bulk-heterojunction organic photovoltaics ……78

6.1. Introduction……78
6.2. Results & Discussion ……..……79
6.2.1. Synthesis of thiophene-fullerene functionalized copolymer……80
6.2.2. Performance of polymer bulk heterojunction OPVs with copolymer……..80
6.2.3. Morphology of P3HT:PCBM with copolymer……82
6.2.4. V_{oc}, *FF* changes in polymer bulk heterojunction OPVs with copolymer …..85
6.3. Conclusion ……..88
6.4. Experimental details……89
6.5. References……...93
Chapter 7 Organic light-emitting diode (OLED) from metal-free organic phosphor……95
7.1. Introduction ...……95
7.2. Results & Discussion ……..96
7.2.1. Synthesis and photo-physical property of BrPFL-TFK ……..97
7.2.2. Spectrum of BrPFL-TFK doped in various host materials……99
7.2.3. Performance of OLED with the purely organic emitter BrPFL-TFK…….103
7.3. Conclusion…….105
7.4. Experimental details……..106
7.5. References…….109
Chapter 8 Outlook……111
8.1. Roll-to-roll fabrication of all vacuum-deposited organic photovoltaics……111
8.2. Increase lifetime of OLED employing a thick emissive layer……..113
8.3. Possible research direction in metal-free organic phosphorescent OLED……116
8.4. References ...…….120

LIST OF FIGURES

Figure 1.1. Schematic illustration of OPV device structure ……..…… 4
Figure 1.2. Dark *J-V* characteristics of (a) CuPc:C_{60} (b) SubPc:C_{60} OPVs recorded for *T* = 296, 275, 247, 218, 193, 171, 155, 145, 128, 114 K ……..…… 6
Figure 1.3. General *J-V* characteristics of OPV under dark and light illumination ……... 8
Figure 1.4. Standard AM 1.5G solar spectrum ...……... 8
Figure 1.5. Standard structure of OLED ...…….. 10
Figure 1.6. The standardized spectral response of the three color-sensitive photoreceptors cell.. 13
Figure 1.7. CIE color space (x, y) diagram…… 14
Figure 1.8. Photopic response curve…….. 15
Figure 2.1. Schematic diagram of vacuum thermal evaporation…….…….. 20
Figure 2.2. Schematic diagram of organic vapor phase deposition system……...…… 21
Figure 2.3. Schematic representation of atomic force microscope…… 23
Figure 2.4. AFM image of 100 nm pentacene thin-film ...…… 23
Figure 2.5. Schematic diagram of Bragg-Brentano (θ-2θ) configuration in XRD measurement.. 24
Figure 2.6. Schematic cross section of transmission electron microscope ...…… 26
Figure 2.7. TEM images of photoactive layers of new (left) and old (right) batches of PDPPTPT polymer with PCBM ……..…….. 27
Figure 3.1. Power conversion efficiency (*PCE*), fill factor (*FF*), and short-circuit current density (J_{sc}) of DBP:C_{70} mixed heterojunction devices grown by VTE and OVPD as functions of mixed layer thickness ……..…….…….. 31
Figure 3.2. (left) Current density (*J*) versus voltage (*V*) characteristics under 1 sun illumination for 60 nm or 100 nm active layer thickness grown by VTE and OVPD, respectively. (right) External and internal quantum efficiencies as a function of wavelength (λ) of the devices …… 32

Figure 3.3. Atomic force microscopy (AFM) images of 60 nm thick DBP:C_{70} (1:10 ratio) Films grown by (top-left) VTE and (top-right) OVPD on a Si substrate. Selected area electron diffraction (SAED) patterns of DBP:C_{70} films grown by (bottom-left) VTE and (bottom-right) OVPD ……..…..…..……. 34

Figure 3.4. (left) Extinction coefficient (k) of DBP:C_{70} grown by VTE and OVPD as a function of wavelength (λ). (right) Natural logarithm of absorption coefficient, log(α), of DBP:C_{70} films grown by VTE and OVPD …….……. 35

Figure 3.5. (left) Fits of forward-biased J-V characteristics of the devices in Figure 3.1 using the ideal diode equation for 60 nm and 100 nm thick active layer OPVs grown by VTE and OVPD, respectively. (right) Series resistance (R_s) and fill factor (FF) of the devices …….....…….……. 37

Figure 4.1. (a) Atomic force (AFM) and optical microscope images of an 8 nm thick Bphen film grown by vacuum thermal evaporation (VTE) on ITO/MoO_3 (10 nm)/ 1:10 (by vol.) DBP:C_{70} (60 nm grown by VTE) and after aging for (b) 12 hr, (c) 25 hr, and (d) 75 hr. (e) Similar images of an 8 nm thick Bphen film grown by VTE on an analogous structure but with the DBP:C_{70} grown to 200 nm thickness by organic vapor phase deposition (OVPD) and (f)-(h) after again for the same durations ……..……..……..… 46

Figure 4.2. (a) Bragg-Brentano Cu-Kα X-ray diffraction (XRD) measurement of 1:10 (by vol.) DBP:C_{70} (100 nm thick) film grown by (I) VTE and (II) OVPD on sapphire substrate. (b) XRD data of the 50 nm thick Bphen on the same structure after aging for 75 hr …...……47

Figure 4.3. Current density-voltage (J-V) characteristics of DBP:C_{70} mixed heterojunction organic photovoltaic (OPV) cells with an 8 nm thick Bphen blocking layer and a 100 nm thick Ag cathode .....…….. 49

Figure 4.4. Fluorescence microscope image of glass/12 nm thick tris(8-hydroxyquinolinato) aluminum (Alq_3)/1:10 (by vol.) DBP:C_{70} (60 nm) grown by (a) VTE or (b) OVPD/Bphen(8 nm)/Ag(100 nm) after aging 75 hr. (c) Energy dispersive spectra (EDS) of DBP:C_{70} (60 nm thick grown by VTE or OVPD)/Bphen (8nm)/Ag(60 nm) films on a Si substrate after aging 75 hr ...……...……..51

Figure 4.5. Capacitance-voltage ($1/C^2$ *vs*. V) characteristics of (a) 60 nm thick VTE-grown, (b) 200 nm thick VTE-grown, and (c) 200 nm thick OVPD-grown DBP:C_{70} active layer devices before and after aging for 250 hr ...…….52

Figure 4.6. Aging characteristics of three DBP:C_{70} mixed heterojunction devices (60 nm thick, 200 nm thick active layer grown by VTE, and 200 nm thick active layer grown by OVPD) with an 8 nm thick Bphen blocking layer and a 100 nm thick Ag cathode ... 53

Figure 5.1. Atomic force microscope (AFM) images of 10 nm thick C_{60} films grown by organic vapor phase deposition (OVPD) at (a) 0.17 torr (b) 0.28 torr (c) 0.49 torr (d) 0.82 torr and (e) vacuum thermal evaporation (VTE). AFM image of 10 nm thick (f) BP4mPy and (g) BP4mPy:C60 (1:1 vol.) grown by OVPD at 0.28 torr ……... 63

Figure 5.2. Atomic force microscope (AFM) images of 10 nm thick BP4mPy:C_{60} (1:1 vol.) films grown by organic vapor phase deposition (OVPD) at (a) 0.17 torr (b) 0.49 torr (c) 0.82 torr. (d) AFM image of 200 nm thick BP4mPy:C60 (1:1 vol.) grown by OVPD at 0.28 torr ……..…… 64

Figure 5.3. X-ray diffraction (XRD) using the Cu-Kα line in the Bragg-Brentano configuration of 200 nm thick (a) C_{60} and (b) BP4mPy:C_{60} (1:1 vol.) on sapphire substrates grown by OVPD at four different growth pressures (0.17, 0.28, 0.49, 0.82 torr) ..…….65

Figure 5.4. Current density-voltage characteristics of sapphire/Al (100 nm)/BP4mPy:C_{60} (1:1 vol., 200 nm)/NTCDA (10 nm)/LiF (1.5 nm)/Al (100 nm) electron-only devices ……..……...66

Figure 5.5. (a) Current density-voltage characteristics of DBP:C_{70} planar mixed heterojunction devices with BP4mPy:C_{60} (1:1 vol., 10 nm) buffers grown by VTE or OVPD at different growth pressures (0.17, 0.28, 0.49, 0.82 torr). (b) Fill factor (*FF*) variation of the devices in (a) depending on the growth pressure ……..68

Figure 5.6. Molecular dynamic simulation results of an ensemble of 12 BP4mPy and 32 C_{60} molecules after simulated annealing with effective molecular kinetic energies of (a) δE_{kin} = 4.5 meV, (b) 7.4 meV, (c) 13 meV, (d) 21.7 meV ….…….. 70

Figure 5.7. (a) Potential energy of the simulated molecular configuration annealed at T = 576 K (corresponding to P_2) as a function of simulation time. (b) Normalized peak intensities at 10.1 Å and 14.1 Å in radial distribution function (RDF) as a function of pressure in BP4mPy:C_{60} blends ……..…… 71

Figure 6.1. Synthetic scheme of thiophene-fullerene functionalized copolymer …… 81
Figure 6.2. Current density-voltage (*J-V*) characteristics of (a) P3HT:PCBM bulk-heterojunction OPVs and (b) the OPVs with copolymer under different thermal annealing time (0, 15, 45, 90 min). Performance of the OPVs depending on thermal annealing time is summarized: (c) current density *Jsc*, (d) open-circuit voltage *Voc*, (e) fill factor *FF*, and (f) power conversion efficiency *PCE* ……..……..82
Figure 6.3. AFM phase image of (a) 180 nm thick P3HT:PCBM or (b) 180 nm thick P3HT:PCBM with 8 wt% copolymer on ITO/ZnO (40 nm) substrate. Optical microscopy image of (c) 180 nm thick P3HT:PCBM or (d) P3HT:PCBM with 8 wt% copolymer on glass substrate after 90 min of thermal annealing at 150 ºC ……...83
Figure 6.4. Conductive-AFM (c-AFM) image of 180 nm thick P3HT:PCBM on (a) ITO/MoO_3 (20 nm) or (b) ITO/ZnO (40 nm) substrate. C-AFM image of 180 nm thick P3HT:PCBM with 8 wt% copolymer on (c) ITO/MoO_3 (20 nm) or (d) ITO/ZnO (40 nm) substrate ……..……84
Figure 6.5. c-AFM image of 180 nm thick P3HT:PCBM with 12 wt% copolymer on (a) ITO/MoO_3 (20 nm) or (b) ITO/ZnO (40 nm) substrate ……...……...……..85
Figure 6.6. Series resistance (R_s) of P3HT:PCBM and P3HT:PCBM with 8 wt% copolymer bulk heterojunction OPVs under different thermal annealing time …….. 86
Figure 6.7. (a) Cyclic voltammetry (CV) curve of copolymer in acetonitrile solution. The inset is the CV curve of ferrocene as a standard reference at a scan rate of 50 mV/s. (b) Absorption of copolymer thin-film measured by UV-vis spectrometer ...…..…... 87
Figure 6.8. Dark *J-V* characteristics of P3HT:PCBM and P3HT:PCBM with 8 wt% copolymer bulk heterojunction OPVs after 45, 90 min of thermal annealing …….. 88
Figure 6.9. Synthetic scheme of sub units in thiophene-fullerene functionalized copolymer 90
Figure 7.1. (a) Synthetic scheme of 1-(7-bromo-9,9-diphenyl-9H-fluoren-2-yl)-2,2,2-trifluoroethan-1-one (BrPFL-TFK). (b) (top) Lowest unoccupied molecular orbital (LUMO) distribution of BrPFL-TFK and (bottom) highest occupied molecular orbital (HOMO) distribution of BrPFL-TFK (c) UV-vis absorption, fluorescence, and phosphorescence spectra of BrPFL-TFK ……...……97
Figure 7.2. Cyclic voltammetry (CV) curve of BrPFL-TFK molecules in acetonitrile solution ..98

Figure 7.3. Energy level diagram of materials used in organic light emitting-diode (OLED) devices ……...……..……..100
Figure 7.4. (a) Photoluminescence (PL) spectra of a 50 nm thick CBP, mCP, and PPT film having 2% BrPFL-TFK. Electroluminescent spectra of OLED devices with 2% BrPFL-TFK doped in (b) CBP and (c) mCP with a TPBi or BP4mPy electron-transporting layer, and (d) PPT …...……..…….…..101
Figure 7.5. Electroluminescent spectra of OLED devices with BrPFL-TFK doped in PPT host emissive layer under different doping concentration of BrPFL-TFK .....……..102
Figure 7.6. (a) Current density-voltage-luminance (*J-V-L*) characteristics of OLED devices having 2% BrPFL-TFK doped in CBP (D1) and mCP with TPBi (D2-a) or BP4mPy (D2-b) as the electron-transporting layer, and PPT (D3). (b) External quantum efficiency-current density (*EQE-J*) plot of the four devices …….104
Figure 7.7. (a) *J-V* characteristic of hole-only device for D3 based on the following structure: ITO (UV Ozone-treated)/15% of MoO_3 doped in mCP (20 nm)/BrPFL-TFK (5 nm)/x% of BrPFL-TFK doped in PPT (20 nm)/PPT (40 nm)/MoO_3 (10 nm)/Al (100 nm). (b) *J-V* characteristic of electron-only device for D3 based on the following structure: ITO (untreated)/BrPFL-TFK (5 nm)/x% of BrPFL-TFK doped in PPT (20 nm)/PPT (40 nm)/LiF (1 nm)/Al (100 nm) ……...…… 104
Figure 8.1. Schematic diagram of the multi-chamber R2R deposition system ....……. 112
Figure 8.2. (a) Chemical structure of the host mCBP and phosphorescent guest $Ir(dmp)_3$ used in the emissive layer of the OLED. (b) Structure of the three OLEDs. HATCN, NPD, Alq_3 are used for hole injection layer, hole transporting layer, electron transporting layer, respectively ……...……. 115
Figure 8.3. Chemical structure of (a) 1-(7-bromo-9,9-diphenyl-9H-fluoren-2-yl)-2,2,2-trifluoroethan-1-one (BrPFL-TFK) and (b) A few purely organic phosphors having the fluorene core with various functional groups .....…….. 117
Figure 8.4. The external quantum efficiency versus current density characteristics of the $Eu(TTA)_3$phen:CBP device ……...…….. 118
Figure 8.5. Molecular structure of host materials (CBP, CBP-Br2, CBP-Br4) and guest material (4CzIPN) [9] …….…… 119

LIST OF TABLES

Table 1.1. A comparison of properties in organic and inorganic materials ...……3

Table 3.1. Interplanar d-spacings of OVPD grown DBP:C_{70} films …….……33

Table 4.1. Crystallographic data for Bphen/DBP:C_{70} ……..……48

Table 4.2. Performance of DBP:C_{70} mixed heterojunction OPVs grown by VTE or OVPD …...50

Table 5.1. Zero-field mobility, μ_0, and field-activation parameter, γ, of BP4mPy:C_{60} mixed layers under different growth conditions …… 67

Table 5.2. Performance of DBP:C_{70} planar mixed heterojunction OPVs with 10 nm thick BP4mPy:C_{60} compound buffer layers ……..69

Table 8.1. OLED performance chart from Idemitsu Kosan Co, Ltd …….. 114

ABSTRACT

Organic optoelectronic devices have been widely used in display, energy-storage, and consumer electronics. Insightful understanding on material properties, device architecture, and fabrication processes is inevitable to improve the performance of organic optoelectronic devices. My PhD research focuses on improving the performance of organic photovoltaics (OPV) and organic light-emitting diode (OLED) through the systematic processing and material design.

The first part of the dissertation describes how to construct a highly conductive morphology of mixed donor:acceptor heterojunction. Organic vapor phase deposition (OVPD) was utilized to enhance crystallinity of C_{70} acceptor in the mixed tetraphenyldibenzoperiflanthen (DBP):C_{70} thin-film. Forming the face-center-cubic (fcc) structure of C_{70} facilitated charge extraction, thereby improving fill factor (*FF*) of the corresponding OPVs.

The second part presents the study on the morphological stability and reliability of OPVs. The cathode buffer, bathophenanthroline (BCP), undergoes significant morphological degradation. This morphological degradation was successfully suppressed by making the underlying DBP:C_{70} layer rougher via the moving N_2 carrier gas in OVPD. The open-circuit voltage (V_{oc}) of the obtained heterojunction OPVs of DBP:C_{70} grown by OVPD experienced a negligible drop (< 3 % change) while the equivalent OPVs grown by VTE showed a significant decrease in V_{oc} from 0.91±0.01 *V* to 0.74±0.01 after 1 Sun illumination for 250 h.

The third part explains a more precise way to control the morphology of organic mixed layer. It was found that increase in the growth pressure of OVPD induced reorganization of molecules to form the equilibrium morphology. The morphology of the electron-filtering buffer layer of 3,5,3′,5′-tetra(m-pyrid-3-yl)phenyl[1,1′]biphenyl (BP4mPy):C_{60} was optimized to achieve the highest electron mobility by means of the control of the growth pressure. Consequently, the resulting OPVs with optimized BP4mPy:C_{60} buffer showed *FF* = 0.65±0.01 and a much higher

PCE = 8.0±0.2 % compared to *PCE* = 6.6±0.2 % of the equivalent OPVs with the same composition buffer layer grown by VTE.

The fourth part summarizes the effects of the inclusion of novel block-copolymers on the performance of the polymer bulk-heterojunction photovoltaic cells. The block-copolymers were composed of thiophene units with and without a dangling phenyl-C61-butyric acid methyl ester (PCBM) side chain. The added copolymer into the poly(3-hexylthiophene) (P3HT): PCBM active layer resulted in greatly improved thermal stability of P3HT:PCBM. Furthermore, electron conductivity also increased since the fullerene units of the copolymers contribute to the formation of a percolation pathway for electron transport. While *PCE* of conventional P3HT:PCBM bulk-heterojunction solar cells decreases significantly from 2.6±0.2 to 1.2±0.2% after 90-min of thermal annealing, the equivalent OPVs with the copolymer shows a much smaller decrease in *PCE* from 3.1±0.2% to 2.7±0.2%.

The last section of this dissertation covers the design of phosphorescent OLED employing a metal-free purely organic phosphor. Owing to their much longer triplet lifetime in the millisecond regime compared to microseconds of organometallics, a more careful consideration should be given in the device design. The requirements for the host materials in metal-free purely organic phosphor OLEDs are identified to be a high triplet energy, suitable HOMO and LUMO energy levels, and large spectral overlap with the absorption of the phosphors. Systematic investigation on various host molecules, electron transporting molecules, and the layer thickness of each layer allows us to demonstrate an optimized phosphorescent OLED having an external quantum efficiency (EQE) of 2.5 % at 1 mA/cm^2.

Chapter 1

Introduction to organic optoelectronic devices

The development of organic semiconductor materials draws industrial as well as academic interests owing to their multiple advantageous properties and a large molecular design window. Tunable optoelectronic properties, cost-effectiveness, and processing feasibility on flexible substrates make organic materials more attractive in optoelectronic device applications. This chapter as an introductory chapter of the dissertation discusses the fundamental properties of organic semiconducting materials and the device physics and figure of merits of the two most widespread organic optoelectronic devices, organic photovoltaics (OPV) and organic light-emitting diode (OLED).

1.1 Fundamental properties of organic semiconducting materials

Organic materials generally refer to materials made up of carbon and hydrogen atoms with some heteroatoms (either sulfur, oxygen, or nitrogen). Organic materials have a unique property compared to their inorganic counterparts due to the different bonding type. Organic molecules are bound by Van der Waals forces [1]. Van der Waals forces are an electrostatic interaction between molecules. Induced dipole moment of molecules attracts surrounding molecules when they are within a close distance (few nm). The strength of Van der Waals bond is much weaker than a covalent bond (sharing electron pairs between atoms) or an ionic bond (Coulombic interaction

between charged ion) through which inorganic materials are held together. Therefore, density of states in organic materials are discrete molecular orbitals instead of the continuous energy band in inorganic compounds. Accordingly, the charge transport mechanism is hopping-base transport between molecular orbital levels, whereas the charge transport in inorganic compounds is through a well-defined energy band [2]. The resulting charge mobility of organics is usually less than 0.1 $cm^2/(V\cdot s)$ compared to that of inorganic materials, which is more than 1000 $cm^2/(V\cdot s)$. The thickness of each organic layer is usually < 200 nm due to this mobility constraint [3]. Dielectric constants of inorganics are usually large ($11.9\varepsilon_0$ for Si and $13.2\varepsilon_0$ for GaAs, where $\varepsilon_0 = 8.854\times10^{-14}$ F/cm is the permittivity of free space) owing to the delocalized nature of the carriers, while dielectric constants of organics are small (usually $3\varepsilon_0$ - $4\varepsilon_0$) [1]. The difference in dielectric constants leads to the difference in exciton binding energy. An analytical expression of the exciton binding energy can be obtained after solving Schrödinger's equation of the electronic state in an atom.

$$E_b = \frac{e^2 a_0}{(m^*/m)(a_0^*)^2} \tag{1.1}$$

$$a_0^* = \mathrm{m}/m^* \varepsilon a_0 \tag{1.2}$$

where, E_b is the exciton binding energy, a_0^* is the exciton radius, e is the elementary charge, m is the electron mass, m^* is the effective reduced mass, ε is the dielectric constant, and a_0 is the Bohr radius for the hydrogen atom. The exciton radius of organic materials is ~ 1 nm with a large binding energy (0.1 – 1 eV), called Frenkel exciton. In contrast, excitons in inorganic compounds have a small binding energy (typically less than $kT = 25.7\ meV$) with a nearly 10 nm of exciton radius, called Wannier-Mott excitons [4]. The difference in material properties between organic materials

and inorganic compounds is summarized in Table 1.1. A large exciton binding energy of organic semiconducting materials (by either light absorption or direct carrier injection) plays a critical role in the operation of organic optoelectronic devices.

Table 1.1 A comparison of properties in organic and inorganic materials

Property	Organics	Inorganics
Bonding type	Van der Waals	Covalent or Ionic
Charge transport	Polaron Hopping	Band Transport
Mobility	< 0.1 cm^2/V·s	~ 1000 cm^2/V·s
Exciton binding energy	0.1-1 eV	< 100 meV
Exciton Radius	~10Å	~100Å

1.2. Organic photovoltaics (OPV)

Organic photovoltaics (OPV) are one major branch in organic optoelectronic devices. OPV utilizes photon energy from sun to populate excitons in the organic photo-active layer, collecting charge carriers at each electrode after the exciton disassociation within the organic photo-active layer. First proof-of-concept of OPV was demonstrated by C. W. Tang with 1 % power conversion efficiency [5]. After tremendous efforts in the development of new materials and device architecture, the power conversion efficiency of OPVs exceeds 10 % [6,7].

1.2.1. Structure of OPV

A standard OPV consists of an anode, an anode buffer layer, an organic donor:acceptor (D:A) photo-active layer, a cathode buffer layer, and a cathode as shown in Figure 1.1. Indium tin oxide (ITO) is widely used as an anode owing to its high transparency and conductivity. The anode

buffer layer is usually transparent transition-metal oxide (MoO_3, ZnO, NiO, etc.) having high conductivity of charge carriers. The D:A photo-active layer is the most important layer where the generation and disassociation of excitons and charge transport occur. Once excitons are generated after absorption of photons, the excitons are dissociated at the interface between the donor and the acceptor due to their energy level difference. The separated charges through exciton dissociation are transported towards each buffer layer. Therefore, organic materials having high absorbance, high carrier mobility, and suitable energy levels are required for the D:A layer. The cathode buffer layer can be made of either organic materials or a transition metal oxide. Organic materials are generally more preferred in small-molecule OPVs because of their readily tunable energy levels. Al or Ag metal is used as a cathode based on their high reflectivity and proper work-function.

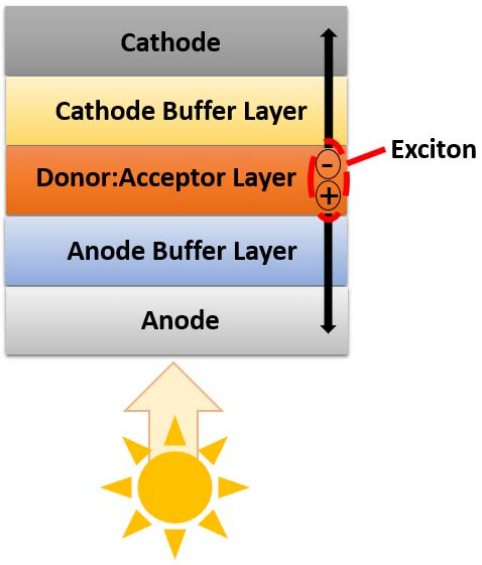

Figure 1.1. Schematic illustration of OPV device structure.

Mainly, two common architectures have been investigated for the D:A layer. The first one is the bilayer (planar) heterojunction where donor and acceptor organic layers are stacked

consecutively. The efficiency of these bilayer heterojunction OPVs is limited by the exciton diffusion length of ~ 10 nm for most organic materials. Even if donor or acceptor materials have high carrier mobility and absorption coefficient, the layer thickness beyond the exciton diffusion length of organic semiconductors does not produce any more photo-current because the excitons beyond the exciton diffusion length will recombine before they reach the D:A interface [8]. The other architecture is the heterojunction of mixed D:A having the donor and acceptor-rich domains within the exciton diffusion length. The D:A mixed layer thickness is not limited to the exciton diffusion length any more but to the light penetration length and the resistance of the D:A layer. The charge collection and transport efficiencies become more important in the D:A mixed heterojunction OPV [9].

1.2.2. Current-voltage characteristics of OPV

Historically, a physical model of inorganic photovoltaics was established first to explain the current-voltage (*J-V*) characteristics of the device. The ideal-diode equation, called Shockley equation, of inorganic photovoltaics is as follows:

$$J(V) = J_s[exp(\frac{V-JR_s}{nkT/q}) - 1] - J_L \quad (1.3)$$

Here, J_s is the reverse-bias saturation current, R_s is the series-resistance of the device, n is the diode ideality factor, k is Boltzmann constant, T is temperature, q is elementary charge, and J_L is the current generated from the absorption of photons (photo-current). This model can also be applied to describe *J-V* characteristics of organic photovoltaics due to its simplicity. However, Giebink *et al*. showed that it failed to fit experimental *J-V* characteristic of OPVs at different operating

temperatures [10]. After including the excitonic nature of OPVs in the physical model, the original equation was modified to the ideal-diode equation for organic D:A heterojunction:

$$J(V) = J_{sD}[exp(\frac{V-JR_S}{n_D kT/q}) - 1] + J_{sA}[exp(\frac{V-JR_S}{n_A kT/q}) - 1] - J_L \quad (1.4)$$

where $J_{sD(A)}$ is the reverse-bias saturation current on the donor (acceptor) side, $n_{D(A)}$ is the ideality factors considering the trap-limited recombination in the donor (acceptor) side. The two exponentials in Equation (1.4) are for the polaron pair recombination occurred at both donor and

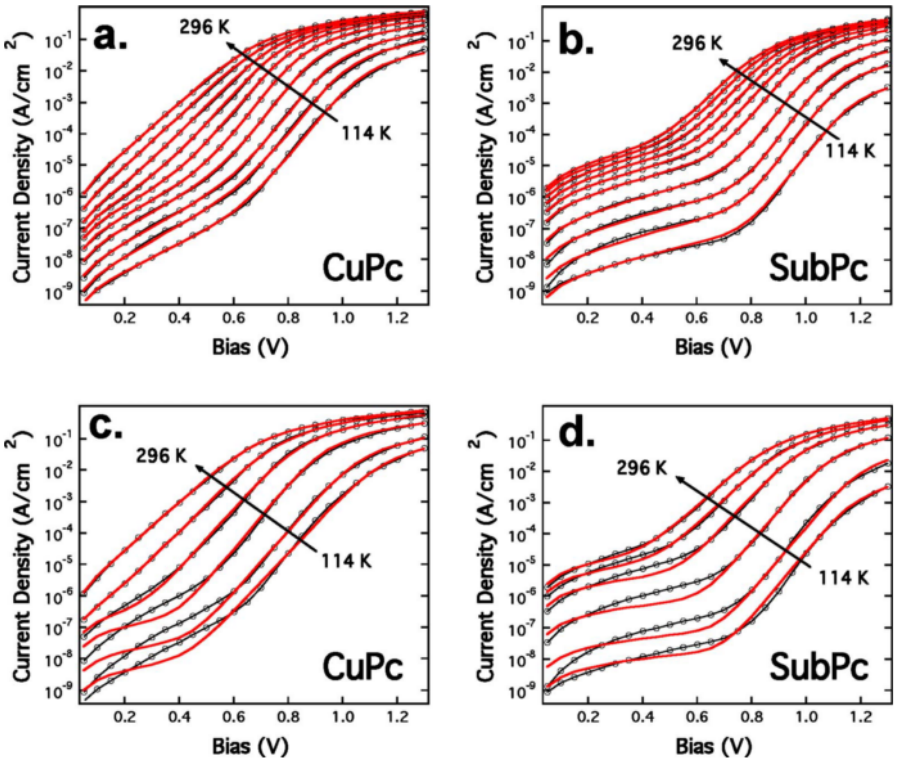

Figure 1.2. Dark *J-V* characteristics of (a) CuPc:C_{60} (b) SubPc:C_{60} OPVs recorded for T = 296, 275, 247, 218, 193, 171, 155, 145, 128, 114 K. Red lines indicate fits to Equation (1.4). Both data sets are refit using Equation (1.3) in (c) and (d), where the difference between data and theory is most pronounced at low voltage and temperature. [10]

acceptor. As shown in Figure 1.2, the Giebink's model successfully describe *J-V* characteristics of copper phthalocyanine (CuPc):C_{60}, boron subphthalocyanine chloride (SubPc):C_{60} heterojunction OPVs, whereas the original ideal-diode model does not.

1.2.3. Efficiency of OPV

Figure 1.3 shows general *J-V* characteristics of OPV under light illumination. The maximum electrical power generated from OPV is the maximum area of the rectangle defined by $J(V) \times V$ in fourth quadrant of the *J-V* curve. This is the maximum power point (MPP) of OPV, which is $P_{m,out} = J_{mp} \times V_{mp}$. Geometrical factor, called fill factor (*FF*), is defined by squareness of *J-V* characteristic in the fourth quadrant:

$$FF = \frac{P_{m,out}}{J_{sc}V_{oc}} = \frac{J_{mp}V_{mp}}{J_{sc}V_{oc}} \tag{1.5}$$

In the physical point of view, *FF* represents the quality of the diode. It is affected by charge transport properties of OPV (series resistance), molecular recombination, and manufacturing defects (shunt resistance). The power conversion efficiency (*PCE*) of the device is defined by the ratio of the maximum electrical power from OPV to the incident optical power (P_0).

$$\eta = \frac{P_{m,out}}{P_0} = \frac{J_{sc}V_{oc}FF}{P_0} \tag{1.6}$$

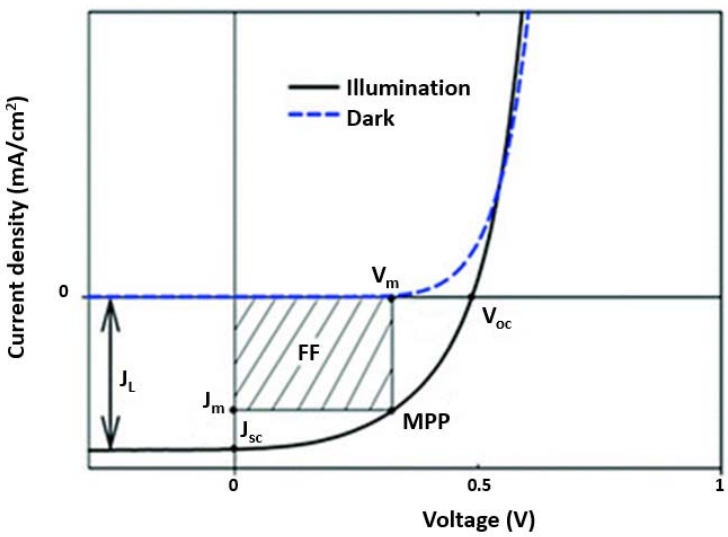

Figure 1.3. General *J-V* characteristics of OPV under dark and light illumination. Several figures of merits are included.

For standard measurement, AM 1.5G solar spectrum (air mass 1.5) is used as an incident light spectrum. AM 1.5G spectrum stands for the solar irradiation at 48.19 degree solar zenith angle with a total power density of 100 mW/cm^2. Figure 1.4 shows the standard AM 1.5G solar spectrum.

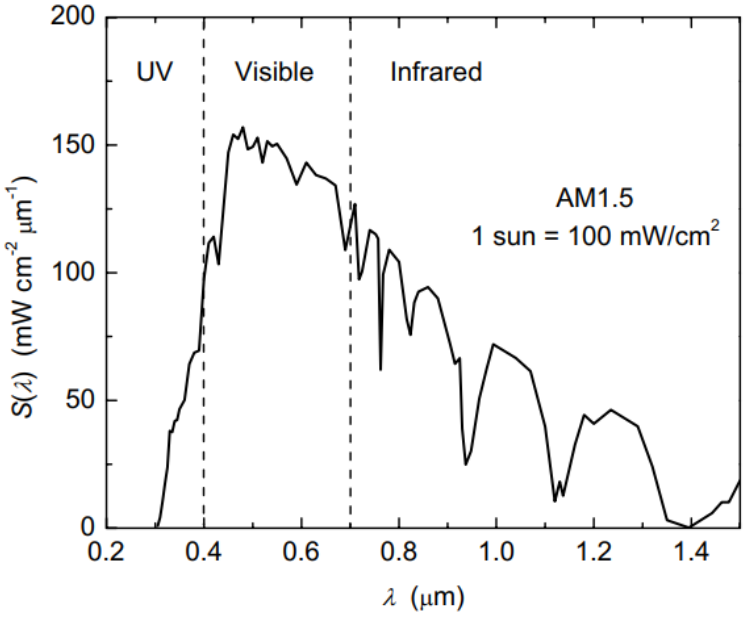

Figure 1.4. Standard AM 1.5G solar spectrum.

Practically, solar simulators with a known light source (Xenon arc lamp, mercury lamp, tungsten lamp, etc.) are used to analyze the performance of OPV. Corrections of the incident power and spectral mismatch of solar simulators compared to AM 1.5G solar spectrum are needed to evaluate OPV cells accurately.

1.3. Organic light emitting diode (OLED)

Organic light emitting diode (OLED) in the display technology is the most successful demonstration of organic optoelectronic devices. OLED operates as electrons and holes are injected to form excitons in organic emissive materials, and excitons radiatively decay to generate photons with a specific wavelength that is determined by the bandgap of the organic emissive materials. Since Tang and VanSlyke demonstrated the first organic electroluminescent devices [11], significant breakthrough to overcome fundamental challenges and limits and realize high efficiency OLEDs was made by Forrest and Thompson through rational design and utilization of organometallic phosphor compounds [12, 13]. Nowadays, researches in OLED put more emphasis on extending the device lifetime of particularly blue OLED due to the roll-off issue of the devices originated from the high exciton energy [14–16].

1.3.1. Device structure of OLED

The standard structure of OLED consists of an anode, a hole injection layer (HIL), a host transport layer (HTL), an electron blocking layer (EBL), an emissive layer (EML), an electron transport layer (ETL), a hole blocking layer (HBL), an electron injection layer (EIL), and a cathode as shown in Figure 1.5. HIL and EIL facilitate the injection of holes and electrons from the anode and cathode, respectively. Charge transport layers (HTL, ETL) are responsible for transport of

carriers from each injection layer to EML. Further HBL, EBL are needed to confine the formation of excitons within EML because most of organic materials have asymmetric hole and electron mobilities. The lowest unoccupied molecular orbital (LUMO) level of EBL needs to be at least equal or shallower than that of EML to effectively block electrons from EML. In the same way, the highest occupied molecular orbital (HOMO) level of HBL needs to be at least equal or deeper than that of EML to effectively block holes from EML. The above-mentioned requirements can be met by a single or multilayer design depending on materials' electrical properties and energy level alignments.

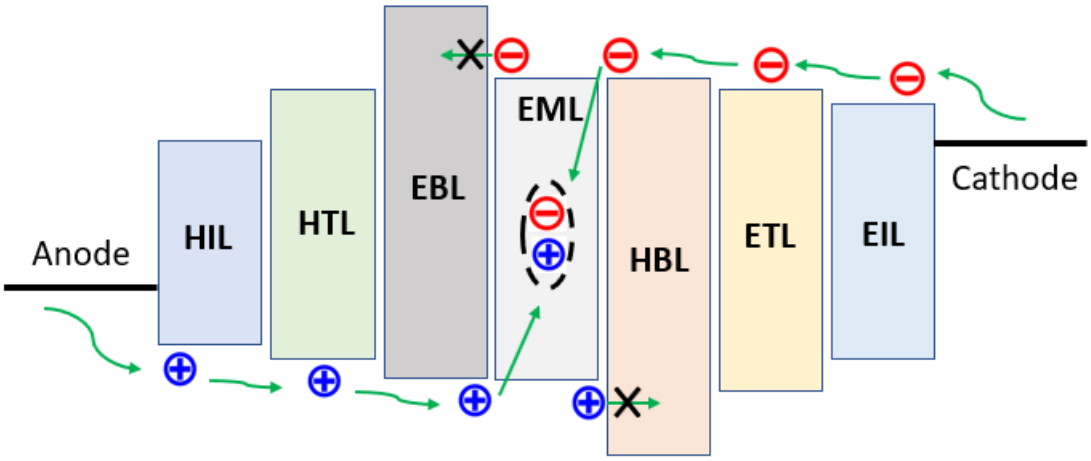

Figure 1.5. Standard structure of OLED. Transitions of electrons and holes are indicated.

EML comprises two different organic materials, called the host-guest system. The emitting material (guest) is diluted as a minor component into the major host material having a high triplet exciton energy. A high doping concentration of guest molecules results in self-quenching due to the formation of aggregation and consequent nonradiative quenching. Typically, the doping concentration ranges from 2 % to 20 % (by vol.) depending on the charge transport property and

non-radiative relaxation of the guest material. The injected electrons and holes can form either a singlet exciton (spin anti-symmetric, spin number = 0) or a triplet exciton (spin symmetric, spin number = 1) within the EML. According to the fundamental quantum statistics, the probability of triplet-exciton formation is three times higher than that of singlet-exciton [3]. Therefore, fluorescent OLEDs using singlet excitons have a fundamental limitation in its efficiency compared to phosphorescent OLEDs utilizing triplet excitons. The maximum internal quantum efficiency (IQE) of fluorescent OLEDs is only 25 %, while that of phosphorescent OLEDs is 100 % by transferring singlet excitons to triplet excitons via intersystem crossing [17].

1.3.2. Energy transfer

There are two types of energy transfer mechanism depending on the distance between excitons. Förster resonant energy transfer (FRET) is a long-range electromagnetic dipole-dipole interaction. Spins should be conserved during the energy transfer, allowing only transfer from excited singlet to ground state singlet. The FRET rate is expressed as [18]:

$$k_{FRET} = \frac{1}{\tau_D}\left(\frac{R_0}{R}\right)^2 \tag{1.7}$$

where τ_D is the lifetime of the host molecule, R is the distance between the host molecule and guest molecule, and R_0 is Förster radius defined as:

$$R_0^6 = 8.77 \cdot \Phi_D \kappa^2 \int I_D(\lambda)\varepsilon_A(\lambda)\lambda^4 d\lambda \tag{1.8}$$

Here, Φ_D is the quantum yield of the host molecule's fluorescence, κ is the orientation factor of the dipoles, I_D is the emission intensity of the host, and ε_A is the absorption coefficient of the guest. The FRET efficiency is proportional to the spectral overlap between the emission of the host and the absorption of the guest. A typical Förster radius is from 5 to 10 nm, which is effective in most host-guest mixtures in EML [19].

The other energy transfer mechanism is a short-range coherent transfer of excitons by simultaneous charge exchange, called Dexter transfer. Dexter transfer rate is given as [20]:

$$k_{Dexter} = \frac{2\pi}{\hbar} \Gamma^2 \int I_D(\lambda) \varepsilon_A(\lambda)\, d\lambda \tag{1.9}$$

where, Γ is the transition matrix element for charge exchange, which is expressed as:

$$\Gamma^2 = < \Phi_D(1)\Phi_A^*(2)| \frac{1}{4\pi\varepsilon_r\varepsilon_0 R} |\Phi_D^*(1)\Phi_A(2) >< \sigma_D(2)|\sigma_A(2) >< \sigma_D^*(1)|\sigma_A^*(1) > \tag{1.10}$$

Here, Φ is the spatial component of molecular ground state wavefunction, σ is the spin component of molecular ground state wavefunction (* denotes excited state). According to Equation (1.10), transition matrix element Γ becomes non-zero only if two molecular wavefunctions have overlap and ground state and excited state have the same spin multiplicity. This means that Dexter transfer allows triplet-triplet energy transfer between host and guest molecules, unlike FRET. Assuming hydrogenic initial and final states, Equation (1.10) can be approximated to $\Gamma^2 \propto exp(-\frac{2R}{L})$, where L is effective Bohr radius of molecules. Thus, Dexter transfer is only effective when two molecules are in proximity of 1 nm [21].

1.3.3. Color and efficiency of OLED

To represent color of specific photons, Commision Internationale de l'Éclairage (CIE) coordinate system is devised based on the spectral responsivity of ρ, γ, β cones in the retina [3]:

$$x = \int \Phi_P(\lambda)X(\lambda)d\lambda,\ y = \int \Phi_P(\lambda)Y(\lambda)d\lambda,\ z = \int \Phi_P(\lambda)Z(\lambda)d\lambda \quad (1.11)$$

$$\bar{x} = x / (x + y + z),\ \bar{y} = y / (x + y + z) \quad (1.12)$$

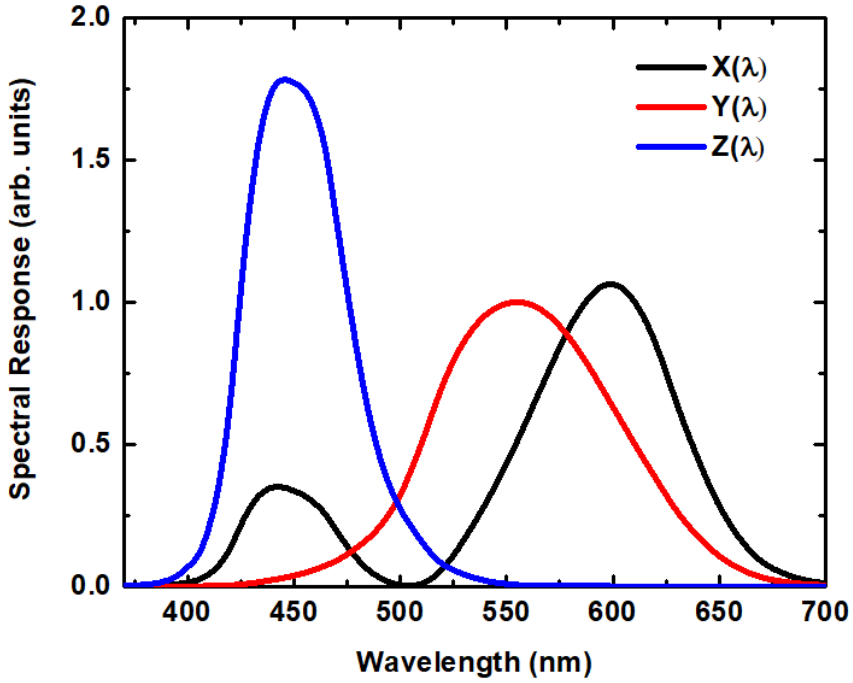

Figure 1.6. The standardized spectral response of the three color-sensitive photoreceptors cell.

where, Φ_p is photon flux from OLED emission, X(λ), Y(λ), Z(λ) are standardized response of the three color-sensitive photoreceptors in the human eye as shown in Figure 1.6. From the calculated $(\bar{x}, \bar{y})$ in Equation (1.12), the color of OLED is represented in CIE color space shown in Figure 1.7.

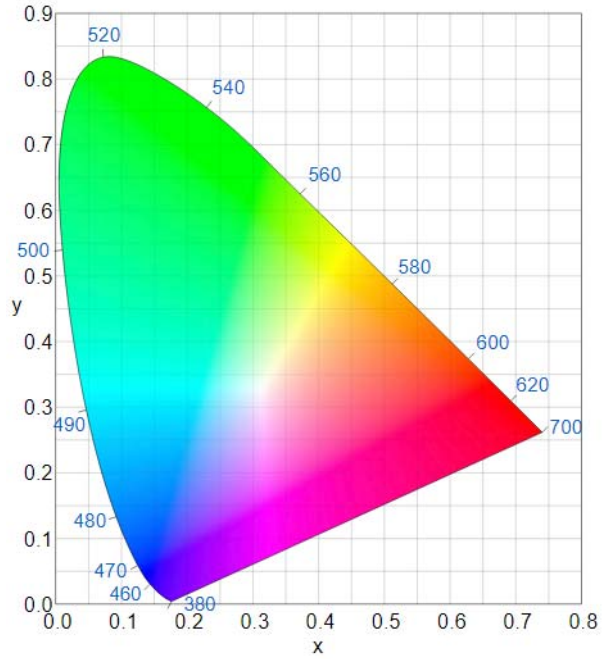

Figure 1.7. CIE color space (x, y) diagram. Color of mono-chromatic light is included in the curved boundary.

External quantum efficiency (EQE) is one of the most important figure of merits in OLED. It is defined as follows:

$$\begin{aligned} \mathrm{EQE} &= \frac{number\ of\ photons\ extracted}{number\ of\ electrons\ injected} \\ &= \frac{number\ of\ photons\ generated}{number\ of\ electrons\ injected} \times \frac{number\ of\ photons\ extracted}{number\ of\ photons\ generated} \\ &= \eta_C \eta_E \eta_{PLQY} \times \eta_{out} \end{aligned} \tag{1.13}$$

Here, η_C is the charge balance factor, η_E is the ratio of emissive excitons, η_{PL} is the photoluminescence efficiency, and η_{out} is the outcoupling efficiency. η_C represents confinement of electrons and holes within EML without any leakage to the adjacent layers. η_E is the ratio of radiative excitons in emissive molecules. As mentioned in 1.3.1, η_E of fluorescent OLED is 25 %,

while η_E of phosphorescent OLED utilizing triplets emitters is 100 %. η_{PL} is determined by the ratio of the radiative decay rate (k_r) to the total decay rate ($k_r + k_{nr}$) including non-radiative decays. Except η_{out}, first three terms are related to the photo-physical property of emissive molecules and the structure of OLED. Thus, multiplication of η_C, η_E, and η_{PLQY} is the internal quantum efficiency (IQE) of OLED. The outcoupling efficiency, η_{out}, is typically ~20 % since many of generated photons within EML are dissipated by substrate, waveguide, and surface plasmon modes [22, 23].

To define OLED efficiency in terms of a photometric unit, luminous efficiency function (P(λ)) for photopic response is introduced as shown in Figure 1.8. This indicates the averaged spectral sensitivity of photoreceptor cells in human eyes.

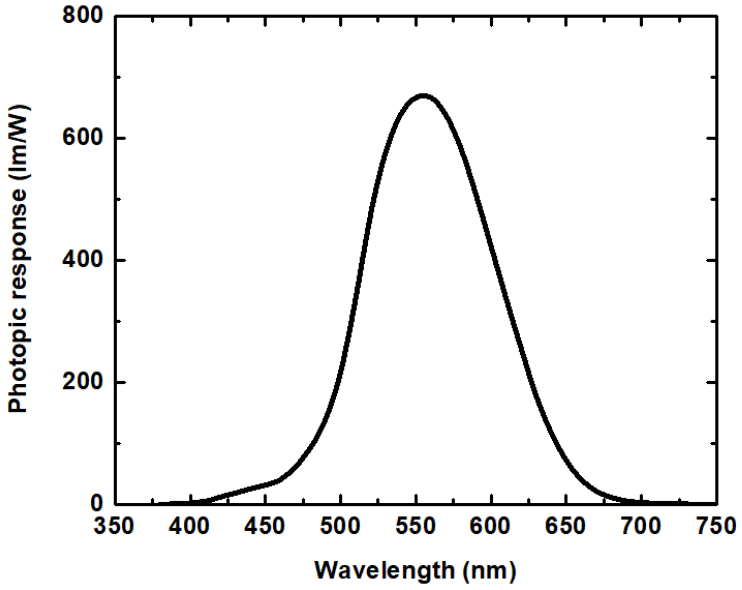

Figure 1.8. Photopic response curve.

Normalized luminous responsivity (Φ_L) of human eyes to photon flux (Φ_p) is defined as:

$$\Phi_L = \frac{\int \Phi_P P(\lambda) d\lambda}{\int \Phi_P d\lambda} \tag{1.14}$$

The luminous flux (L, in lumen), is a photometric unit equivalent to radiant power (Watt), defined as:

$$\mathrm{L} = \Phi_L \frac{hc}{\lambda} \times (EQE) \times \frac{I}{q} \tag{1.15}$$

Where, h is Planck's constant, c is the speed of light, I is current, q is the elementary charge. The power efficiency of OLED is calculated by dividing the luminous flux with the electrical power.

$$\eta_p = L/(V \times I) = \Phi_L \times EQE \times \frac{1}{V} \times \frac{hc}{q\lambda}$$

1.4. References

[1] M. Pope and C. E. Swenberg, *Electronic processes in organic crystals and polymers*. Oxford University Press on Demand, 1999.

[2] D. Ma and Y. Chen, *Organic Semiconductor Heterojunctions and Its Application in Organic Light-Emitting Diodes*. Springer, 2017.

[3] A. Köhler and H. Bässler, *Electronic processes in organic semiconductors: An introduction*. John Wiley & Sons, 2015.

[4] C. Kittel, *Introduction to solid state physics*. Wiley, 2005.

[5] C. W. Tang, "Two-layer organic photovoltaic cell," *Appl. Phys. Lett.*, vol. 48, no. 2, pp. 183–185, 1986.

[6] X. Che, X. Xiao, J. D. Zimmerman, D. Fan, and S. R. Forrest, "High-Efficiency, Vacuum-Deposited, Small-Molecule Organic Tandem and Triple-Junction Photovoltaic Cells," *Adv. Energy Mater.*, Aug. 2014.

[7] S. Zhang, L. Ye, and J. Hou, "Breaking the 10% Efficiency Barrier in Organic Photovoltaics: Morphology and Device Optimization of Well-Known PBDTTT Polymers," *Adv. Energy Mater.*, vol. 6, no. 11, pp. 1–20, 2016.

[8] P. Peumans, A. Yakimov, and S. R. Forrest, "Small molecular weight organic thin-film photodetectors and solar cells," *J. Appl. Phys.*, vol. 93, no. 7, p. 3693, 2003.

[9] S. R. Forrest, "The Limits to Organic Photovoltaic Cell Efficiency," *MRS Bull.*, vol. 30, no. 1, pp. 28–32, 2005.

[10] N. C. Giebink, G. P. Wiederrecht, M. R. Wasielewski, and S. R. Forrest, "Ideal diode equation for organic heterojunctions. I. Derivation and application," *Phys. Rev. B*, vol. 82, no. 15, p. 155305, Oct. 2010.

[11] C. W. Tang and S. A. Vanslyke, "Organic electroluminescent diodes Organic electroluminescent diodes," *Appl. Phys. Lett.*, vol. 51, no. 913, pp. 10–13, 1987.

[12] M. A. Baldo, S. Lamansky, P. E. Burrows, M. E. Thompson, and S. R. Forrest, "Very high-efficiency green organic light-emitting devices based on electrophosphorescence," *Appl. Phys. Lett.*, vol. 75, no. 1, pp. 4–6, 1999.

[13] M. A. Baldo, M. E. Thompson, and S. R. Forrest, "High-efficiency fluorescent organic light-emitting devices using a phosphorescent sensitizer," *Nature*, vol. 403, no. 6771, pp. 750–753, 2000.

[14] N. C. Giebink *et al.*, "Intrinsic luminance loss in phosphorescent small-molecule organic light emitting devices due to bimolecular annihilation reactions," *J. Appl. Phys.*, vol. 103, no. 4, p. 44509, 2008.

[15] Y. Zhang, J. Lee, and S. R. Forrest, "Tenfold increase in the lifetime of blue phosphorescent organic light-emitting diodes," *Nat. Commun.*, vol. 5, pp. 1–7, 2014.

[16] J. Lee, C. Jeong, T. Batagoda, C. Coburn, M. E. Thompson, and S. R. Forrest, "Hot excited state management for long-lived blue phosphorescent organic light-emitting diodes," *Nat. Commun.*, vol. 8, no. May, pp. 1–9, 2017.

[17] C. Adachi, M. A. Baldo, M. E. Thompson, and S. R. Forrest, "Nearly 100% internal phosphorescence efficiency in an organic light emitting device," *J. Appl. Phys.*, vol. 90, no. 10, pp. 5048–5051, 2001.

[18] T. Főrster, "10th Spiers Memorial Lecture. Transfer mechanisms of electronic excitation," *Discuss. Faraday Soc.*, vol. 27, pp. 7–17, 1959.

[19] Y. Kawamura, J. Brooks, J. J. Brown, H. Sasabe, and C. Adachi, "Intermolecular interaction and a concentration-Quenching mechanism of phosphorescent Ir(III) complexes in a solid film," *Phys. Rev. Lett.*, vol. 96, no. 1, pp. 11–14, 2006.

[20] D. L. Dexter, "A theory of sensitized luminescence in solids," *J. Chem. Phys.*, vol. 21, no. 5, pp. 836–850, 1953.

[21] Y. Zhang and S. R. Forrest, "Triplet diffusion leads to triplet-triplet annihilation in organic phosphorescent emitters," *Chem. Phys. Lett.*, vol. 590, pp. 106–110, 2013.

[22] S. Nowy, J. Frischeisen, and W. Brütting, "Simulation based optimization of light-outcoupling in organic light-emitting diodes," vol. 7415, p. 74151C, 2009.

[23] W. Brütting, J. Frischeisen, T. D. Schmidt, B. J. Scholz, and C. Mayr, "Device efficiency of organic light-emitting diodes: Progress by improved light outcoupling," *Phys. Status Solidi Appl. Mater. Sci.*, vol. 210, no. 1, pp. 44–65, 2013.

Chapter 2

Method

This chapter provides background information about experimental methods and characterization techniques used in the following chapters. Theoretical description with experimental details are included.

2.1. Growth technique of organic materials

Various growth techniques are available to deposit organic thin-films. Most common ways to deposit organic-thin films are vacuum thermal evaporation, organic vapor phase deposition, and spin-casting. Vacuum thermal evaporation (VTE) and organic vapor phase deposition will be explained in detail since the difference between the two growth techniques is a main topic in Chapters 3 - 5.

2.1.1. Vacuum thermal evaporation

Vacuum thermal evaporation is widely used in organic thin-film deposition due to its simple and intuitive operation. Organic materials are loaded in a molybdenum or tungsten baffled boat. A resistive heater heats up the baffled boat to evaporate organic materials. Evaporated molecules are ballistically transported from the boat to a substrate in a high vacuum environment ($\sim 10^{-7}$ torr). Quartz crystal microbalance is used to monitor the thickness of the deposited organic

thin-film based on the crystal's frequency change depending on the mass deposited on the crystal. Substrate rotation is usually required to achieve high uniformity (>90 %). The material utilization efficiency is typically low compared to organic vapor phase deposition even though it strongly depends on the geometry of the chamber (distance from the boat to the substrate, size of the chamber, etc.). For example, a VTE chamber in a laboratory-scale (~ 4 inch diameter substrate and 25 inches chamber height) has less than 5 % material utilization efficiency, whereas industrial VTE system with an in-line linear source has at least 50 % material utilization efficiency [1, 2].

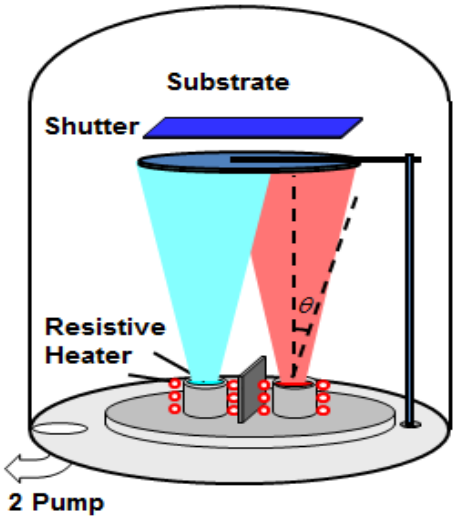

Figure 2.1. Schematic diagram of vacuum thermal evaporation.

2.1.2. Organic vapor phase deposition

Organic vapor phase deposition (OVPD) is the deposition technique using a carrier gas based on vapor phase epitaxy. Organic materials are loaded in a boat at one end, being transported towards a cooled substrate via the inert carrier gas. The pathway of the evaporated material follows the direction of the carrier gas flow. Thus, the chamber configuration of OVPD is not limited to

the facing-down configuration of VTE. It can be either horizontal or facing-up to ease manufacturing integration [3, 4]. The temperature of the OVPD chamber wall needs to be maintained at an elevated temperature to prevent any condensation of the evaporated organic vapor. Therefore, material utilization efficiency of OVPD is much higher than that of VTE where evaporated organics can be randomly adsorbed on the chamber wall [5]. Also, uniformity of OVPD is high (> 90%) even without rotation as far as the substrate temperature is uniformly maintained [6]. OVPD has various growth parameters such as chamber pressure, substrate temperature, carrier gas flow rate that VTE does not have. With these multiple growth parameters, OVPD can effectively control the morphology of organic thin films. The effects of the morphological change on the performance of OPV will be discussed throughout Chapters 3 - 5. A simplified diagram of an OVPD system is shown in Figure 2.2.

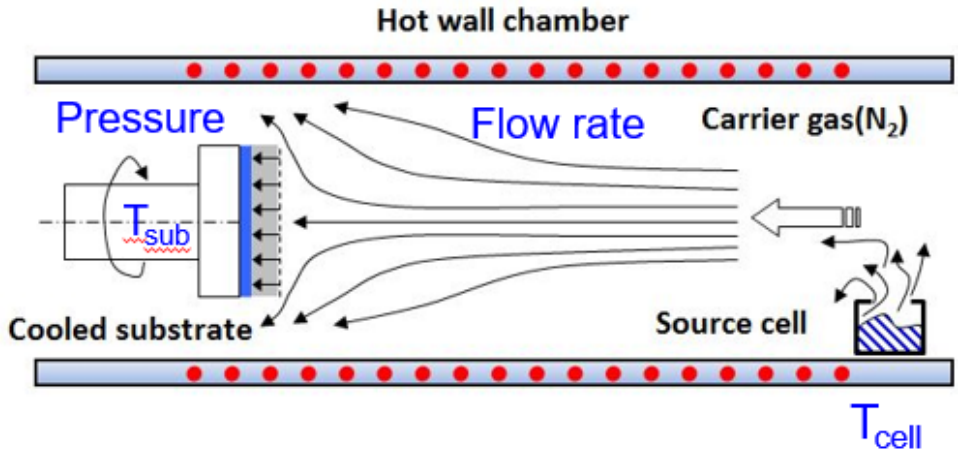

Figure 2.2. Schematic diagram of organic vapor phase deposition system. Growth parameters are indicated.

2.1.3. Spin-coating

Spin-coating is a simple way to deposit organic thin films. An organic solution is prepared by dissolving organic materials in organic solvents (1,2-Dichlorobenzene, Tetrahydrofuran,

Chloroform, etc.). A typical spin-coating process starts with dropping an organic solution on a substrate, rotating the substrate rapidly afterwards. Usually thin films of less than 300 nm thick are formed after the spin-coating since majority of solutions are removed during the rotation. The thickness of the thin-film is determined by the concentration of the solution, viscosity of the solution, and the spin speed. Spin-coating is the most effective method to deposit polymer materials because VTE and OVPD require a high processing temperature and will induce thermal decomposition of organic materials. However, the spin-coating is not suitable for an organic multi-layer structure because spin-coating of an additional layer can dissolve the preformed organic layers underneath. Depositing multi-layers through spin-coating is possible by using orthogonal solvents in each layer, however, it is practically impossible to find the collection of orthogonal solvents for every organic layer.

2.2. Thin-film characterization method

As the morphology of organic thin-film is critically important to the performance of organic optoelectronic devices, representative characterization techniques are summarized and explained in this subsection. Depending on the property of organic materials (crystallinity, domain size, chemical composition, etc.), a proper technique needs to be chosen to characterize the organic thin-film correctly.

2.2.1. Atomic force microscopy

Figure 2.3 shows the atomic force microscope (AFM), which maps the surface topology or surface composition with a resolution less than a nanometer by means of the force measurement

between its cantilever tip and the surface of a specimen. It records the change of a laser signal reflected from the probe tip attached to the cantilever.

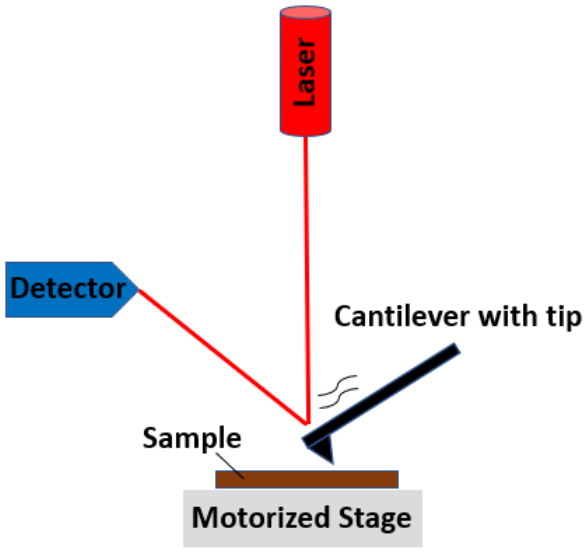

Figure 2.3. Schematic representation of atomic force microscope.

There are three measurement modes of AFM - contact mode, non-contact mode, and tapping mode. The contact mode has a fast scan speed, but usually induces a damage on a soft organic film surface. The non-contact mode is suitable on the surface of organic films. However, because of its

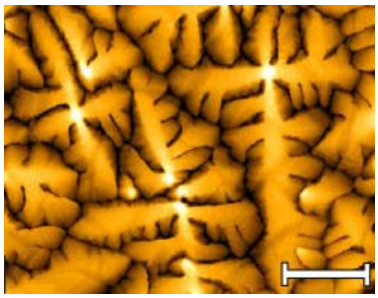

Figure 2.4. AFM image of 100 nm pentacene thin-film. Scale bar is 2 μm long.

slow scan speed and high sensitivity to environment, often the tapping mode is more preferred to the non-contact mode for organic thin films. From the image acquired, a surface roughness is typically represented as the root mean-square (RMS) value of the height variation. An AFM image of pentacene thin-films is shown in Figure 2.4. [6]

2.2.2. X-Ray diffraction

X-Ray diffraction (XRD) is a useful measurement technique to unravel structural information of materials. If a given specimen has a certain crystal structure, incident X-ray will be diffracted at an angle determined by Bragg's law of diffraction:

$$2d \sin\theta = n\lambda \tag{2.1}$$

where, d is the crystal plane spacing, θ is the incident angle of X-ray, n is an integer, and λ is the wavelength of the incident X-ray. After X-ray is generated by striking a target metal (typically Cu,

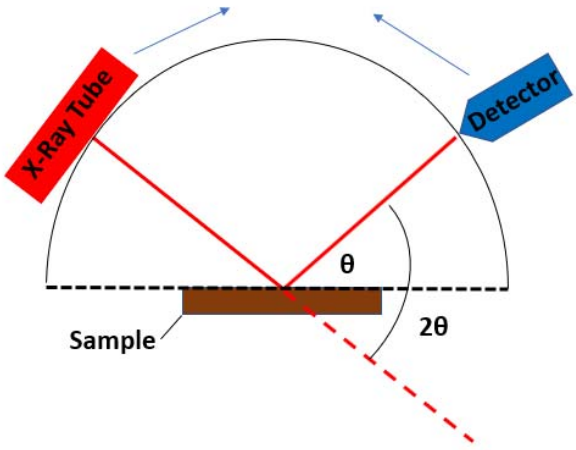

Figure 2.5. Schematic diagram of Bragg-Brentano (θ-2θ) configuration in XRD measurement.

Mo) with electron beams accelerated at a high voltage (10~100Kv), Bragg-Brentano (θ - 2θ) configuration is used to collect diffraction data of the specimen as shown in Figure 2.5. Once the peak positions are identified, a corresponding crystal plane spacing can be easily calculated with λ of X-ray and the measured θ. Furthermore, an approximate crystallite size can be calculated based on Scherrer's equation [7]:

$$B(2\theta) = \frac{0.93\times\lambda}{L\cos\theta} \tag{2.2}$$

where, B is an approximate crystallite size, L is the full width-half maximum (FWHM) value of the obtained peaks in the XRD measurement. Thus, the crystallite size gets smaller with large L. The application of Equation (2.1) and Equation (2.2) to analyze the structural parameters of the organic thin-film will be illustrated in Chapters 4 and 5.

2.2.3. Transmission electron microscopy

Transmission electron microscope (TEM) directs an electron beam to transmit through a specimen, creating images based on the interaction of electrons with the specimen. The intensity change after the electron beam passes the specimen creates image contrast in the fluorescent screen. Simplified TEM configuration is shown in Figure 2.6. TEM can also measure diffraction from electron beam using diffraction aperture in the microscope column. Since short de Brogile wavelength of electrons is extremely short (2.24 *pm* at 300 *keV*), the imaging resolution is less than few angstroms. Thus, TEM is a useful technique to investigate the morphology of organic thin-films down to nano-size. Examples of TEM images for organic materials are shown in Figure

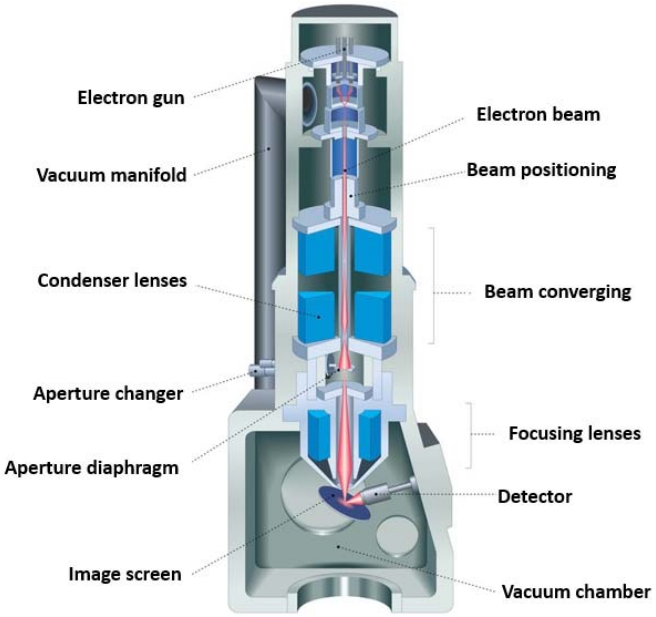

Figure 2.6. Schematic cross section of transmission electron microscope.

2.7 [8]. One practical challenge in TEM for organic thin-film characterization is the difficulty in sample preparation. To get a cross-section image of a thin-film, an ion-beam milling process is used to cut specimen and attach the section to a TEM grid. A sophisticated sample-cut is required because organics easily get damaged from the high ion-beam intensity. Detailed description of sample preparation for TEM is elsewhere [9, 10]. An alternative transfer method of organic thin-films to a TEM grid is introduced. First, dip a Si/MoO_3 substrate having a deposited organic thin-film into DI water. The thin-film is delaminated from the substrate since MoO_3 is water-soluble. The film transfer to a TEM grid is completed by dredging the thin-film floating on the water surface. An electron diffraction image shown in Chapter 3 was obtained by this transfer method.

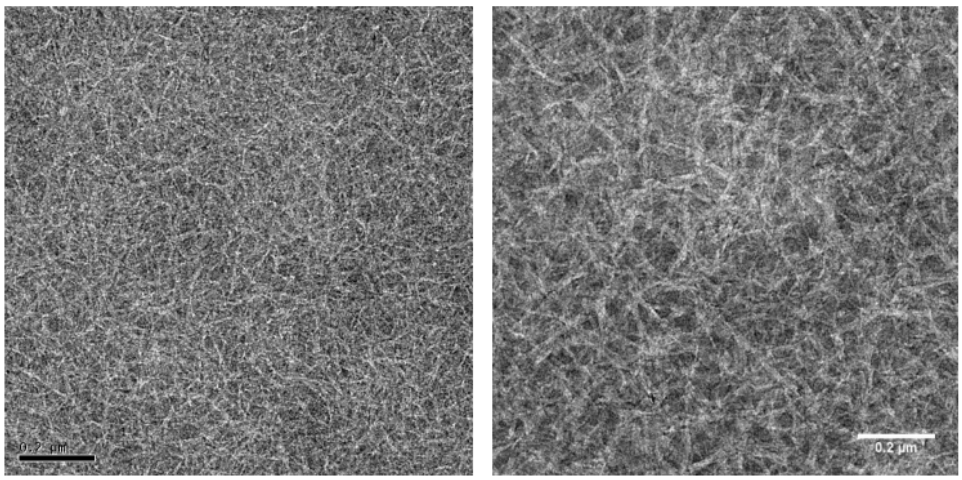

Figure 2.7. TEM images of photoactive layers of new (left) and old (right) batches of PDPPTPT polymer with PCBM [8].

2.3. References

[1] S. Van Slyke *et al.*, "Linear Source Deposition of Organic Layers for Full-Color OLED," *SID Symp. Dig. Tech. Pap.*, pp. 886–889, 2002.

[2] U. Hoffmann, H. Landgraf, M. Campo, J. Bruch, S. Keller, and M. Koenig, "46 . 1 : New Concept for Large Area White OLED Production for Lighting," *Camera*, pp. 688–691, 2010.

[3] F. Yang, K. Sun, and S. R. Forrest, "Efficient Solar Cells Using All-Organic Nanocrystalline Networks," *Adv. Mater.*, vol. 19, no. 23, pp. 4166–4171, Dec. 2007.

[4] C. Rolin, G. Vartanian, and S. R. Forrest, "Laser induced fluorescence monitoring of the transport of small organic molecules in an organic vapor phase deposition system," *J. Appl. Phys.*, vol. 112, no. 11, p. 113502, 2012.

[5] C. Rolin, B. Song, and S. R. Forrest, "Mass Transport through the Carrier Gas Boundary Layer in Organic Vapor Phase Deposition," *Phys. Rev. Appl.*, vol. 1, no. 3, p. 34002, Apr. 2014.

[6] C. Rolin, K. Vasseur, J. Genoe, and P. Heremans, "Growth of pentacene thin films by in-line organic vapor phase deposition," *Org. Electron.*, vol. 11, no. 1, pp. 100–108, Jan. 2010.

[7] A. L. Patterson, "The Scherrer formula for X-ray particle size determination," *Phys. Rev.*, vol. 56, no. 10, p. 978, 1939.

[8] K. H. Hendriks, G. H. L. Heintges, V. S. Gevaerts, M. M. Wienk, and R. a J. Janssen, "High-molecular-weight regular alternating diketopyrrolopyrrole-based terpolymers for efficient organic solar cells," *Angew. Chemie - Int. Ed.*, vol. 52, no. 32, pp. 8341–8344, 2013.

[9] J. Mayer, L. a Giannuzzi, T. Kamino, and J. Michael, "TEM Sample Preparation and Damage," *MRS Bull.*, vol. 32, no. 5, pp. 400–407, 2007.

[10] R. M. Langford and A. K. Petford-Long, "Preparation of transmission electron microscopy cross-section specimens using focused ion beam milling," *J. Vac. Sci. Technol. A Vacuum, Surfaces, Film.*, vol. 19, no. 5, pp. 2186–2193, 2001.

Chapter 3

Effect of mixed layer crystallinity on the performance of organic photovoltaics

This chapter is adapted from the peer-reviewed publication: *Adv. Mater.*, 26, 2914-2918 (2014)

3.1. Introduction

State-of-the-art solar cells based on small molecular weight organic molecules rely on multilayer structures whose morphology must be engineered at the nanoscale [1–5]. It follows, therefore, that growth methods enabling control over film morphology and layering schemes are required to achieve this objective. One such method is organic vapor phase deposition (OVPD), where organic molecules are transported by a hot inert carrier gas from the source to a cooled substrate where they condense to form a thin film [6, 7]. Compared to conventional vacuum thermal evaporation (VTE), the use of a carrier gas in OVPD dramatically changes many aspects of the film deposition kinetics. For example, the presence of carrier gas molecules in the vicinity of the substrate leads to a reduced molecular mean free path [8–10]. Furthermore, the formation of complex multilayers and mixed or doped layers are enabled by the precise control over gas flow rates, source temperatures, background pressure, and substrate temperature [11]. And finally, OVPD is capable of high speed film growth with efficient material utilization and thickness uniformity over large substrate areas [12, 13]. Indeed, OVPD is particularly useful in the growth

of complex morphologies such as those inherent in mixed donor/acceptor heterojunctions. These structures have been shown to maximize the efficiency of exciton dissociation by distributing the donor-acceptor interface throughout the photoactive OPV layers [14-16]. The morphology control afforded by OVPD can be engineered to minimize photo-generated charge recombination often incurred in the mixed region [8,17,18].

3.2. Results & Discussion

We demonstrate organic photovoltaic (OPV) cells based on a nanocrystalline mixed tetraphenyldibenzoperiflanthen (DBP): C_{70} heterojunction grown by OVPD with a power conversion efficiency, *PCE* = 6.7±0.2%, compared to 6.2±0.2% for analogous, optimized devices grown by VTE. Due to the lower electrical resistance of the nanocrystalline layers formed via OVPD, the active region thickness can be almost double those grown by VTE. The increased cell thickness has the potential to ease manufacturing tolerances by reducing the occurrence of shorts due to pinholes often encountered in thinner cells [19–21]. In addition, the material utilization efficiency of OVPD is generally significantly higher than VTE [22,23], thereby the increased thickness of the organic layer should not negatively impact the total cost of device fabrication.

3.2.1. Performance of mixed heterojunction OPVs

Mixed heterojunction OPVs were fabricated with the following structure: Glass/indium tin oxide (ITO) anode/MoO_3 (10 nm)/DBP:C_{70} (*x* nm, 1:10 ratio by volume)/bathophenanthroline (BPhen) (8 nm)/Ag cathode (100 nm). The 1:10 DBP:C_{70} films were grown by VTE (base pressure ~2×10^{-7} torr) at deposition rates of 0.2 Å/s and 2.0 Å/s, and by OVPD using source temperatures of 375±2 °C and 540±1 °C for DBP and C_{70}, respectively. For OVPD, a N_2 carrier at a mass flow

rate of 50 standard cubic centimeters per minute (sccm) was simultaneously injected into both source cells using the system configuration described previously [8, 17, 18]. Device performance as a function of mixed active layer thickness, x, in Figure 3.1, indicates that for $x > 60$ nm, the *FF* of VTE-grown devices dramatically decreases. Consequently, at $x = 60$ nm the VTE-grown device has a maximum *PCE* = 6.2±0.2% (at 1 sun, AM1.5G illumination, spectrally corrected) and *FF* = 0.58±0.01. On the other hand, OVPD-grown devices have *FF* = 0.61±0.01 up to $x = 100$ nm, and the short-circuit current density, J_{sc}, peaks at $x = 100$ nm, leading to *PCE* = 6.7±0.2% and *FF*=0.61±0.01. These trends are also apparent in the *J-V* characteristics under similar illumination conditions shown in Figure 3.2 (left), where devices grown by VTE and OVPD are compared at the optimum thicknesses of $x = 60$ nm and 100 nm, respectively. Figure 3.2 (right) shows the

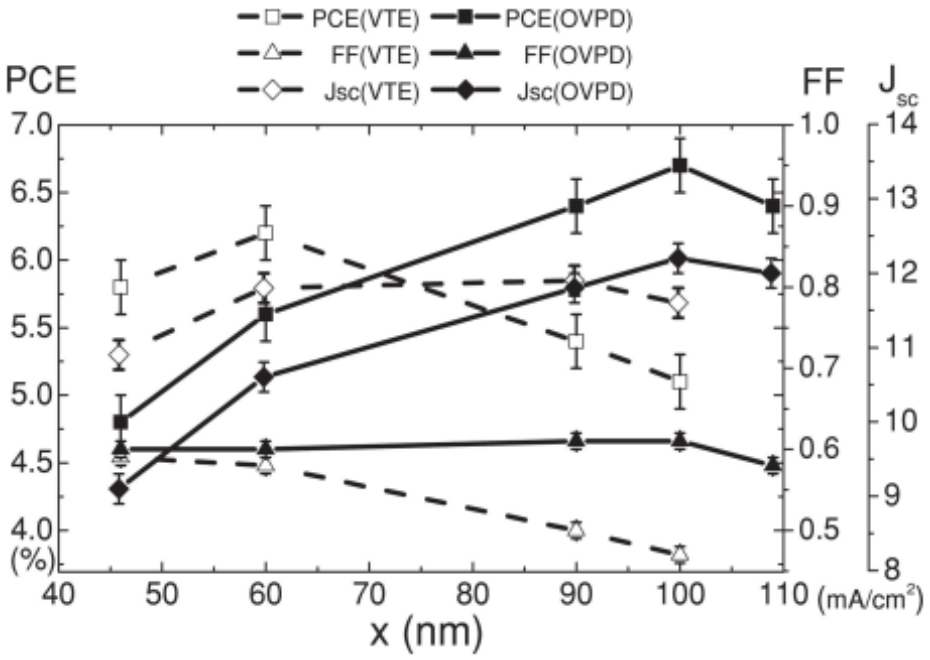

Figure 3.1. Power conversion efficiency (*PCE*), fill factor (*FF*), and short-circuit current density (J_{sc}) of DBP:C_{70} mixed heterojunction devices grown by VTE and OVPD as functions of mixed layer thickness. Open circuit-voltages for all devices are 0.90±0.01 V. Standard deviations of device parameters (J_{sc}, *FF*, *PCE*) are ±0.2 mA/cm^2, ±0.01, ±0.2%, respectively.

external and internal quantum efficiency (*EQE, IQE*, respectively) spectra of these devices. Here, *IQE* is obtained from the *EQE* and the absorption spectra [24, 25]. The x = 100 nm OVPD-grown device has a ~7% higher *IQE* than the x = 60 nm device grown by VTE. Since *IQE* is the ratio of charge at the contacts to the number of photons absorbed within the active layer [25], OVPD-grown OPVs exhibit higher efficiency charge transfer than analogous VTE-grown devices.

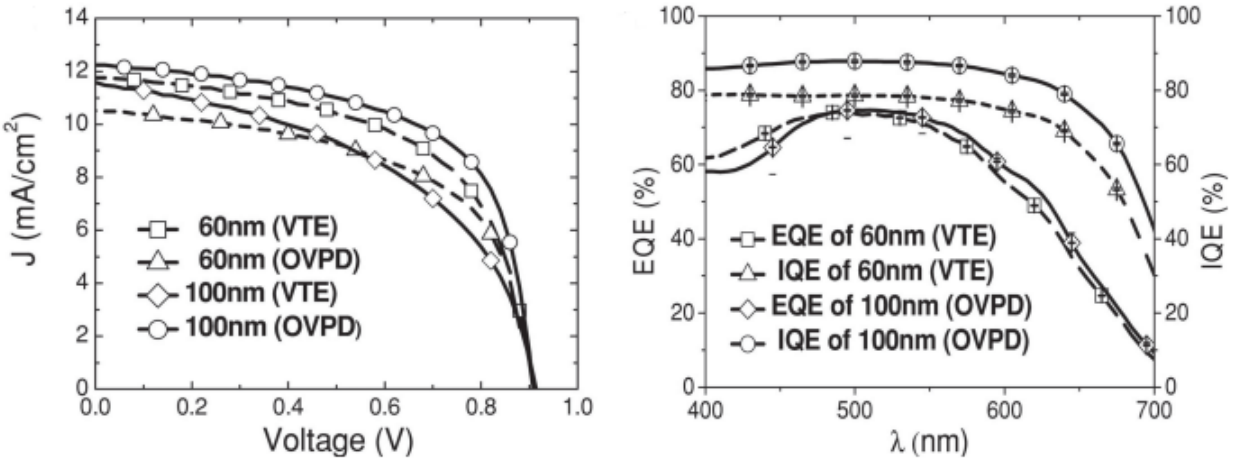

Figure 3.2. (left) Current density (J) versus voltage (V) characteristics under 1 sun illumination for 60 nm or 100 nm active layer thicknesses grown by VTE and OVPD, respectively. (right) External and internal quantum efficiencies as a function of wavelength (λ) of the devices.

3.2.2. Morphology of DBP:C_{70} mixed layer

The DBP:C_{70} mixed layers were examined using atomic force microscopy (AFM) and transmission electron microscopy (TEM) to determine the morphologies achieved by the two growth techniques. Figure 3.3 (top-left), shows an AFM image of a VTE-grown film on a Si substrate. The surface is featureless with a root-mean-square roughness of *rms* = 0.4±0.1 nm, showing no indication of a crystalline nanostructure. In contrast, the OVPD-grown film (Figure 3.3 top-right) exhibits ~ 40 nm diameter features suggestive of nanocrystallites, with *rms* = 1.5±0.2

nm. The structures were also investigated by selected area electron diffraction (SAED), as shown in Figure 3.3 (bottom). It has been reported that both hexagonal close packed (hcp) and face-centered cubic (fcc) polymorphs of C_{70} can co-exist, with their ratio dependent on the growth temperature and pressure [26–28]. The fcc polymorph of C_{70} has a unit cell dimension of a = 14.89Å [29]. The SAED pattern of the VTE-grown film (Figure 3.3 bottom-left) indicates a completely amorphous layer, which is in striking contrast to the OVPD-grown film in Figure 3.3 (bottom-right), where four concentric rings corresponding to diffraction peaks [29, 30] suggestive of fcc C_{70}. Identification of the peaks in the figure and their interplanar spacings are summarized

Table 3.1 Interplanar d-spacings of OVPD grown DBP:C_{70} films

(hkl) index	$d=a/\sqrt{h^2+k^2+l^2}$ [a]	d_1/d [b] (XRD)	d_1/d (SAED)
(111)	8.59 Å	1.00	1.00
(220)	5.26 Å	1.63	1.62
(311)	4.49 Å	1.91	1.93
(420)	3.39 Å	2.53	2.60

[a] a = 14.89Å is the lattice constant of the C_{70} fcc structure in. d_1 corresponds to the (111) plane. The errors in d_1/d from SAED ~ 3% arise from inaccuracies in extracting diameters of concentric rings in Figure 3.3.
[b] C_{70} data from Ref. 30.

in Table 3.1. We attribute the crystallinity of C_{70} observed in OVPD-grown films to the presence of N_2 molecules that impart energy during growth. The carrier gas enhances surface diffusion of the incident organic molecules that promotes nucleation, desorption, crystallite ripening, etc., resulting in a morphology that approaches that of the equilibrium crystal structure [10, 18].

While SAED does not provide information on the arrangement of the DBP molecules in such dilute mixtures as employed here, the differences in nanostructure result in changes in spectral properties from which the structure may be indirectly inferred. As shown in Figure 3.4, the OVPD-grown

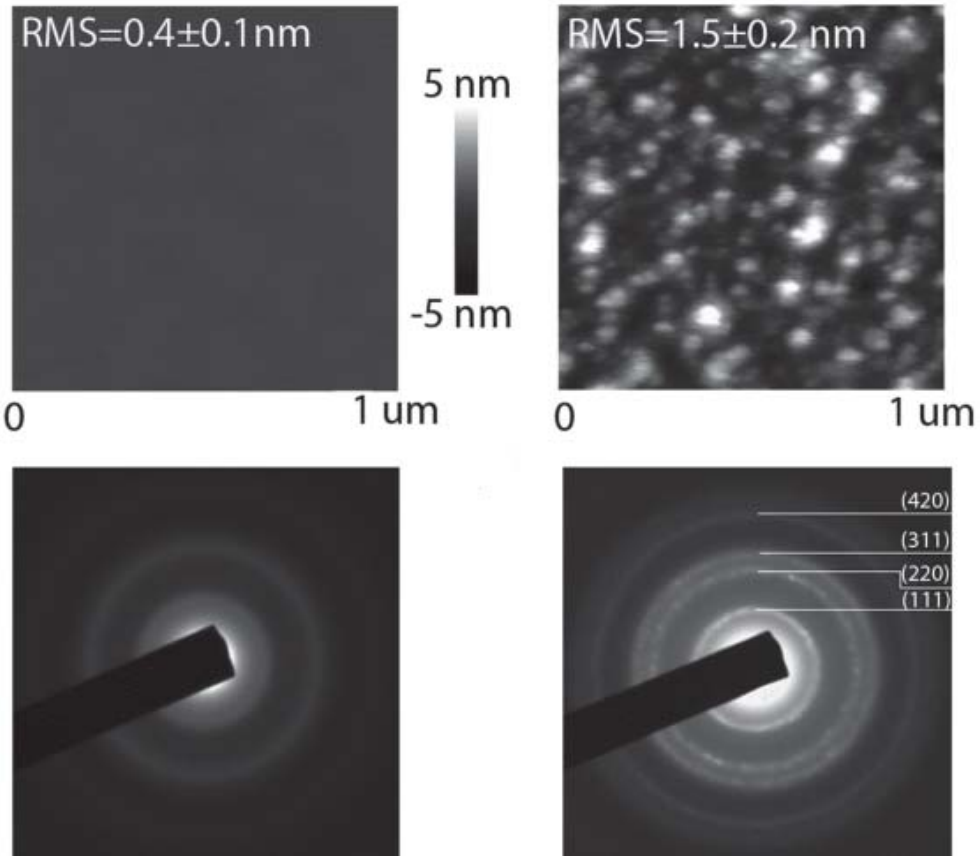

Figure 3.3. Atomic force microscopy (AFM) images of 60 nm thick DBP:C_{70} (1:10 ratio) films grown by (top-left) VTE and (top-right) OVPD on a Si substrate. The root-mean-square (RMS) roughness of the films is shown. The errors are due to variation from area to area of the film. Selected area electron diffraction (SAED) patterns of DBP:C_{70} films grown by (bottom-left) VTE and (bottom-right) OVPD. Corresponding Miller indices of C_{70} face-centered cubic (fcc) structure are indicated for the OVPD-grown film.

DBP:C_{70} film has a lower extinction coefficient (k) in the DBP spectral range between wavelengths of λ = 500 nm and 625 nm [15, 31, 32], compared to that grown by VTE. Anisotropic materials typically have at least two different optical constants: Ordinary optical constants for p-polarized light and extraordinary optical constants for s-polarizations [33]. For planar DBP molecule, the ordinary extinction coefficient is larger than the extraordinary coefficient, and hence the absorption of DBP depends on its preferred orientation in the film [31], which in turn is strongly affected by the substrate and growth process [33, 34]. In our case, we attribute the decreased extinction

coefficient in OVPD-grown films to a preferred molecular orientation along the axis of lower k relative to the light that is incident normal to the substrate. As a result, OVPD-grown OPVs require a thicker mixed layer than an analogous VTE-grown layer to achieve a similar *EQE*, as shown in Figure 3.1. Hence, we conclude that the nanocrystalline morphology of C_{70} affects the orientation of the diluted DBP when grown by OVPD, whereas this preferred orientation is not observed in VTE growth.

3.2.3. Optical and Electrical properties of DBP:C_{70} mixed layer

Since the nanostructure of the organic film affects the allowed optical transitions near highest occupied molecular orbital (HOMO) – lowest unoccupied molecular orbital (LUMO) energy gap (i.e. near the long wavelength optical cutoff) [35, 36], we can analyze the spectral properties of the films in this region to gain further information about their morphologies. That is,

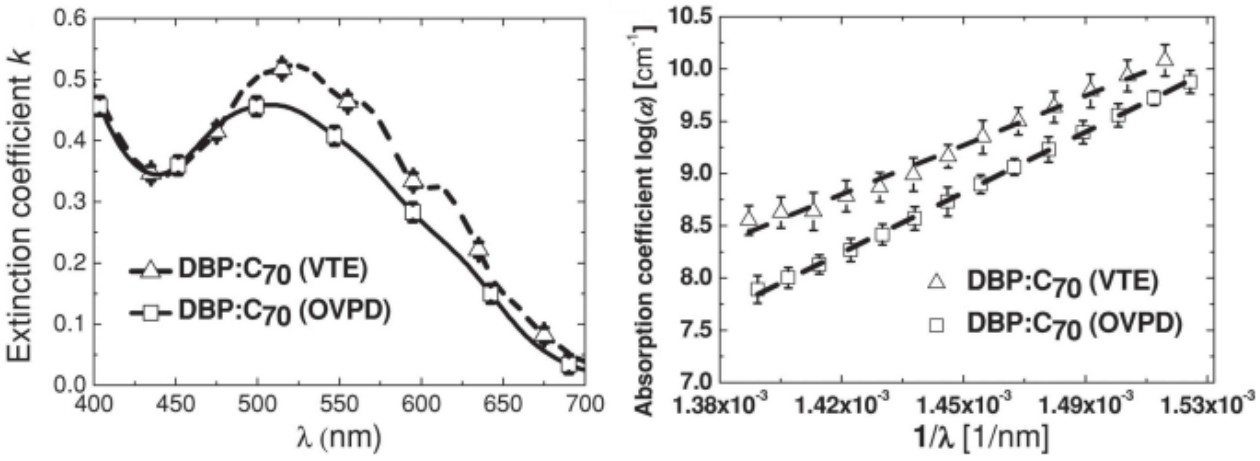

Figure 3.4. (left) Extinction coefficient (k) of DBP:C_{70} grown by VTE and OVPD as a function of wavelength (λ). (right) Natural logarithm of the absorption coefficient, log(α), of DBP:C_{70} films grown by VTE and OVPD *vs.* $1/\lambda$ near the film long wavelength cutoff. Dashed lines are linear fits to the data. Their slopes yield the Urbach tail energies, $U = 101\pm4$ meV and 81 ± 2 meV for VTE and OVPD-grown mixtures, respectively.

structural disorder leads to a broadened density of states that results in an Urbach tail near the absorption cutoff [37–39] that follows: $\alpha = \alpha_0 \exp(hc/(\lambda U))$. Here, α_0 is a constant, h is Planck's constant, c is the speed of light, and U is Urbach tail energy (see Figure 3.4). From the slopes of the best fits to the data, we obtain U=81±2 meV and 101±4 meV for DBP:C_{70} films grown by OVPD and VTE, respectively, compared to the reported value of VTE-grown C_{70} of 55 meV [38]. Errors in U correspond to the standard deviation of four samples. The lower energy for OVPD indicates reduced disorder than for VTE-grown films. This also agrees with the observation that OVPD results in a C_{70} fcc structure (c.f. Figure 3.3).

Finally, the *J-V* characteristics of the OPVs can be understood in terms of the modified ideal-diode equation for organic heterojunctions [40, 41]:

$$J = J_{sD}\left[exp\left(\frac{q(V-JR_S)}{n_D k_b T}\right) - \chi\right] + J_{sA}\left[exp\left(\frac{q(V-JR_S)}{n_A k_b T}\right) - \chi\right] - q\eta_{PPd}J_X. \quad (3.1)$$

Here, J_{sD} *and* J_{sA} are the saturation current densities associated with trapped charge in the donor and acceptor layers, respectively, n_D and n_A are the corresponding ideality factors, J_X is the exciton current density, R_s is the series resistance, q is electron charge, T is the temperature, k_b is Boltzmann's constant, and η_{PPd} is the polaron pair dissociation efficiency. Also, χ is the ratio of the polaron pair dissociation rate at voltage, V, to its value at equilibrium. For simplicity, we assume $\chi \approx 1$ [41]. The fit to the forward characteristics of the devices in Figure 3.1 measured at their optimal thicknesses are shown in Figure 3.5 (left), from which we obtain R_s *vs.* x plotted in Figure 3.5 (right), along with the corresponding *FF*. While R_s for VTE -grown devices increases linearly from 0.5±0.1 at x = 45 nm to 2.5±0.2 Ω-cm^2 at x = 100 nm, its value for OVPD-grown devices is nearly thickness independent, with R_s < 0.5±0.1 Ω-cm^2 up to x = 110 nm. The decreased

series resistances is primarily due to the improved crystallinity of C_{70} (see Figure 3.3). Furthermore, directional grain structure of DBP molecules has previously been observed for substrates heated during growth [42]. Since OVPD employs a hot carrier gas, the temperature of growth surface can be higher than in VTE growth. Further, oriented films of DBP may be induced to the higher surface mobility of molecules, also enabled by the presence of the carrier gas. This directionality in film growth leads to an equilibrium nanocrystalline structure that increases charge mobility [43]. Both the improved crystallinity of C_{70} and preferential orientation of DBP explain that OVPD growth results in a morphology that leads to an improved charge extraction compared to the amorphous VTE-grown structures.

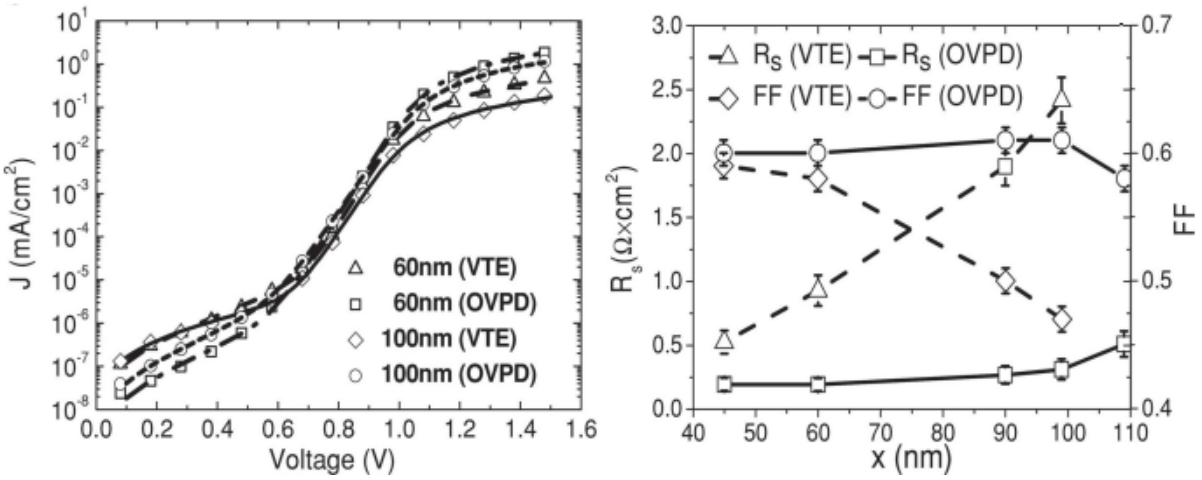

Figure 3.5. (left) Fits of the forward-biased *J-V* characteristics of the devices in Figure 3.1 using the ideal diode equation for 60 nm and 100 nm thick active layer OPVs grown by VTE and OVPD, respectively. (right) Series resistance (R_s) and fill factor (*FF*) of the devices. Error bars correspond to the standard deviation of 4 devices for each data point.

3.3. Conclusion

The growth of mixed DBP:C_{70} layers by OVPD leads to a nanocrystalline morphology that improves charge extraction and reduced charge recombination in mixed heterojunction organic photovoltaic cells relative to analogous cells grown by VTE. Since OVPD growth occurs near

thermodynamic equilibrium, mixed layers are nanocrystalline compared with the amorphous layers grown by the highly non-equilibrium process of VTE. A consequence of the enhanced crystallinity is a reduction of extinction coefficient of DBP. The enhanced crystallinity also results in a low series resistance R_s and hence, a high *FF* even for relatively thick mixed DBP:C_{70} films. The absorption loss in the nanocrystalline films is compensated by the use of thicker active layers without negatively impacting either R_s or *FF*. Optimal DBP:C_{70} layers grown by OVPD have a thickness of 100 nm, resulting in OPVs with a *PCE* = 6.7±0.2%. This compares to *PCE* = 6.2±0.2% obtained with optimized 60 nm-thick mixed layers grown by VTE. The significantly thicker nanocrystalline devices should ultimately result in higher device yields through the reduction in pin-holes and other shunt paths often observed in very thin VTE-grown OPVs.

3.4. Experimental details

Device fabrication: Glass substrates pre-coated with a 70 nm thick layer of indium tin oxide (ITO) having sheet resistance of 20 Ω/□ were cleaned with tergitol, deionized water, acetone, and isopropanol, followed by exposure to ultraviolet-ozone treatment for 10 min. The substrates were transferred into a vacuum thermal evaporation chamber to deposit MoO_3 at 1.0Å/s. The DBP:C_{70} mixed layers were grown on MoO_3 by either VTE or OVPD, transferring the samples into the respective growth chamber through an ultrahigh purity N_2-filled glove box. The remaining layers of BPhen and Ag were deposited by VTE, also following transfer from the OVPD reactor without air exposure. For VTE growth, two separate quartz crystal monitors tracked the deposition rates of DBP and C_{70}, at 0.2Å/s, 2.0Å/s (1:10 ratio), respectively at base pressure of ~10^{-7} torr. For OVPD, the three zones of the reactor were set a 570, 510, and 450˚C, respectively, creating a temperature gradient from the source to the substrate positions along the tube. The DBP and C_{70}

were co-evaporated by heating the source materials to 375±2˚C and, 540±1˚C respectively, at a source barrel flow rate of 50 sccm N_2. The gas solvent was further diluted by 20 sccm N_2 introduced directly into the main reactor tube. The pressure during growth was maintained at 0.61 torr. These conditions achieved the same deposition rate as in VTE.

Measurement of device characteristics: *J-V* characteristics were obtained in an ultrahigh purity N_2 gas environment using an Agilent 4156C semiconductor parameter analyzer. Simulated AM 1.5G illumination, 1 sun intensity (100mW/cm^2) was provided using a solar simulator, and calibrated using a standard Si reference cell traceable to National Renewable Energy Laboratory (NREL) standards. The *EQE* spectra were measured with Stanford SR830 DSP lock-in amplifier under 200 Hz-chopped monochromated Xe-lamp. A NIST-traceable Si detector was used as a reference.

Selective area electron diffraction (SAED) measurements: Organic layers were deposited onto MoO_3 (10 nm) pre-deposited on Si substrates cleaned with acetone and isopropanol. Organic layers were captured on a copper grid by dissolving MoO_3 in deionized water. The SAED patterns were recorded using a JEOL 3011 high resolution electron microscope at an accelerating voltage of 300kV with a 20 μm selective aperture diameter.

Measurement of optical constants: Variable angle spectroscopic ellipsometery was used to measure thickness and optical constants of thin film samples deposited on Si substrates. Spectroscopic data were recorded in the near infrared for thickness measurements, and in the ultraviolet-visible range for obtaining the optical constants, using a B-spline algorithm [44]. This procedure was repeated over samples having different thicknesses to reduce error.

3.5. References

[1] S. R. Forrest, "The path to ubiquitous and low-cost organic electronic appliances on plastic," *Nature*, vol. 428, no. 6986, p. 911, Apr. 2004.

[2] W. Zeng, K. S. Yong, Z. M. Kam, F. Zhu, and Y. Li, "Effect of blend layer morphology on performance of ZnPc:C60-based photovoltaic cells," *Appl. Phys. Lett.*, vol. 97, no. 13, p. 133304, Sep. 2010.

[3] G. D. Wei, S. Y. Wang, K. Sun, M. E. Thompson, and S. R. Forrest, "Solvent-Annealed Crystalline Squaraine: PC70BM (1:6) Solar Cells," *Adv. Energy Mater.*, vol. 1, no. 2, p. 184, Mar. 2011.

[4] O. P. Lee *et al.*, "Efficient Small Molecule Bulk Heterojunction Solar Cells with High Fill Factors via Pyrene-Directed Molecular Self-Assembly," *Adv. Mater.*, vol. 23, no. 45, p. 5359, Dec. 2011.

[5] J. D. Zimmerman *et al.*, "Independent Control of Bulk and Interfacial Morphologies of Small Molecular Weight Organic Heterojunction Solar Cells," *Nano Lett.*, vol. 12, no. 8, p. 4366, Aug. 2012.

[6] M. Baldo *et al.*, "Organic Vapor Phase Deposition," *Adv. Mater.*, vol. 10, no. 18, pp. 1505–1514, Dec. 1998.

[7] M. Shtein, P. Peumans, J. B. Benziger, and S. R. Forrest, "Micropatterning of small molecular weight organic semiconductor thin films using organic vapor phase deposition," *J. Appl. Phys.*, vol. 93, no. 7, p. 4005, Apr. 2003.

[8] F. Yang, K. Sun, and S. R. Forrest, "Efficient Solar Cells Using All-Organic Nanocrystalline Networks," *Adv. Mater.*, vol. 19, no. 23, pp. 4166–4171, Dec. 2007.

[9] A. Farahzadi *et al.*, "Stochastic analysis on temperature-dependent roughening of amorphous organic films," *EPL (Europhysics Lett.*, vol. 90, p. 10008, Apr. 2010.

[10] C. Rolin *et al.*, "Vapor Phase Growth of Functional Pentacene Films at Atmospheric Pressure," *Adv. Funct. Mater.*, vol. 22, no. 23, pp. 5050–5059, Jul. 2012.

[11] C. Rolin, G. Vartanian, and S. R. Forrest, "Laser induced fluorescence monitoring of the transport of small organic molecules in an organic vapor phase deposition system," *J. Appl. Phys.*, vol. 112, no. 11, p. 113502, 2012.

[12] R. R. Lunt, B. E. Lassiter, J. B. Benziger, and S. R. Forrest, "Organic vapor phase deposition for the growth of large area organic electronic devices," *Appl. Phys. Lett.*, vol. 95, no. 23,

p. 233305, 2009.

[13] C. Rolin, K. Vasseur, J. Genoe, and P. Heremans, “Growth of pentacene thin films by in-line organic vapor phase deposition,” *Org. Electron.*, vol. 11, no. 1, pp. 100–108, Jan. 2010.

[14] J. Xue, B. P. Rand, S. Uchida, and S. R. Forrest, “A hybrid planar-mixed molecular heterojunction photovoltaic cell,” *Adv. Mater.*, vol. 17, no. 1, p. 65, 2005.

[15] X. Xiao, J. D. Zimmerman, B. E. Lassiter, K. J. Bergemann, and S. R. Forrest, “A hybrid planar-mixed tetraphenyldibenzoperiflanthene/C70 photovoltaic cell,” *Appl. Phys. Lett.*, vol. 102, no. 7, p. 73302, 2013.

[16] J. Xue, B. P. Rand, S. Uchida, and S. R. Forrest, “Mixed donor-acceptor molecular heterojunctions for photovoltaic applications. II. Device performance,” *J. Appl. Phys.*, vol. 104, no. 12, p. 124903, Dec. 2005.

[17] F. Yang, M. Shtein, and S. R. Forrest, “Controlled growth of a molecular bulk heterojunction photovoltaic cell,” *Nat. Mater.*, vol. 4, no. 1, pp. 37–41, Dec. 2004.

[18] F. Yang, M. Shtein, and S. R. Forrest, “Morphology control and material mixing by high-temperature organic vapor-phase deposition and its application to thin-film solar cells,” *J. Appl. Phys.*, vol. 98, no. 1, p. 14906, 2005.

[19] C. H. Peters, I. T. Sachs-Quintana, J. P. Kastrop, S. Beaupre´, M. Leclerc, and M. D. Mcgehee, “High Efficiency Polymer Solar Cells with Long Operating Lifetimes,” *Adv. Energy Mater.*, vol. 1, no. 4, p. 491, Jul. 2011.

[20] F. C. Krebs, *Stability and Degradation of Organic and Polymer Solar Cells*, 1st ed. John Wiley & Sons, Ltd, 2012.

[21] K. Feron, T. J. Nagle, L. J. Rozanski, B. B. Gong, and C. J. Fell, “Spatially resolved photocurrent measurements of organic solar cells: Tracking water ingress at edges and pinholes,” *Sol. Energy Mater. Sol. Cells*, vol. 109, pp. 169–177, Feb. 2013.

[22] M. Schwambera *et al.*, “OLED Manufacturing by Organic Vapor Phase Deposition Review of the OVPD Technology Scaling of the OVPD technology,” *SID Symp. Dig. Tech. Pap.*, vol. 34, no. 1, pp. 1419–1421, 2003.

[23] B. Marheineke, “OVPD: OLED manufacturing coming of age,” *Proc. SPIE*, vol. 5961, no. 1, p. 596101, Jun. 2005.

[24] L. a. a. Pettersson, L. S. Roman, and O. Inganäs, “Modeling photocurrent action spectra of photovoltaic devices based on organic thin films,” *J. Appl. Phys.*, vol. 86, no. 1, p. 487,

1999.

[25] P. Peumans, A. Yakimov, and S. R. Forrest, “Small molecular weight organic thin-film photodetectors and solar cells,” *J. Appl. Phys.*, vol. 104, no. 7, p. 3693, Apr. 2003.

[26] G. B. Vaughan *et al.*, “Orientational disorder in solvent-free solid c70,” *Science*, vol. 254, no. 5036, pp. 1350–3, Nov. 1991.

[27] G. Vantendeloo, S. Amelinckx, S. Muto, M. Verheijen, P. Vanloosdrecht, and G. Meijer, “Structures and phase transitions in C60 and C70 fullerites,” *Ultramicroscopy*, vol. 51, no. 1–4, p. 168, Jun. 1993.

[28] V. D. Blank *et al.*, “Structure and properties of C60 and C70 phases produced under 15 GPa pressure and high temperature,” *Phys. B Condens. Matter*, vol. 339, no. 1, p. 39, 2003.

[29] M. Valsakumar *et al.*, “Crystal structure and disorder in solid C70,” *Phys. Rev. B. Condens. Matter*, vol. 48, no. 12, pp. 9080–9085, Sep. 1993.

[30] M. C. Valsakumar *et al.*, “Crystal structure of solid C70,” *Pramana-Journal Phys.*, vol. 40, no. 2, pp. L137–L144, Feb. 1993.

[31] D. Yokoyama, Z. Q. Wang, Y. Pu, K. Kobayashi, J. Kido, and Z. Hong, “High-efficiency simple planar heterojunction organic thin-film photovoltaics with horizontally oriented amorphous donors,” *Sol. Energy Mater. Sol. Cells*, vol. 98, p. 472, Mar. 2012.

[32] Z. Wang, D. Yokoyama, X. Wang, Z. Hong, Y. Yang, and J. Kido, “Highly efficient organic p-i-n photovoltaic cells based on tetraphenyldibenzoperiflanthene and fullerene C-70,” *Energy Environ. Sci.*, vol. 6, no. 1, p. 249, Jan. 2013.

[33] D. Yokoyama, “Molecular orientation in small-molecule organic light-emitting diodes,” *J. Mater. Chem.*, vol. 21, no. 48, p. 19187, 2011.

[34] S. R. Forrest, “Ultrathin Organic Films Grown by Organic Molecular Beam Deposition and Related Techniques,” *Chem. Rev.*, vol. 97, no. 6, pp. 1793–1896, Sep. 1997.

[35] M. S. Dresselhaus and G. Dresslhaus, “Fullerenes and Fullerene Derived Solids as Electronic Materials,” *Annu. Rev. Mater. Sci.*, vol. 25, no. 1, p. 487.

[36] H. Kataura, Y. Endo, K. Kikuchi, T. Hanyu, and S. Yamaguchi, “Dielectric constants of C60 and C70 thin films,” *J. Phys. Chem. Solids*, vol. 58, no. 11, p. 1913, Nov. 1997.

[37] T. Gotoh, S. Nonomura, S. Hirata, and S. Nitta, “Photothermal bending spectroscopy and photothermal deflection spectroscopy of C60 thin films,” *Appl. Surf. Sci.*, vol. 113/114, p. 278, Apr. 1997.

[38] W. Zhou *et al.*, "Optical absorption spectra of C70 thin films," *J. Appl. Phys.*, vol. 104, no. 1, p. 459, 1996.

[39] H. Habuchi, S. Nitta, D. X. Han, and S. Nonomura, "Localized electronic states related to O-2 intercalation and photoirradiation on C60 films and C70 films," *J. Appl. Phys.*, vol. 87, no. 12, p. 8580, Jun. 2000.

[40] B. P. Rand, D. P. Burk, and S. R. Forrest, "Offset energies at organic semiconductor heterojunctions and their influence on the open-circuit voltage of thin-film solar cells," *Phys. Rev. B*, vol. 75, no. 11, p. 115327, Mar. 2007.

[41] N. C. Giebink, G. P. Wiederrecht, M. R. Wasielewski, and S. R. Forrest, "Ideal diode equation for organic heterojunctions. I. Derivation and application," *Phys. Rev. B*, vol. 82, no. 15, p. 155305, Oct. 2010.

[42] Y. Zhou, T. Taima, Y. Shibata, T. Miyadera, T. Yamanari, and Y. Yoshida, "Controlled growth of dibenzotetraphenylperiflanthene thin films by varying substrate temperature for photovoltaic applications," *Sol. Energy Mater. Sol. Cells*, vol. 95, no. 10, pp. 2861–2866, Oct. 2011.

[43] D. Yokoyama, Y. Setoguchi, A. Sakaguchi, M. Suzuki, and C. Adachi, "Orientation Control of Linear-Shaped Molecules in Vacuum-Deposited Organic Amorphous Films and Its Effect on Carrier Mobilities," *Adv. Funct. Mater.*, vol. 20, no. 3, pp. 386–391, Feb. 2010.

[44] J. W. Webber, T. A. R. Hansen, van de Sanden, and R. Engeln, "B-spline parametrization of the dielectric function applied to spectroscopic ellipsometry on amorphous carbon," *J. Appl. Phys.*, vol. 106, no. 12, p. 123503, 2009.

Chapter 4

Reliability of organic photovoltaics grown via organic vapor phase deposition

This chapter is adapted from the peer-reviewed publication: *Adv. Energy Mater.*, 5, 1401952 (2015)

4.1. Introduction

Recent improvement in small molecular-weight organic photovoltaics (OPVs) based on small molecular-weight materials have been realized by controlling thin-film morphology down to the nanometer scale [1–4]. Morphology has been found to influence device efficiencies [5–7], operational lifetimes [8-10], and failure mechanisms [11, 12]. One method to effectively control the film morphology is via growth by organic vapor phase deposition (OVPD) [13–15], where deposition occurs in the presence of a hot, inert carrier gas that provides extra energy for organic molecules to find an equilibrium configuration as they adsorb onto the substrate. This is in contrast to conventional vacuum thermal evaporation (VTE), where molecules follow ballistic trajectories from the source to the substrate, affording them little opportunity to find a lowest energy site before being buried by subsequently arriving molecules [16]. Also, OVPD has the advantages of high material utilization efficiency [17, 18], scalability for uniform growth over large substrates [19, 20], and enhanced device lifetime [21].

4.2. Results & Discussion

We show that morphological changes over time in a bathophenanthroline (Bphen) cathode blocking layer used in fullerene-based OPVs strongly impact device reliability, and that these changes are significantly reduced when the underlying active region is grown by OVPD *vs*. VTE. The wide energy gap Bphen has often been used in organic light emitting diodes (OLEDs) [22, 23], and OPVs [24, 25] as an optical spacer and exciton blocking layer proximal to the cathode contact [26, 27]. However, devices containing Bphen suffer from morphological instabilities [28, 29] resulting from its low glass transition temperature of 62 ˚C [30]. When deposited onto a tetraphenyl-dibenzoperiflanthene (DBP):C_{70} mixed active region grown by VTE, the morphological transformation of Bphen is found to significantly reduce the open-circuit voltage (V_{OC}) from 0.91±0.01% to 0.52±0.01% after aging at 50±5 ˚C for 250 hr under simulated AM 1.5G solar illumination. The decrease in V_{OC} results in the reduction of the power conversion efficiency from *PCE* = 6.0±0.2% to 3.1±0.2%. In addition, the morphological degradation results in electrical shorts across the devices, greatly reducing device yield from 93% to 63% for VTE-optimized devices. In contrast, the rougher, nanocrystalline surfaces of the DBP:C_{70} active layers grown by OVPD effectively pin the overlying amorphous Bphen, thereby preventing morphological changes. Hence, OPVs grown by OVPD have the highest *PCE* = 6.7±0.2%, and experience little change in V_{OC}, *PCE* or device yield when similarly aged.

4.2.1. Morphological degradation of Bphen

Atomic force (AFM) and optical microscope images of an 8 nm thick Bphen layer on a 1:10 (by vol.) DBP:C_{70} active layer (60 nm thick for VTE-grown, or 200 nm thick for OVPD-grown devices) are shown in Figure 4.1. Active layer thicknesses were individually optimized for

each growth technique, with the nanocrystalline OVPD active layer grown thicker due to its higher conductivity than the amorphous layers grown by VTE [31]. Figures 4.1a-d show images of a Bphen cap on a VTE-grown active layer after 0, 12 , 25, and 75 hr aging, respectively, under simulated 1 sun intensity. The initial Bphen surface has a root-mean-square (RMS) roughness of 0.4±0.1 nm, followed by spherulite growth appearing within 25 hr (Figure 4.1c, 4.1d). In contrast, the Bphen on the relatively rough nanocrystalline OVPD-grown active layer (RMS = 1.2±0.2 nm, Figure 4.1e) becomes only marginally rougher, to RMS = 2.2±0.4 nm, over this same period (Figure 4.1f, 4.1g). There are only a very few regions of local crystallization after 75 hr (Figure 4.1h). The active layer surface itself has an RMS roughness of 0.8±0.2 nm for VTE, and 4.1±0.2 nm for OVPD, neither of which changed after 75 hr. Hence, we conclude that all morphological

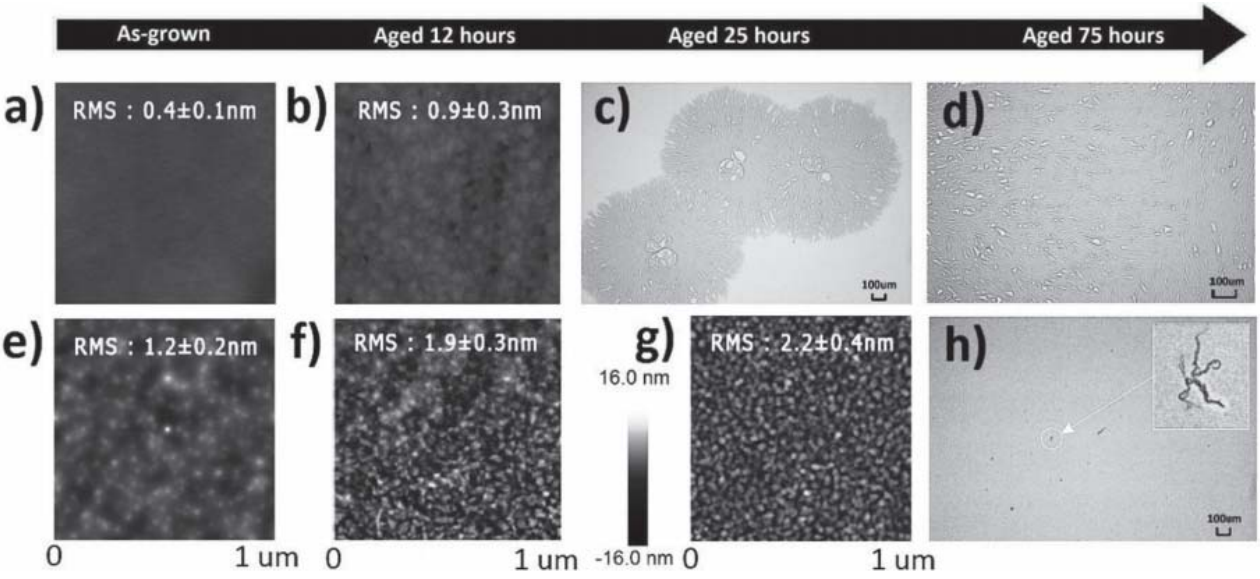

Figure 4.1. (a) Atomic force (AFM) and optical microscope images of an 8 nm thick Bphen film grown by vacuum thermal evaporation (VTE) on ITO/MoO_3 (10 nm)/1:10 (by vol.) DBP:C_{70} (60 nm grown by VTE) and after aging for (b) 12 hr, (c) 25 hr, and (d) 75 hr. (e) Similar images of an 8 nm thick Bphen film grown by VTE on an analogous structure but with the DBP:C_{70} grown to 200 nm thickness by organic vapor phase deposition (OVPD) and (f)-(h) after aging for the same durations. The root-mean-square (RMS) surface roughness of each image is indicated.

changes occur only in the Bphen overlayer. This suggests that the initially rough OVPD-grown surface pins the morphology of Bphen, whereas the smooth VTE-grown active layer does not.

X-ray diffraction (XRD) measurements of a 100 nm thick VTE- and OVPD-grown DBP:C_{70} layers on sapphire are shown in Figure 4.2a. The peak at 10.26±0.03º corresponds to diffraction from the (111) plane of the face-centered-cubic (fcc) crystal structure of C_{70} [32], which is only apparent for the OVPD-grown layer (curve II, Figure 4.2a), indicative of its nanocrystalline morphology. In contrast, the diffraction pattern of the VTE-grown active layer is featureless due to its amorphous structure (curve I, Figure 4.2a) [31]. Following aging for 75 hr, the XRD measurements of a 50 nm thick Bphen on a 100 nm thick DBP:C_{70} layer grown by VTE show the emergence of a narrow, strong reflection at 8.37±0.03º corresponding to a crystal plane spacing of d_{002} = 10.55±0.04 Å of the orthorhombic Bphen lattice (curve I, Figure 4.2b) [33], whereas the Bphen peak on the OVPD-grown layer is broad and weak (curve II, Figure 4.2b).

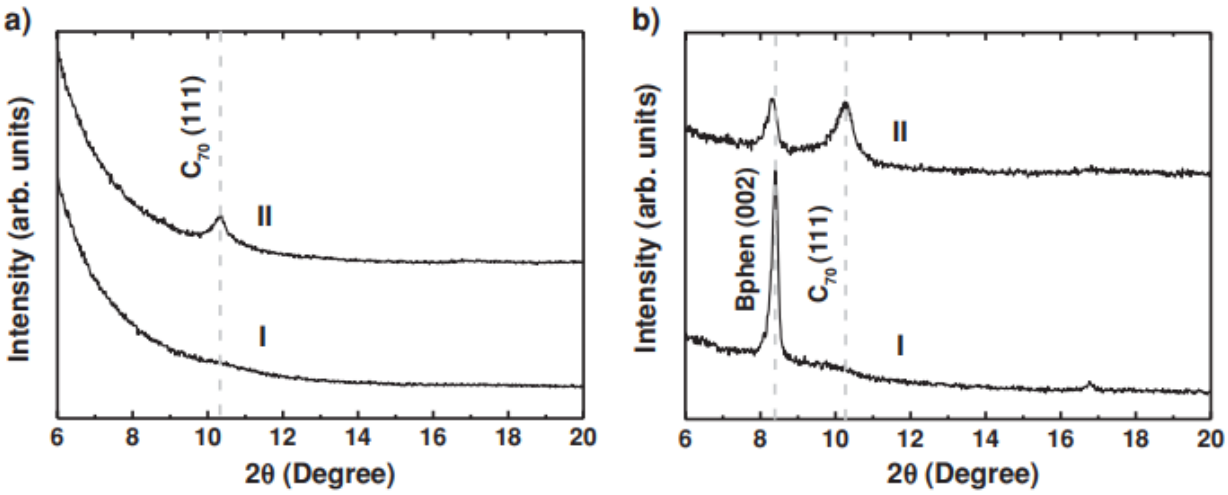

Figure 4.2. (a) Bragg-Brentano Cu-Kα X-ray diffraction (XRD) measurement of 1:10 (by vol.) DBP:C_{70} (100 nm thick) film grown by (I) VTE and (II) OVPD on sapphire substrates. (b) XRD data of the 50 nm thick Bphen on the same structure after aging for 75 hr. Peak positions and crystal indices are shown.

From the full width at half maxima of each peak (Table 4.1), we estimate that the aged Bphen crystallite size is at least 35% smaller when deposited on an OVPD-grown active layer than on one grown by VTE. Since the 50 nm thick Bphen layer used for XRD analysis is much greater than that used as a cathode blocker in an OPV (typically ~8 nm), the actual differences of Bphen crystallite size might be larger in devices themselves because the reduced thickness enhances pinning by the underlying rough surface.

Table 4.1 Crystallographic data for Bphen/DBP:C_{70}

Organic layer	Peak position [º]	FWHM [º]	d-spacing [Å]	Crystallite size[a)] [nm]
Bphen (OVPD)	8.34±0.03	0.28±0.02	10.59±0.04 /10.57[b)]	28±3
C_{70} (OVPD)	10.26±0.03	0.48±0.02	8.61±0.03 / 8.60[c)]	16±2
Bphen (VTE)	8.37±0.03	0.19±0.02	10.55±0.04 / 10.57[b)]	42±4

[a)] Calculated using the Scherrer equation, $t = \frac{K\lambda}{B\cos\theta}$ where K is a constant dependent on crystallite shape (0.9), λ is the wavelength of Cu-kα X-ray line, B is the full width at half maximum of the peak, and θ is the Bragg angle.
[b)] Calculated based on the (002) plane in orthorhombic Bphen crystal structure [33].
[c)] Calculated based on the (111) plane in face-centered-cubic (fcc) C_{70} crystal structure [32].

4.2.2. Performance change of mixed heterojunction OPVs with Bphen buffer

To understand the relationship between OPV performance and the morphological changes in Bphen, we fabricated three devices with the following structures: Glass/ITO/1:10 (by vol.) DBP:C_{70}(60 nm, 200 nm thick grown by VTE and 200nm thick grown by OVPD)/Bphen(8 nm thick grown by VTE)/Ag(100 nm). In fully VTE-grown devices, 60 and 200 nm were chosen for the active layer thicknesses – the thinner layer is optimized for VTE-grown devices, whereas the

thicker layer corresponds to the highest performance OVPD-grown structures. The OVPD device has a higher fill factor (*FF*) compared to that grown by VTE at the same thickness (200 nm), as shown in Figure 4.3, and Table 4.2. This difference is due to the low series resistance arising from the C_{70} nanocrystalline morphology in OVPD-grown active layers [31]. After aging for 250 hr, the 60 nm thick VTE-grown device exhibits a substantial drop in V_{OC}, from 0.91±0.01 V to 0.52±0.01 V (Figure 4.3b), due to the morphological degradation of the blocking layer. The 200 nm thick VTE-grown device also shows a decrease in V_{OC} from 0.91±0.01 V to 0.74±0.01 V, whereas the OVPD-grown device exhibits almost no change (V_{OC} = 0.91±0.01 V initially, V_{OC} = 0.89±0.01 V after aging). In addition, the device yield for the 60 nm thick VTE-grown population (30 devices) decreases from 93 % to 67 % after 250 hr. In contrast, 200 nm thick devices grown by both VTE and OVPD show only a few shorted devices after aging.

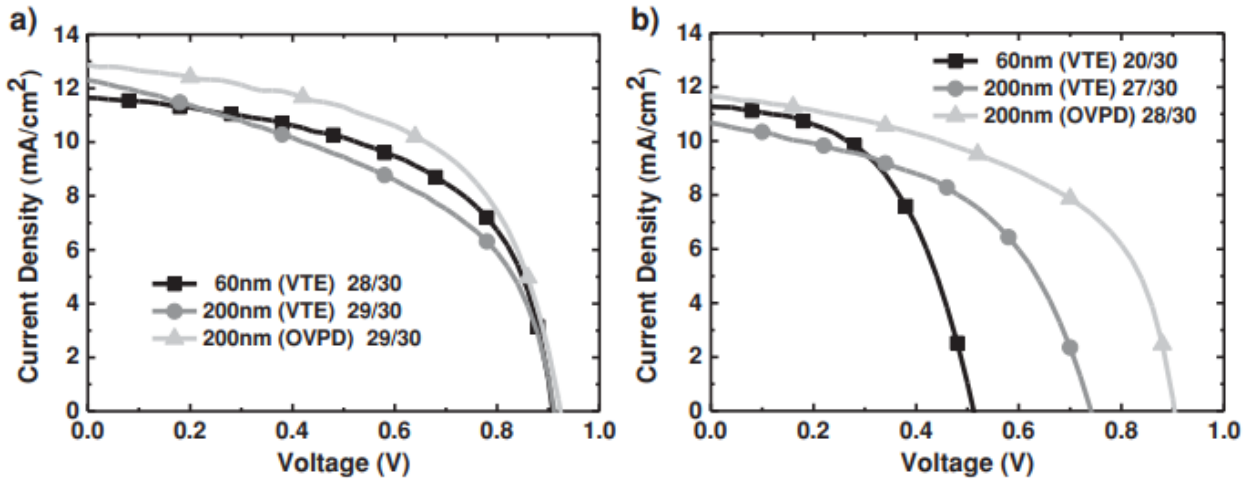

Figure 4.3. Current density-voltage (*J-V*) characteristics of DBP:C_{70} mixed heterojunction organic photovoltaic (OPV) cells with an 8 nm thick Bphen blocking layer and a 100 nm thick Ag cathode. The number of operational devices among the 30 grown on each substrate is specified in the legend. (a) Initial *J-V* characteristics of OPVs with 60 nm thick and 200 nm thick VTE-grown active layers, and a 200 nm thick OVPD-grown active layer. (b) *J-V* characteristics of the three devices after aging 250 hr.

Table 4.2 Performance of DBP:C_{70} mixed heterojunction OPVs grown by VTE or OVPD

Active layer thickness	J_{sc} [mA/cm^2]	V_{oc} [V]	*FF*	*PCE* [%]
As-grown				
60nm (VTE)	11.6±0.02	0.91±0.01	0.56±0.01	6.0±0.2
200nm (VTE)	12.3±0.02	0.91±0.01	0.48±0.01	5.3±0.2
200nm (OVPD)	12.9±0.02	0.91±0.01	0.56±0.01	6.7±0.2
After 250 hours of light illumination				
60nm (VTE)	11.2±0.02	0.52±0.01	0.52±0.01	3.1±0.02
200nm (VTE)	10.7±0.02	0.74±0.01	0.49±0.01	4.0±0.02
200nm (OVPD)	11.6±0.02	0.89±0.01	0.52±0.01	5.5±0.02

4.2.3. Origin of electrical shorts and V_{OC} changes in OPVs

As shown in the fluorescence microscope images in Figure 4.4, we find that Bphen protrusions pierce the active layer after 75 hr for the VTE-grown sample. These protrusions contain Ag, identified by three peaks (at 2.98, 3.14, and 3.35 keV) in the energy dispersive spectra (EDS; see Figure 4.4c). This suggests that device shorts are a result of the diffusion of Ag atoms through the grain boundaries between crystallites in the aged Bphen layer [34]. Such protrusions are completely absent for the OVPD-grown sample (Figure 4.4b), thus greatly reducing the possibility of shorts.

The decrease in V_{OC} can be understood using the expression for the open circuit voltage of organic heterojunctions, where [35]:

$$qV_{OC} = \Delta E_{HL} - n_A k_B T \ln[J_0/J_{sc}] \quad (4.1)$$

with $$\Delta E_{HL} = \Phi_a + \Phi_c + qV_{bi}. \quad (4.2)$$

Here, ΔE_{HL} is the energy difference between the lowest unoccupied molecular orbital (LUMO) of the acceptor (C_{70}) and the highest occupied molecular orbital (HOMO) of the donor (DBP), n_A is the ideality factor due to charge recombination at traps in the acceptor layer, k_B is Boltzmann's constant, T is the temperature, and J_0 is the reverse-bias saturation current density. Also, Φ_a and Φ_c are the hole and electron injection barriers at the anode and cathode, respectively, and V_{bi} is the built-in potential determined by the difference in contact work functions: $V_{bi} = WF_a - WF_c$. Figure 4.5 shows the change in capacitance (C)–voltage (V) characteristics after 250 hr of

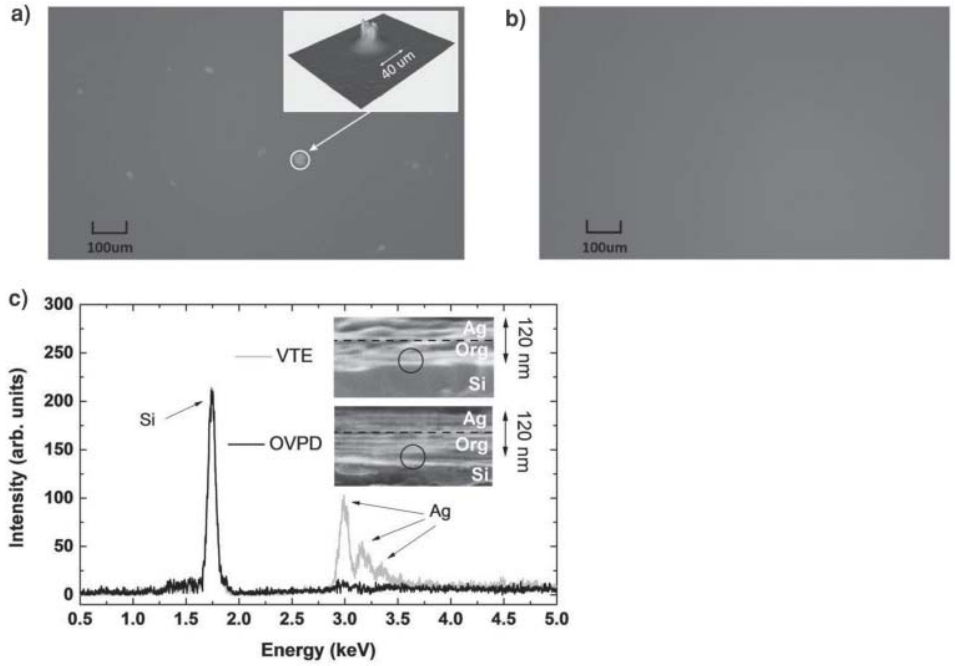

Figure 4.4. Fluorescence microscope image of glass/12 nm thick tris(8-hydroxyquinolinato) aluminum (Alq_3)/1:10 (by vol.) DBP:C_{70} (60 nm) grown by (a) VTE or (b) OVPD/Bphen(8 nm)/Ag(100 nm) after aging 75 hr. 3D image reconstruction of protrusion (Inset) from multiple slices of the 2D images is shown. (c) Energy dispersive spectra (EDS) of DBP:C_{70} (60 nm thick grown by VTE or OVPD)/Bphen(8 nm)/Ag(60 nm) films on a Si substrate after aging 75 hr. Elements corresponding to each peak are indicated. Inset: Cross-sectional SEM images of each sample with EDS probe area indicated (circle). The probe area is located well below the Ag/organic interface to ensure that only areas far away from the contact are sampled for the presence of Ag.

aging for the 60 nm and 200 nm active-layer-thickness VTE-grown devices, and for the 200 nm thick OVPD-grown device. Voltage shifts were observed in the forward-bias region after the aging: ΔV = 0.39±0.03 V, 0.18±0.02 V, and 0.03±0.01 V, respectively. From the Equation 4.1 and 4.2, resulting ΔV could be either $\Delta\Phi_c$ or ΔWF_c after the aging since the degradation exists only in the cathode side. Although it is not clear about ΔWF_c (i.e. ΔV_{bi}) from the $1/C^2$ *vs.* V plot [36], all of ΔV are comparable to the decrease in V_{OC} (0.38±0.01 V, 0.17±0.01 V, and 0.02±0.01 V; c.f. Table 4.2) of the devices. The origin of ΔV is due to the change in fixed charge (ΔQ) at the interface

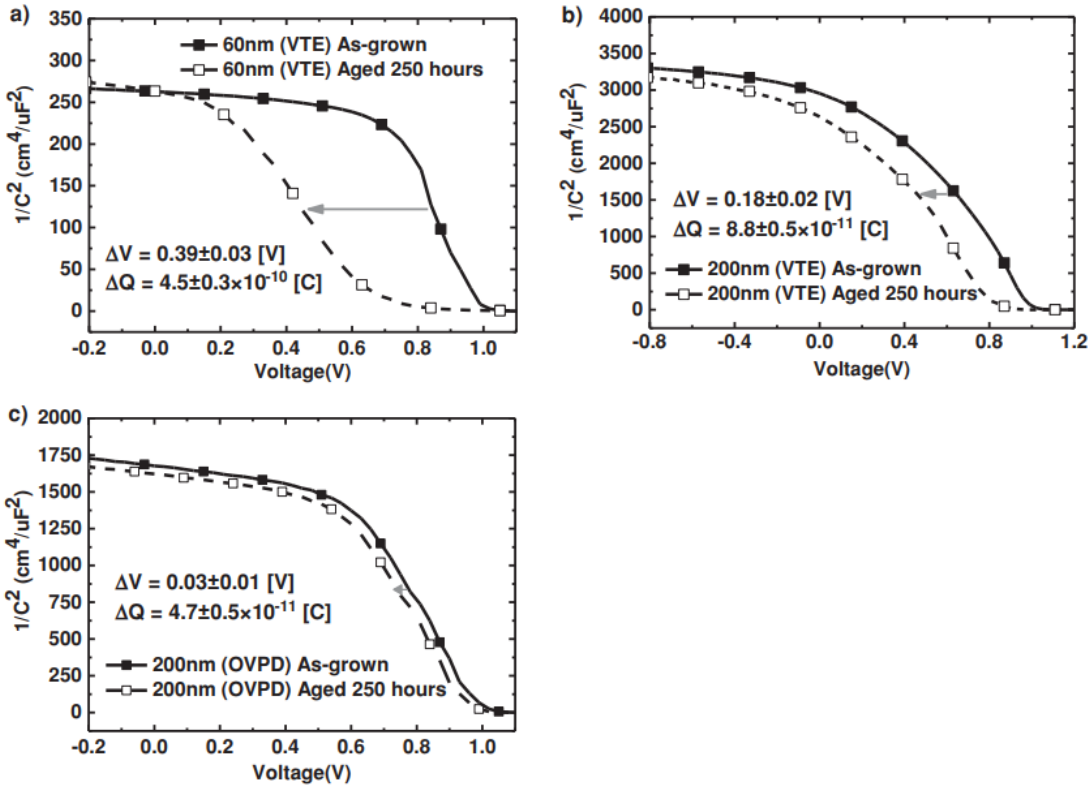

Figure 4.5. Capacitance-voltage ($1/C^2$ vs. V) characteristics of (a) 60 nm thick VTE-grown, (b) 200 nm thick VTE-grown, and (c) 200 nm thick OVPD-grown DBP:C_{70} active layer devices before and after aging for 250 hr. Voltage shifts (ΔV) are obtained from the voltage difference between the initial curve and one after the aging in the middle of the straight line (grey arrows), from which the change in the fixed charge density (ΔQ) is inferred.

between the active layer and the blocker, following $\Delta Q = C\Delta V$. The defects at the interface caused by morphological irregularities during layer crystallization introduce a substantially higher fixed charge density in the VTE-grown active layers. These interface states have the highest density in films that undergo the greatest crystallization: 60nm thick and 200 nm thick VTE-grown layers are therefore anticipated to have higher defect densities than 200 nm thick OVPD-grown layers. We, therefore, calculate the incremental increase in ΔQ after the aging. The 60 nm thick VTE-grown devices show the largest ΔQ = 4.5±0.3×10^{-10} C compared to ΔQ = 8.8±0.5×10^{-11} C for the 200 nm thick VTE-grown devices, and ΔQ = 4.7±0.5×10^{-11} C for the OVPD-grown devices. The decrease in V_{OC} with device age is the primary source of the decrease in *PCE* for both VTE-grown

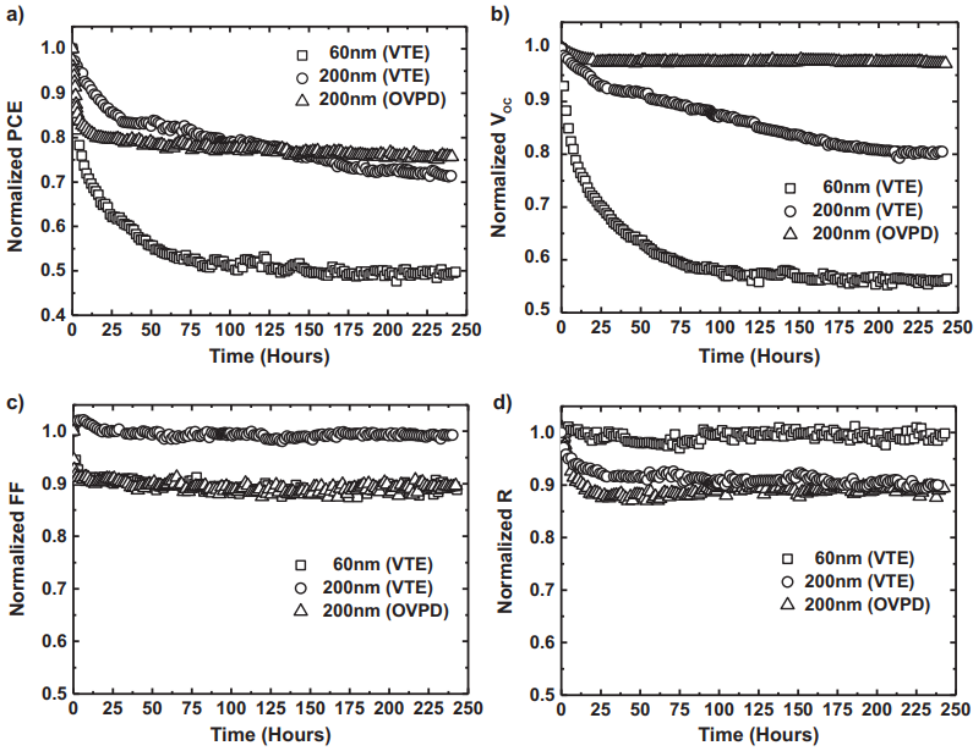

Figure 4.6. Aging characteristics of three DBP:C_{70} mixed heterojunction devices (60 nm thick, 200 nm thick active layer grown by VTE, and 200 nm thick active layer grown by OVPD) with an 8 nm thick Bphen blocking layer and a 100 nm thick Ag cathode. The normalized (a) power conversion efficiency, *PCE*, (b) open circuit-voltage, V_{oc}, (c) responsivity, *R*, and (d) fill factor, *FF*, over 250 hr of AM 1.5G illumination are shown.

devices, as shown in Figure 4.6. While both VTE-grown devices show monotonic decreases in V_{OC} *vs.* time, the effect of Bphen morphology more rapidly impacts the thin active layer device performance. In the 200 nm thick OVPD-grown device, however, both responsivity and *FF* decrease by only 11±1% and 9±1% from their initial values respectively, during the first 25 hours (corresponding to initial burn-in losses [37]). After this, the device performance is stable for the following 225 hr, showing a clear distinction from the VTE-grown devices.

4.3. Conclusion

In summary, the effect of morphological changes of the Bphen blocking layer over time on device performance was investigated for DBP:C_{70} mixed heterojunction OPVs whose active regions are grown by either VTE or OVPD. The Bphen blocking layer tends to crystallize which results in a decrease V_{OC} due to the accumulation of charge at the active-layer/Bphen interface. Morphological degradation not only affects device performance but also leads to electrical shorts —an effect that is mitigated by growing thicker active layers, and is entirely eliminated by the use of OVPD-grown active layers. The rough surface of the nanocrystalline OVPD-grown active layer pins the Bphen morphology, thereby hindering its transformation. This, in turn, results in OPVs that maintain both a high V_{OC} and yield after 250 hr of operation.

4.4. Experimental details

Atomic force microscope images were obtained using a Bruker Dimension Icon AFM in the tapping mode. X-ray diffraction patterns were obtained in the Bragg-Brentano configuration on organic films deposited on sapphire substrates. Fluorescence microscope images were recorded

with an Olympus BX-61 motorized microscope for the following structures: Glass/12 nm thick tris(8-hydroxyquinolinato) aluminum (Alq_3)/1:10 (by vol.) DBP:C_{70}(60 nm grown by either VTE or OVPD)/Bphen(8 nm)/Ag(100 nm). The thickness of the fluorescent (Alq_3) layer was adjusted until sufficient contrast between the protrusions and the fluorescence background emission was clearly observed. Scanning electron microscope (SEM) images were acquired using a Hitachi SU8000 in-line SEM equipped with an energy dispersive spectrometry (EDS) microprobe at 10kV. The cross-sectional images were acquired on layers consisting of 1:10 (by vol.) DBP:C_{70}(60 nm grown by either VTE or OVPD)/Ag(60 nm) deposited on Si substrates. The samples were cleaved after aging. The Ag and organic bulk layers were distinguished from the Si substrate using EDS. Samples were aged under simulated air mass 1.5 global (AM1.5G) illumination in an ultra-high purity (H_2O, O_2 < 1ppm) N_2-filled glovebox. Intensity was calibrated using a National Renewable Energy Laboratory (NREL)-traceable KG-5 filtered Si reference cell.

Organic PV cells were prepared as follows. 2.5 cm^2 square glass substrates were pre-patterned with rectangular, 150 nm thick indium tin oxide (ITO) patterns for each contact. The substrates were subsequently cleaned in tergitol, de-ionized water, twice with acetone, and twice with isopropanol for > 5 min each. Ultraviolet-ozone treatment was applied for 10 min followed by 1 min snow-cleaning [38] with CO_2. Substrates were transferred to the glovebox, and a shadow mask with 1.2 cm^2 square openings was aligned to the ITO pattern for deposition of all layers except cathode. Both MoO_3, and Bphen were deposited at 1Å/s in a VTE chamber (base pressure ~10^{-7}torr). Thicknesses and deposition rates were monitored using quartz crystal monitors. DBP and C_{70} were co-evaporated at 0.2Å/s, 2.0Å/s, leading to 1:10 volume ratio. The OVPD growth employed a multi-barrel quartz reactor with a 10 sccm (standard cubic centimeters per minute) N_2 flow used in each source barrel along with a 6 sccm dilution flow in the main reactor tube,

maintained at a pressure of 0.28 torr. The DBP barrel was heated to 375±2 ˚C, and the C_{70} barrel to 520±2 ºC inside the reactor having three temperature zones of 560, 500, and 440˚C to reach the same deposition rate as in VTE growth. A shadow mask was aligned to the anode patterns to define a 2 mm^2 device area via the deposition of the Ag cathode by VTE at 1Å/s. Following deposition, the devices were packaged in an ultrahigh purity N_2 environment by sealing a 1.6 cm^2 cover glass to the substrate using UV-curable epoxy applied along its periphery.

Current density (*J*) *vs. V* characteristics were measured under AM1.5G illumination using an Agilent 4156C parameter analyzer. Additionally, the wavelength-dependent external quantum efficiency (*EQE*) was recorded using a fiber-coupled Xe arc lamp at 200 Hz with a Stanford SR830 DSP lock-in amplifier. Then the short circuit current density, J_{sc}, was calculated by integrating the *EQE* over the AM 1.5G solar spectrum. The intensity of the solar simulator was set such that J_{sc} was equal to that obtained from the integrated *EQE*. The measured and calculated *J-V* agree to within 4%. Capacitance-voltage characteristics were obtained using an HP 4284A precision LCR meter equipped with an Agilent B1500A semiconductor device analyzer. A 25mV amplitude AC signal at 1 kHz frequency was applied.

The encapsulated devices were aged at 50±5 ℃ under a large area (210 mm^2) AM 1.5G Xe arc lamp solar simulator. The *J-V* characteristics of each device were automatically acquired every 30 min using a computer-controlled semiconductor parameter analyzer.

4.5. References

[1] W. Zeng, K. S. Yong, Z. M. Kam, F. Zhu, and Y. Li, "Effect of blend layer morphology on performance of ZnPc:C60-based photovoltaic cells," *Appl. Phys. Lett.*, vol. 97, no. 13, p. 133304, Sep. 2010.

[2] O. P. Lee *et al.*, "Efficient Small Molecule Bulk Heterojunction Solar Cells with High Fill Factors via Pyrene-Directed Molecular Self-Assembly," *Adv. Mater.*, vol. 23, no. 45, p. 5359, Dec. 2011.

[3] Y. Zhou *et al.*, "Phase separation of co-evaporated ZnPc:C60 blend film for highly efficient organic photovoltaics," *Appl. Phys. Lett.*, vol. 100, no. 23, p. 233302, 2012.

[4] J. D. Zimmerman *et al.*, "Control of interface order by inverse quasi-epitaxial growth of squaraine/fullerene thin film photovoltaics," *ACS Nano*, vol. 7, no. 10, pp. 9268–75, Oct. 2013.

[5] J. S. Kim, J. H. Park, J. H. Lee, J. Jo, D.-Y. Kim, and K. Cho, "Control of the electrode work function and active layer morphology via surface modification of indium tin oxide for high efficiency organic photovoltaics," *Appl. Phys. Lett.*, vol. 91, no. 11, p. 112111, 2007.

[6] J. M. Szarko *et al.*, "When function follows form: Effects of donor copolymer side chains on film morphology and BHJ solar cell performance," *Adv. Mater.*, vol. 22, no. 48, pp. 5468–72, Dec. 2010.

[7] B. Ray and M. A. Alam, "Random vs regularized OPV: Limits of performance gain of organic bulk heterojunction solar cells by morphology engineering," *Sol. Energy Mater. Sol. Cells*, vol. 99, pp. 204–212, Apr. 2012.

[8] S. Bertho *et al.*, "Effect of temperature on the morphological and photovoltaic stability of bulk heterojunction polymer:fullerene solar cells," *Sol. Energy Mater. Sol. Cells*, vol. 92, no. 7, pp. 753–760, Jul. 2008.

[9] M. F. Lo *et al.*, "Operation stability enhancement in organic photovoltaic device by a metal doped organic exciton blocking layer," *Appl. Phys. Lett.*, vol. 97, no. 14, p. 143304, 2010.

[10] T. Y.-H. Lee, Q. Wang, J. U. Wallace, and S. H. Chen, "Temporal stability of blue phosphorescent organic light-emitting diodes affected by thermal annealing of emitting layers," *J. Mater. Chem.*, vol. 22, no. 43, p. 23175, 2012.

[11] C. H. Peters, I. T. Sachs-Quintana, J. P. Kastrop, S. Beaupre´, M. Leclerc, and M. D. Mcgehee, "High Efficiency Polymer Solar Cells with Long Operating Lifetimes," *Adv.*

Energy Mater., vol. 1, no. 4, p. 491, Jul. 2011.

[12] F. C. Krebs, *Stability and Degradation of Organic and Polymer Solar Cells*, 1st ed. John Wiley & Sons, Ltd, 2012.

[13] M. Shtein, P. Peumans, J. B. Benziger, and S. R. Forrest, "Micropatterning of small molecular weight organic semiconductor thin films using organic vapor phase deposition," *J. Appl. Phys.*, vol. 93, no. 7, p. 4005, Apr. 2003.

[14] F. Yang, M. Shtein, and S. R. Forrest, "Morphology control and material mixing by high-temperature organic vapor-phase deposition and its application to thin-film solar cells," *J. Appl. Phys.*, vol. 98, no. 1, p. 14906, 2005.

[15] F. Yang, M. Shtein, and S. R. Forrest, "Controlled growth of a molecular bulk heterojunction photovoltaic cell," *Nat. Mater.*, vol. 4, no. 1, pp. 37–41, Dec. 2004.

[16] S. R. Forrest, "The path to ubiquitous and low-cost organic electronic appliances on plastic," *Nature*, vol. 428, no. 6986, pp. 911–8, Apr. 2004.

[17] M. Schwambera *et al.*, "OLED Manufacturing by Organic Vapor Phase Deposition Review of the OVPD Technology Scaling of the OVPD technology," *SID Symp. Dig. Tech. Pap.*, vol. 34, no. 1, pp. 1419–1421, 2003.

[18] J. Kreis, M. Schwambera, D. Keiper, M. Gersdorff, M. Long, and M. Heuken, "Organic Vapor Phase Deposition (OVPD) for efficient OLED manufacturing: the specific advantages and possibilities of carrier-gas enhanced vapor phase deposition for the manufacturing of organic thin film devices," *Proc. SPIE*, vol. 8476, p. 84761L, Sep. 2012.

[19] R. R. Lunt, B. E. Lassiter, J. B. Benziger, and S. R. Forrest, "Organic vapor phase deposition for the growth of large area organic electronic devices," *Appl. Phys. Lett.*, vol. 95, no. 23, p. 233305, 2009.

[20] C. Rolin, K. Vasseur, J. Genoe, and P. Heremans, "Growth of pentacene thin films by in-line organic vapor phase deposition," *Org. Electron.*, vol. 11, no. 1, pp. 100–108, Jan. 2010.

[21] T. X. Zhou, T. Ngo, J. J. Brown, M. Shtein, and S. R. Forrest, "Stable and efficient electrophosphorescent organic light-emitting devices grown by organic vapor phase deposition," *Appl. Phys. Lett.*, vol. 86, no. 2, p. 21107, 2005.

[22] J. Y. Kim, T. Yasuda, Y. S. Yang, and C. Adachi, "Bifunctional star-burst amorphous molecular materials for OLEDs: achieving highly efficient solid-state luminescence and carrier transport induced by spontaneous molecular orientation," *Adv. Mater.*, vol. 25, no.

19, pp. 2666–71, May 2013.

[23] T. Zhang *et al.*, "Efficient Triplet Application in Exciplex Delayed-Fluorescence OLEDs Using a Reverse Intersystem Crossing Mechanism Based on a ΔES-T of around Zero," *ACS Appl. Mater. Interfaces*, vol. 6, no. 15, pp. 11907–14, Aug. 2014.

[24] X. Xiao, J. D. Zimmerman, B. E. Lassiter, K. J. Bergemann, and S. R. Forrest, "A hybrid planar-mixed tetraphenyldibenzoperiflanthene/C70 photovoltaic cell," *Appl. Phys. Lett.*, vol. 102, no. 7, p. 73302, 2013.

[25] O. L. Griffith and S. R. Forrest, "Exciton management in organic photovoltaic multidonor energy cascades," *Nano Lett.*, vol. 14, no. 5, pp. 2353–8, May 2014.

[26] H. Kanno, R. J. Holmes, Y. Sun, S. Kena-Cohen, and S. R. Forrest, "White Stacked Electrophosphorescent Organic Light-Emitting Devices Employing MoO3 as a Charge-Generation Layer," *Adv. Mater.*, vol. 18, no. 3, pp. 339–342, Feb. 2006.

[27] J. H. Seo *et al.*, "Highly efficient white organic light-emitting diodes using two emitting materials for three primary colors (red, green, and blue)," *Appl. Phys. Lett.*, vol. 90, no. 20, p. 203507, 2007.

[28] B. W. D'Andrade, S. R. Forrest, and A. B. Chwang, "Operational stability of electrophosphorescent devices containing p and n doped transport layers," *Appl. Phys. Lett.*, vol. 83, no. 19, p. 3858, 2003.

[29] M. Tavakkoli, R. Ajeian, M. Nakhaee Badrabadi, S. Saleh Ardestani, S. M. H. Feiz, and K. Elahi Nasab, "Progress in stability of organic solar cells exposed to air," *Sol. Energy Mater. Sol. Cells*, vol. 95, no. 7, pp. 1964–1969, Jul. 2011.

[30] P. Kathirgamanathan *et al.*, "Novel Phenanthroline Derivatives for Electron Transport in Organic Light-emitting Diodes," *Chem. Lett.*, vol. 39, no. 11, pp. 1222–1224, 2010.

[31] B. Song, C. Rolin, J. D. Zimmerman, and S. R. Forrest, "Effect of mixed layer crystallinity on the performance of mixed heterojunction organic photovoltaic cells," *Adv. Mater.*, vol. 26, no. 18, pp. 2914–8, May 2014.

[32] M. Valsakumar *et al.*, "Crystal structure and disorder in solid C70," *Phys. Rev. B. Condens. Matter*, vol. 48, no. 12, pp. 9080–9085, Sep. 1993.

[33] H. Li, J.-L. Brédas, and C. Lennartz, "First-principles theoretical investigation of the electronic couplings in single crystals of phenanthroline-based organic semiconductors," *J. Chem. Phys.*, vol. 126, no. 16, p. 164704, Apr. 2007.

[34] F. C. Krebs and K. Norrman, “Analysis of the Failure Mechanism for a Stable Organic Photovoltaic During 10 000 h of Testing,” *Prog. photovoltaics Res. Appl.*, vol. 15, no. September, pp. 697–712, 2007.

[35] N. C. Giebink, G. P. Wiederrecht, M. R. Wasielewski, and S. R. Forrest, “Ideal diode equation for organic heterojunctions. I. Derivation and application,” *Phys. Rev. B*, vol. 82, no. 15, p. 155305, Oct. 2010.

[36] T. Kirchartz *et al.*, “Sensitivity of the Mott–Schottky Analysis in Organic Solar Cells,” *J. Phys. Chem. C*, vol. 116, no. 14, pp. 7672–7680, Apr. 2012.

[37] X. Tong, N. Wang, M. Slootsky, J. Yu, and S. R. Forrest, “Intrinsic burn-in efficiency loss of small-molecule organic photovoltaic cells due to exciton-induced trap formation,” *Sol. Energy Mater. Sol. Cells*, vol. 118, pp. 116–123, Nov. 2013.

[38] N. Wang, J. D. Zimmerman, X. Tong, X. Xiao, J. Yu, and S. R. Forrest, “Snow cleaning of substrates increases yield of large-area organic photovoltaics,” *Appl. Phys. Lett.*, vol. 101, no. 13, p. 133901, 2012.

Chapter 5

Control of morphology in electron-conducting buffers via organic vapor phase deposition

This chapter is adapted from the peer-reviewed publication: *Nano Lett.*, 16, 3905 (2016)

5.1. Introduction

The power conversion efficiencies of small molecular-weight organic photovoltaic (OPV) cells depend, among other factors, on the composition and morphology of the cathode buffer layer [1–4] that serves to block excitons from quenching at the contact, and to conduct electrons from the acceptor layer to the electrode. A recent and efficient "electron filtering buffer" design has been introduced that employs a mixture of a fullerene to conduct electrons along with a wide-energy gap matrix that blocks excitons [1, 5, 6]. It is expected that the properties of such filters depend critically on morphology, fullerene-to-matrix mixture, optical transparency, etc. Indeed, Bergemann, et al. have shown a strong dependence of conductivity on the concentration of the fullerene, with the percolation threshold for conductivity being unexpectedly low at < 20% for bathophrenanthroline (Bphen):C_{60} buffers [7]. In this context, the growth process of organic vapor phase deposition (OVPD) has proven to be a precise means to control thin film morphology required in such dilute mixtures [8–11]. For example, OVPD growth can yield films with long range crystalline order, thereby enhancing device performance [9], morphological stability [8], and yield [8, 12] when compared to devices grown by vacuum thermal evaporation (VTE). One

particular benefit of OVPD is the ability to control the thermodynamic conditions (e.g. carrier gas pressure, flow rate, and substrate temperature) during growth that can be used to vary the kinetic energy imparted on depositing molecules. This, in turn, affects the diffusion of organic molecules at the growth interface, and hence the crystallinity of the resulting thin film [13]. Indeed, the variation in carrier gas pressure can result in dramatic changes in thin-film morphology by inducing pronounced surface roughening due to gas-phase nucleation among other effects [14].

5.2. Results & Discussion

We demonstrate morphological control over fullerene-based electron-filtering buffer layers using OVPD by employing 3,5,3',5'-tetra(m-pyrid-3-yl)phenyl[1,1']biphenyl (BP4mPy) as a wide energy gap exciton blocker. This material has improved morphological stability compared with Bphen due to its high glass transition temperature [15]. We find that the morphology, and specifically the extent of the crystalline domains of C_{60} mixed into BP4mPy are a function of growth pressure, as supported by atomic force microscopy (AFM) and x-ray diffraction (XRD). The compound buffer grown at a nitrogen background pressure of P = 0.28 torr in the OVPD chamber shows the largest C_{60} crystallite size of 10 nm within the amorphous BP4mPy matrix. A further increase in growth pressure results in an amorphous mixture in which the crystalline C_{60} conductive "wires" are absent. In the space-charge limited current (SCLC) regime, we find that the electron mobility follows the crystallinity of C_{60} whose extent is controlled by the OVPD growth pressure. The mobility of the highest conductivity buffer is $6.1\pm0.5\times10^{-3}$ $cm^2/V\cdot s$, which is comparable to that of a neat, polycrystalline C_{60} thin-film (3.3×10^{-2} $cm^2/V\cdot s$). Tetraphenyldibenzoperiflanthene (DBP):C_{70} planar mixed heterojunction OPVs employing the BP4mPy:C_{60} electron-filtering buffer grown at 0.28 torr show a power-conversion efficiency *PCE*

= 8.0±0.2 % with a fill factor *FF* = 0.65±0.01, compared to *PCE* = 6.6±0.2 % and *FF* = 0.55±0.01 for an amorphous, VTE-grown buffer. We attribute this improvement to film morphology that is determined by the kinetic energy imparted to the molecules at the growth interface by the N_2 carrier gas in OVPD. By varying the gas pressure, we can vary the extent of fullerene crystallinity in the blends, achieving morphologies that range from amorphous to extended high conductivity C_{60} crystalline domains. Microscopic analysis is supported by molecular dynamic simulations indicating that distinct morphologies are the result of the control of molecular kinetics at the growth interface.

5.2.1. Morphology of BP4mPy:C_{60} electron-conducting buffer

The surface morphology of C_{60} and BP4mPy thin films are investigated using atomic force microscopy (AFM), with images of 10 nm thick C_{60} films grown at pressures of P_1 =0.17, P_2 =

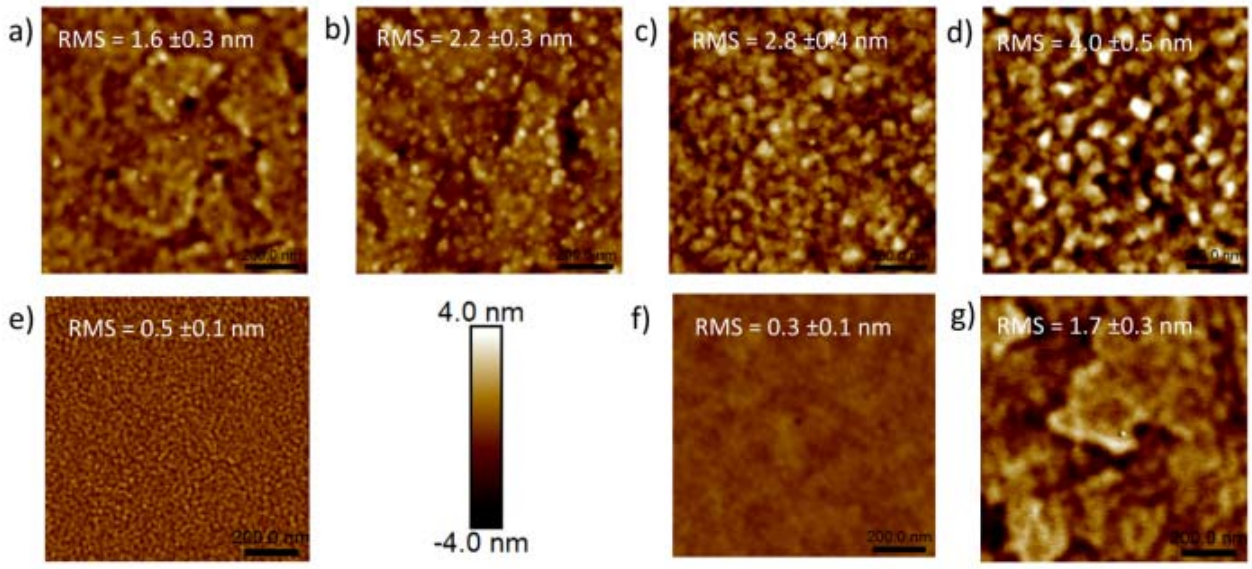

Figure 5.1**.** Atomic force microscope (AFM) images of 10 nm thick C_{60} films grown by organic vapor phase deposition (OVPD) at (a) 0.17 torr (b) 0.28 torr (c) 0.49 torr (d) 0.82 torr and (e) vacuum thermal evaporation (VTE). AFM image of 10 nm thick (f) BP4mPy and (g) BP4mPy:C_{60} (1:1 vol.) grown by OVPD at 0.28 torr. All thin-films are deposited on an ITO/MoO_3 10 nm/DBP:C_{70} (1:8 vol., 54 nm)/C_{70} (9 nm) surface. Root-mean-square (RMS) surface roughnesses are indicated.

0.28, P_3 = 0.49 and P_4 = 0.82 torr shown in Figure 5.1a-d, respectively. Cluster-like features suggestive of crystallite formation develop with increasing pressure. This is accompanied by an increase in surface roughness, from a root mean square value of 1.6±0.3 nm at P_1, to 4.0±0.5 nm at P_4. The diameter of a C_{60} cluster is ~10 nm in Figure 5.1d. In contrast, surface clustering is absent in the film grown by VTE suggesting a homogeneously amorphous film (Figure 5.1e). The surfaces of BP4mPy thin films grown by both VTE and OVPD are smooth and featureless as shown in Figure 5.1f. Further, the 1:1 (by vol.) BP4mPy:C_{60} film surface morphology does not show a pressure dependence when grown by OVPD (Figure 5.2). We conclude that the change in morphology under different growth pressures is confined to changes only in the regions C_{60} due to its propensity for crystallization into a face centered cubic (fcc) structure [16, 17], whereas BP4mPy is stable in the amorphous phase with a relatively high glass transition temperature (128 ^{o}C) [18].

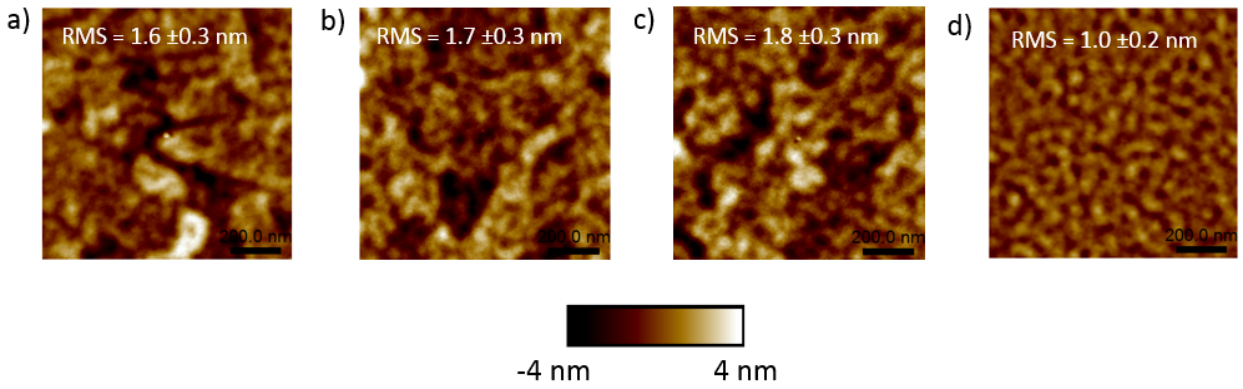

Figure 5.2. Atomic force microscope (AFM) images of 10 nm thick BP4mPy:C_{60} (1:1 vol.) films grown by organic vapor phase deposition (OVPD) at (a) 0.17 torr (b) 0.49 torr (c) 0.82 torr. (d) AFM image of 200 nm thick BP4mPy:C_{60} (1:1 vol.) grown by OVPD at 0.28 torr. All thin-films are deposited on an ITO/MoO_3 10 nm/DBP:C_{70} (1:8 vol., 54 nm) surface. Root-mean-square (RMS) surface roughnesses are indicated.

Structural information is obtained via XRD of 200 nm thick C_{60} films grown by OVPD for these same growth pressures, as shown in Figure 5.3a. Consistent with the development of C_{60} clusters, (Figure 5.1a-d), the peak at a diffraction angle of 2θ=10.93±0.03° corresponding to the (111) plane of the C_{60} fcc structure [16, 17] increases with pressure. In the 1:1 BP4mPy:C_{60} film, this peak emerges at P_1 = 0.17 torr, increasing to a maximum intensity at P_2 = 0.28 torr, and then declines as pressure is increased further until it disappears at P_4 = 0.82 torr (Figure 5.3b). Using Scherrer analysis of the peak broadening [19], we obtain an approximate average C_{60} crystallite size of 10±1 nm for the film at P_2. However, VTE-grown 1:1 BP4mPy:C_{60} films show no diffraction features from C_{60}, indicating that it is most likely amorphous.

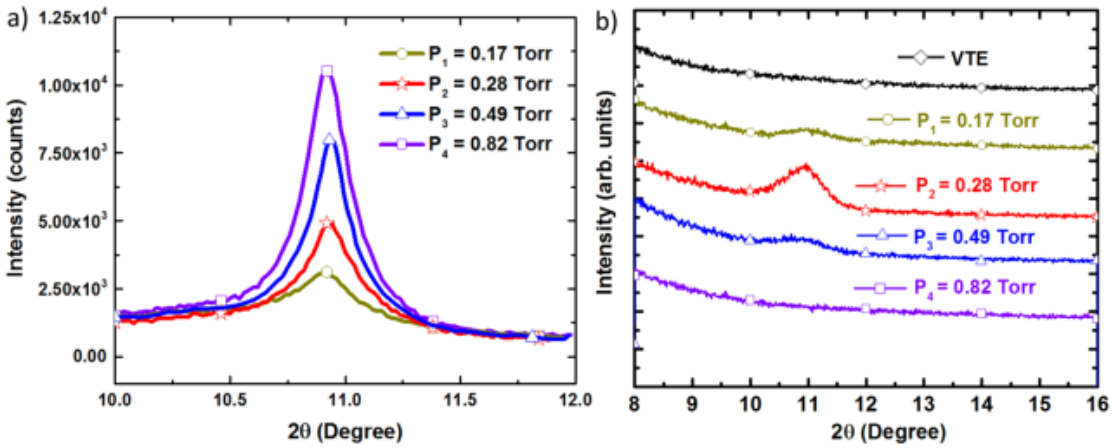

Figure 5.3. X-ray diffraction (XRD) using the Cu-Kα line in the Bragg-Brentano configuration of 200 nm thick (a) C_{60} and (b) BP4mPy:C_{60} (1:1 vol.) on sapphire substrates grown by OVPD at four different growth pressures (0.17, 0.28, 0.49, 0.82 torr).

5.2.2. Electrical property of BP4mPy:C_{60} electron-conducting buffer

The electron mobility (μ) of the mixed layer is obtained from the current density (J)-voltage (V) characteristics of an electron-only device in the space-charge limited current (SCLC) regime where [20]:

$$J = \frac{9}{8}\varepsilon\varepsilon_0\mu(E)\frac{V^2}{d^3} \tag{5.1}$$

with [21]
$$\mu(E) = \mu_0 \exp[\gamma(E)^{1/2}] \tag{5.2}$$

that assumes the mobility is limited by Frenkel-Poole intermolecular hopping. Here, ε is relative permittivity of the layer (≈3), ε_0 is the permittivity of free space, d is the film thickness, E is the electric field, μ_0 is zero-field mobility, and γ is the field-activation parameter that is a function of the degree of disorder of the film [22]. By fitting the *J-V* characteristics for the electron-only devices to these expressions (see Figure 5.4), we obtain μ_0, and γ for compound buffers grown under different growth conditions as listed in Table 5.1. We observe that μ_0 increases and γ decreases with the crystalline domain size of C_{60} (c.f. Figure 5.3b), indicating that electrons are

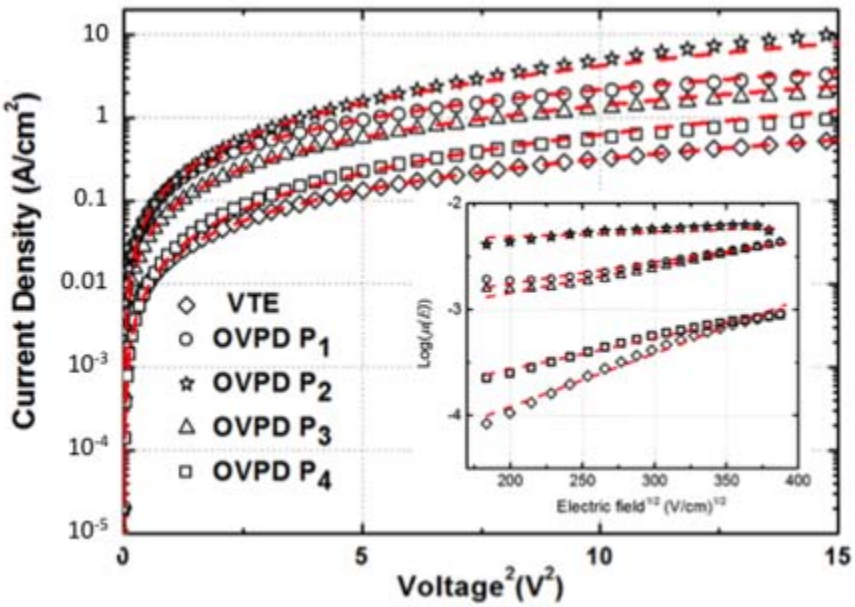

Figure 5.4. Current density-voltage characteristics of sapphire/Al (100 nm)/BP4mPy:C_{60} (1:1 vol., 200 nm)/NTCDA (10 nm)/LiF (1.5 nm)/Al (100 nm) electron-only devices. The BP4mPy:C_{60} blends were grown by OVPD at four different pressures (P_1=0.17, P_2=0.28, P_3=0.49, P_4=0.82 torr) or by VTE. Lines indicate fits based on space-charge limited current. (Inset) Logarithm of electron mobility versus the applied electric field for the electron-only devices.

conducted through the C_{60} domains within the BP4mPy matrix. The highest $\mu_0 = 6.1\pm0.5\times10^{-3}$ $cm^2/V\cdot s$ corresponds to buffers grown at P_2, which is comparable to 3.3×10^{-2} $cm^2/V\cdot s$ of neat, polycrystalline C_{60} thin films [23]. The lowest $\gamma = 4.6\pm0.5\times10^{-4}$ $(cm/V)^{1/2}$ is also observed in the buffer grown at P_2, providing additional evidence for structural order of C_{60} at this pressure. Electron-filtering buffers grown by VTE have $\mu_0 = 7.9\pm0.4\times10^{-5}$ $cm^2/V\cdot s$ with the largest $\gamma = 5.0\pm0.6\times10^{-3}$ $(cm/V)^{1/2}$, suggesting significant disorder within and between the C_{60} clusters.

Table 5.1 Zero-field mobility, μ_0, and field-activation parameter, γ, of BP4mPy:C_{60} mixed layers under different growth conditions

Growth Process	**Pressure [Torr]**	**μ_0 [$cm^2/(V\cdot s)$]**[a]	**γ x10^3 [$(cm/V)^{1/2}$]**[a]
VTE	10^{-7}	$7.9\pm0.4\times10^{-5}$	5.0±0.6
OVPD	0.17	$1.8\pm0.3\times10^{-3}$	2.0±0.7
OVPD	0.28	$6.1\pm0.5\times10^{-3}$	0.46±0.05
OVPD	0.49	$1.3\pm0.2\times10^{-3}$	2.5±0.5
OVPD	0.82	$1.6\pm0.1\times10^{-4}$	3.5±0.5

[a] Parameters are extracted from current density (J)-voltage (V) characteristics of the electron-only device. Electron-only devices have the following structure: Al (100 nm)/BP4mPy:C_{60} (1:1 vol., 200 nm)/NTCDA (10 nm)/LiF (1.5nm)/Al (100 nm). Errors are obtained from the deviations in the fitting.

5.2.3. Performance of mixed heterojunction OPVs with BP4mPy:C_{60} buffer

Figure 5.5a shows the performance of DBP:C_{70} planar-mixed heterojunction OPVs with the different electron-filtering buffers. The variations in performance primarily arise from differences in *FF* of the devices whose full characteristics are listed in Table 5.2. From Figure 5.5b, we observe that *FF* varies as a function of the growth pressure, following similar variations in μ_0 of the buffers

shown in Table 5.1. Therefore, we conclude that the *FF* is strongly dependent on the extraction of electron-polarons from the buffer; that is, as the extent of the C_{60} crystalline domains increases, the mobility and hence the *FF* are also increased. The OPV with the buffer grown at P_2 = 0.28 torr shows the highest *FF* = 0.65±0.01 and *PCE* = 8.0±0.2 %, compared to the device with the amorphous buffer grown by VTE whose *FF* and *PCE* are 0.55±0.01 and 6.6±0.2 %, respectively.

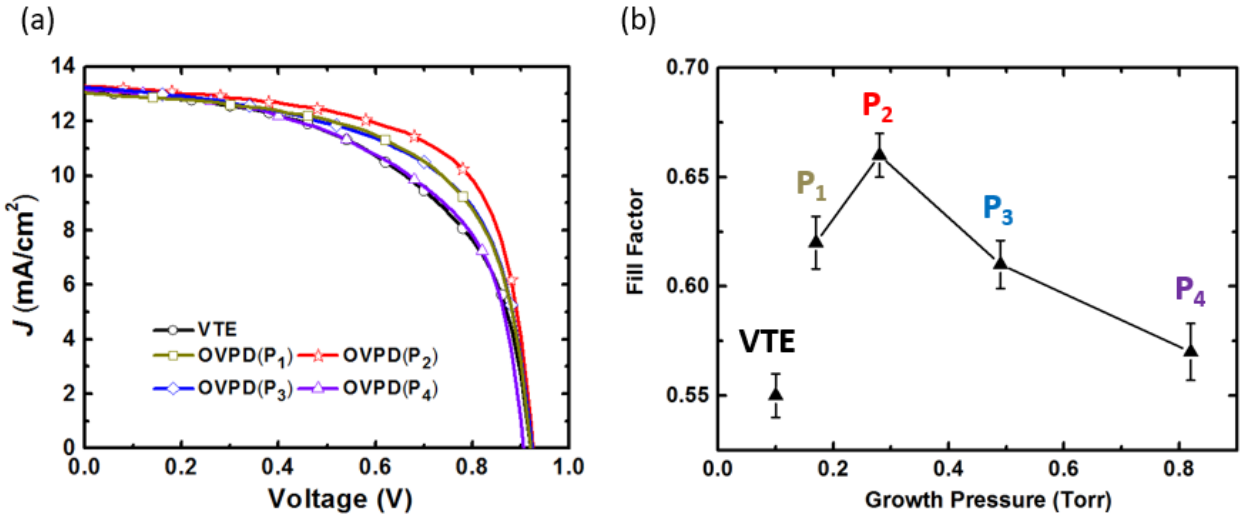

Figure 5.5. (a) Current density-voltage characteristics of DBP:C_{70} planar mixed heterojunction devices with BP4mPy:C_{60} (1:1 vol., 10 nm) buffers grown by VTE or OVPD at different growth pressures (0.17, 0.28, 0.49, 0.82 torr). (b) Fill factor (*FF*) variation of the devices in (a) depending on the growth pressure.

5.2.4. Molecular dynamic simulation of BP4mPy:C_{60} buffer

To understand the morphological dependence on the pressure, molecular dynamic simulations of the blend under different thermodynamic conditions used during growth have been performed. In OVPD, N_2 carrier gas imparts kinetic energy to adsorbate molecules to promote diffusion along the surface until the molecules find suitably low energy sites to stabilizes their location. Over a suitably small range of pressures such as those used in our experiments, we can express the dependence of kinetic energy on pressure as an equivalent small change in substrate

Table 5.2 Performance of DBP:C_{70} planar mixed heterojunction OPVs with 10 nm thick BP4mPy:C_{60} compound buffer layers

Growth Process	**Pressure [Torr]**	***Jsc* [mA/cm^2][a]**	***V_{OC}* [V][a]**	***FF*[a]**	***PCE* [%][a]**
VTE	10^{-7}	13.1±0.2	0.920±0.002	0.55±0.01	6.6±0.2
OVPD	0.17	13.2±0.2	0.920±0.002	0.62±0.01	7.5±0.2
OVPD	0.28	13.3±0.2	0.923±0.001	0.65±0.01	8.0±0.2
OVPD	0.49	13.2±0.2	0.922±0.001	0.61±0.01	7.4±0.2
OVPD	0.82	13.1±0.2	0.915±0.003	0.57±0.01	6.7±0.2

[a)] Error bars from standard deviation of four different samples.

temperature according to the ideal gas law. That is, if the temperature at pressure P_1 is T_1, then at a different pressure, P, the incremental kinetic energy is given by the canonical relationship:

$$\delta E_{kin}\left(T,P\right)=\frac{k_B(T_{eff}-T_1)}{k_BT_1}\delta E_{kin,0}(T_1,P_1)+\delta E_{kin,0}\left(T_1,P_1\right)=\left[\frac{k_BT_1\left(P/P_1-1\right)}{k_BT_1}+1\right]\delta E_{kin,0}\left(T_1,P_1\right) \quad (5.3)$$

where k_B is Boltzmann's constant and T_{eff} is the effective substrate temperature that leads to the increased energy. The increase in carrier gas pressure allows molecules to find lower energy sites due to their larger kinetic energy. In this case, T_{eff} represents the *equivalent* annealing temperature (as opposed to the actual temperature) that would impart the energy required for molecules to reorganize into the observed morphology. It remains for us to determine the activation energy barrier, $\delta E_{kin,0}$ that must be overcome for a molecule to have sufficient surface mobility to seek a

low energy site, rather than to be fixed at its point of initial incidence on the surface. From the data in Figure 5.3 and 5.4, and measurements of μ_0 and γ, we infer that nanocrystallites form at pressure P_1 = 0.17 torr, whereas when deposited in vacuum on room temperature substrates, the morphology is completely amorphous. An elevated temperature of T_1 = 350 K compared to the substrate temperature (= 297 K) was chosen as the kinetic energy in the presence of N_2 at P_1 was imparted to the molecules. Thus, we can set a lower limit to the activation energy for crystallite formation of $\delta E_{kin,0}$ = 4.5 meV. Following Equation 5.3, the molecular dynamics leading to different morphologies in the limited pressure range from P_1 to P_4 can be simulated.

Figure 5.6 shows the molecular dynamic simulation results for 32 C_{60} and 12 BP4mPy molecules that are initially randomly distributed in their own regions. The simulation proceeds by

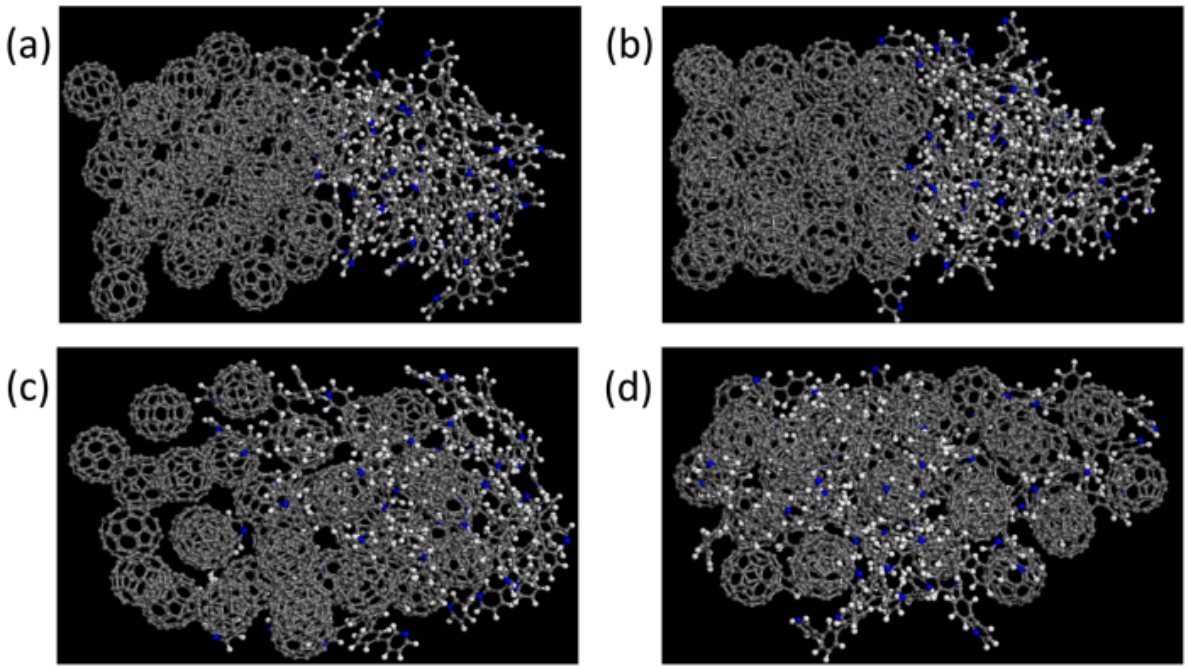

Figure 5.6. Molecular dynamic simulation results of an ensemble of 12 BP4mPy and 32 C_{60} molecules after simulated annealing with effective molecular kinetic energies of (a) δE_{kin} = 4.5 meV, (b) 7.4 meV, (c) 13 meV, (d) 21.7 meV corresponding to OVPD growth pressures of 0.17 torr, 0.28 torr, 0.49 torr, 0.82 torr, respectively. Note the ordered fcc C_{60} lattice in (b), and the almost complete intermixing of the equilibrium structure achieved at the highest pressure of 0.82 torr in (d).

allowing the ensemble of molecules to reach different equilibrium arrangements at each background pressure. At P_1 (T_{eff} = 350K), Figure 5.6a shows that there is minor reorganization within the C_{60} and BP4mPy regions with a slight intermixing at the interface. At P_2 (corresponding to δE_{kin} = 7.4 meV) in Figure 5.6b, C_{60} molecules clearly form into an fcc lattice, consistent with the significant crystallization observed for C_{60} under these growth conditions (c.f. Figure 5.3). As the growth pressure increases to P_3 (corresponding to δE_{kin} = 13.0 meV in Figure 5.6c), C_{60} and BP4mPy molecules inter-diffuse across the domain boundaries, and become completely blended in an amorphous mixture at the highest pressure, P_4 (δE_{kin} = 21.7 meV in Figure 5.6d). Finally, we calculated the total intermolecular vdW energies of each equilibrium morphology in Figure 5.6. The corresponding energies are -0.833 eV/molecule at P_1, -0.872 eV/molecule at P_2, -0.935 eV/molecule at P_3, and -1.01 eV/molecule at P_4. This implies that the ensemble energy decreases as the BP4mPy:C_{60} blend becomes more intermixed. Hence, increasing pressure and hence kinetic energy) drives the morphology to an increasingly stabilized structure. We tested whether the

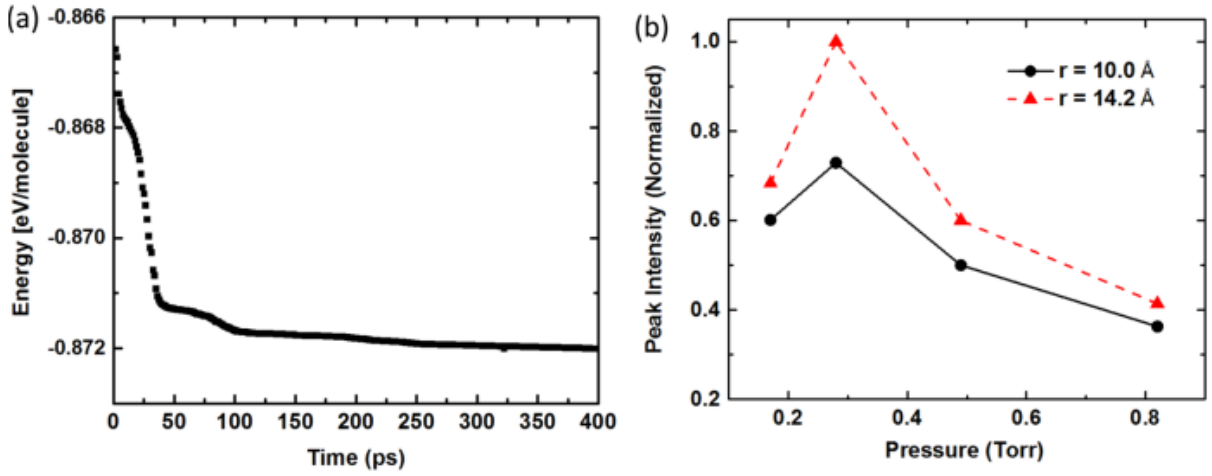

Figure 5.7. (a) Potential energy of the simulated molecular configuration annealed at T = 576 K (corresponding to P_2) as a function of simulation time. The equilibrium structure is achieved after approximately 150 ps. (b) Normalized peak intensities at 10.1 Å and 14.1 Å in radial distribution function (RDF) as a function of pressure in BP4mPy:C_{60} blends.

simulation is carried out over a sufficient period to ensure that the equilibrium structure is achieved. In Figure 5.7a, we show the simulation at T_2 = 576 K proceeding for 400 ps. A stable minimum energy is reached after approximately 150 ps. We further analyze each morphology with an intermolecular radial distribution function (RDF) [24] that quantifies the degree to which the fcc structure of C_{60} is achieved. Figure 5.7b shows the RDF peak intensity at 10.1 Å and 14.1 Å for the four different morphologies. The peak at 10.1 Å is from the nearest-neighbor distance of carbon atoms, and 14.1Å corresponds to the fcc lattice constant [24]. From Figure 5.7b, we find that the morphology at P_2 has the largest fcc content, with the degree of order decreasing at higher pressure. Once again this is consistent with observations obtained by XRD in Figure 5.3, and inferred from the conductivity of the films in Figure 5.4.

5.3. Conclusion

We demonstrate that the morphology of BP4mPy:C_{60} compound buffer can be controlled by the growth pressure in OVPD. Specifically, we find that the degree of C_{60} crystallite formation increases with pressure below P_2 = 0.28 torr, but then decreases with at higher pressures as the constituent molecules become increasingly intermixed. At the optimum growth pressure, the electron mobility is $6.1\pm0.5\times10^{-3}$ $cm^2/V\cdot s$, comparable to the mobility of crystalline C_{60} thin films. The DBP:C_{70} planar-mixed heterojunction OPVs with compound buffers grown at 0.28 torr have FF = 0.65±0.01 and PCE = 8.0±0.2 %, which are significantly improved compared with FF = 0.55±0.01 and PCE = 6.6±0.2 % for analogous devices grown by VTE. Morphological differences are understood by annealing of C_{60} domains in molecular dynamic simulation. These simulations are consistent with observation in that the highest degree of order in the C_{60} domains occurs at a pressure of 0.28 torr where the conductivity and other optoelectronic properties of the layers are optimized. It is expected that the conductivity of BP4mPy:C_{70} can be also enhanced by optimizing

OVPD growth conditions. Indeed, we can infer that this approach can be generally applied to any fullerene-based compound buffer.

5.4. Experimental details

Samples used for atomic force microscope (AFM) analysis have the following structures: ITO/MoO_3 (10 nm)/DBP:C_{70} (1:8 vol., 54 nm)/C_{70} (9 nm)/BP4mPy:C_{60} (1:1 vol., 10 nm). The AFM images were recorded by a Bruker Dimension Icon AFM in tapping mode. X-ray diffraction data for 200 nm thick BP4mPy:C_{60} layers were obtained using a Rigaku x-ray diffractometer in the Bragg-Brentano configuration using the Cu-Kα line at 40kV and 100mA. Electron-only devices have the following structure for space charge limited current measurements: Sapphire/Al (100 nm)/BP4mPy:C_{60} (1:1 vol., 200 nm)/NTCDA (10 nm)/LiF (1.5nm)/Al (100 nm). NTCDA was used to block hole conduction [4], and the LiF/Al top contact enabled efficient electron injection [25]. An Agilent 4156C parameter analyzer was used to measure current-voltage characteristics. Both μ_0 and γ were determined from fits to Equation 5.2.

OPV devices have the following structure: ITO/MoO_3 (10 nm)/DBP:C_{70} (1:8 by vol., 54 nm)/C_{70} (9 nm)/BP4mPy:C_{60} (1:1 by vol., 10 nm)/Ag (100 nm). Glass substrates were pre-coated with ITO (R_s = 20Ω/□). Substrates were cleaned with tergitol, deionized water, acetone, and isopropanol for 5 min each. Ultraviolet (UV)-ozone treatment was applied for 10 min, followed by CO_2 snow-cleaning for 1 min [26]. All layers except BP4mPy:C_{60} layer were grown by VTE. The device area (4.9 mm^2) is defined by the 2.5 mm-diameter shadow mask circular openings through which Ag is deposited. The VTE deposition rate was monitored by quartz crystal microbalance. For OVPD growth, 2 sccm of N_2 was injected into each source barrel and the main reactor, and a total of 6 sccm of N_2 was maintained during the growth. Substrates were water-

cooled at 24ºC. Temperatures of source barrels were adjusted to maintain deposition rates of 0.5Å/s. Thicknesses were calibrated ex-situ; a Si substrate was included to enable ellipsometric thickness measurement after deposition. All devices were fabricated in ultra-high purity (H_2O, O_2 <1 ppm) N_2-filled glovebox without exposure to atmosphere.

Molecular dynamic simulations were performed using Materials Studio v8.0 (Biovia Corp., San Diego, CA) along with the Forcite module for simulated annealing. Velocity scaling [27] was chosen to ensure reliable temperature control during the 250 ps simulated annealing. A Dreiding forcefield [28] 6-12 Lennard-Jones potential function was applied. As an initial condition, 32 C_{60} and 12 BP4mPy molecules were initially distributed in each region within 14.2 Å × 14.2 Å × 28.4 Å box. The initial temperature is set at 297 K based on the actual substrate temperature used during OVPD growth. Annealing temperatures corresponding to different growth pressures were determined based on ideal gas law (T_{eff} in Equation 5.3). The annealing cycle is repeated 3 times for 250 ps followed by geometric optimization, which ensures final molecular configuration at each annealing temperature has reached lowest energy sites. Intermolecular van der Waals energies were then calculated for each molecular configuration.

5.5. References

[1] X. Xiao, K. J. Bergemann, J. D. Zimmerman, K. Lee, and S. R. Forrest, "Small-Molecule Planar-Mixed Heterojunction Photovoltaic Cells with Fullerene-Based Electron Filtering Buffers," *Adv. Energy Mater.*, vol. 4, no. 7, May 2014.

[2] H.-W. Lin *et al.*, "An effective bilayer cathode buffer for highly efficient small molecule organic solar cells," *Org. Electron.*, vol. 13, no. 10, pp. 1925–1929, 2012.

[3] J. Yu, N. Wang, Y. Zang, and Y. Jiang, "Organic photovoltaic cells based on TPBi as a cathode buffer layer," *Sol. Energy Mater. Sol. Cells*, vol. 95, no. 2, pp. 664–668, 2011.

[4] B. E. Lassiter *et al.*, "Organic photovoltaics incorporating electron conducting exciton blocking layers," *Appl. Phys. Lett.*, vol. 98, no. 2011, pp. 2012–2015, 2011.

[5] O. L. Griffith *et al.*, "Charge transport and exciton dissociation in organic solar cells consisting of dipolar donors mixed with C," *Phys. Rev. B*, vol. 92, no. 8, p. 85404, 2015.

[6] X. Che, X. Xiao, J. D. Zimmerman, D. Fan, and S. R. Forrest, "High-Efficiency, Vacuum-Deposited, Small-Molecule Organic Tandem and Triple-Junction Photovoltaic Cells," *Adv. Energy Mater.*, Aug. 2014.

[7] K. J. Bergemann, J. A. Amonoo, B. Song, P. F. Green, and S. R. Forrest, "Surprisingly High Conductivity and E ffi cient Exciton Blocking in Fullerene/Wide-Energy-Gap Small Molecule Mixtures," *Nano Lett.*, vol. 15, no. 6, pp. 3994–3999, 2015.

[8] B. Song, Q. C. Burlingame, K. Lee, and S. R. Forrest, "Reliability of Mixed-Heterojunction Organic Photovoltaics Grown via Organic Vapor Phase Deposition," *Adv. Energy Mater.*, pp. 1–6, 2015.

[9] B. Song, C. Rolin, J. D. Zimmerman, and S. R. Forrest, "Effect of mixed layer crystallinity on the performance of mixed heterojunction organic photovoltaic cells.," *Adv. Mater.*, vol. 26, no. 18, pp. 2914–8, May 2014.

[10] R. R. Lunt, J. B. Benziger, and S. R. Forrest, "Growth of an ordered crystalline organic heterojunction," *Adv. Mater.*, vol. 19, no. 23, pp. 4229–4233, 2007.

[11] F. Yang, M. Shtein, and S. R. Forrest, "Controlled growth of a molecular bulk heterojunction photovoltaic cell," *Nat. Mater.*, vol. 4, no. 1, pp. 37–41, Dec. 2004.

[12] R. R. Lunt, B. E. Lassiter, J. B. Benziger, and S. R. Forrest, "Organic vapor phase deposition for the growth of large area organic electronic devices," *Appl. Phys. Lett.*, vol. 95, no. 23, p. 233305, 2009.

[13] M. Shtein, H. F. Gossenberger, J. B. Benziger, and S. R. Forrest, "Material transport regimes and mechanisms for growth of molecular organic thin films using low-pressure organic vapor phase deposition," *J. Appl. Phys.*, vol. 89, p. 1470, 2001.

[14] C. Rolin *et al.*, "Vapor Phase Growth of Functional Pentacene Films at Atmospheric Pressure," *Adv. Funct. Mater.*, vol. 22, no. 23, pp. 5050–5059, Jul. 2012.

[15] S. J. Su, D. Tanaka, Y. J. Li, H. Sasabe, T. Takeda, and J. Kido, "Novel four-pyridylbenzene-armed biphenyls as electron-transport materials for phosphorescent OLEDs," *Org. Lett.*, vol. 10, no. 5, pp. 941–944, 2008.

[16] R. M. Fleming *et al.*, "Diffraction symmetry in crystalline, close-packed," *Mat. Res. Soc. Symp. Proc.*, vol. 206, pp. 691–695, 1991.

[17] K. Ota, M. Makoto, E. L. Milford, G. a. Mackin, H. L. Weiner, and D. a. Hafler, "Solid C60 : a new from of carbon,", *Nature*, vol. 346, pp. 183–187, 1990.

[18] P. Kathirgamanathan *et al.*, "Novel Phenanthroline Derivatives for Electron Transport in Organic Light-emitting Diodes," *Chem. Lett.*, vol. 39, no. 11, pp. 1222–1224, 2010.

[19] A. L. Patterson, "The Scherrer Formula for X-Ray Particle Size Determination", *Physical Review*, vol. 56, no. 10, pp. 978–982, 1939.

[20] P. Mark and W. Helfrich, "Space-Charge-Limited Currents in Organic Crystals," *J. Appl. Phys.*, vol. 33, no. 1, p. 205, 1962.

[21] L. B. Schein, A. Peled, and D. Glatz, "The electric field dependence of the mobility in molecularly doped polymers," *J. Appl. Phys.*, vol. 66, no. 2, pp. 686–692, 1989.

[22] A. Ioannidis, "Current – voltage characteristic of organic light emitting diodes," *Appl. Phys. Lett.*, vol. 72, no. 23, pp. 3038–3040, 1998.

[23] R. Pandey, A. a. Gunawan, K. A. Mkhoyan, and R. J. Holmes, "Efficient organic photovoltaic cells based on nanocrystalline mixtures of boron subphthalocyanine chloride and C60," *Adv. Funct. Mater.*, vol. 22, no. 3, pp. 617–624, 2012.

[24] C. I. Wang, C. H. Hsu, C. C. Hua, and S. a. Chen, "Molecular dynamics study of pair interactions, interfacial microstructure, and nanomorphology of C60/MEH-PPV hybrids," *J. Polym. Res.*, vol. 20, no. 7, 2013.

[25] S. Y. Park, C. H. Lee, W. J. Song, and C. Seoul, "Enhanced electron injection in organic light-emitting devices using Al/LiF electrodes," *Curr. Appl. Phys.*, vol. 1, no. 1, pp. 116–120, 2001.

[26] N. Wang, J. D. Zimmerman, X. Tong, X. Xiao, J. Yu, and S. R. Forrest, “Snow cleaning of substrates increases yield of large-area organic photovoltaics,” *Appl. Phys. Lett.*, vol. 101, no. 13, p. 133901, 2012.

[27] S. Nosé, “A molecular dynamics method for simulations in the canonical ensemble,” *Mol. Phys.*, vol. 52, no. 2, pp. 255–268, 1984.

[28] S. L. Mayo, B. D. Olafson, and W. A. Goddard III, “DREIDING: A Generic Force Field for Molecular Simulations,” *J. Phys. Chem.*, vol. 94, no. Suite 540, pp. 8897–8909, 1990.

Chapter 6

Effect of copolymer in polymer bulk-heterojunction organic photovoltaics

6.1. Introduction

Development of semi-conducting π-conjugated polymers opens a new possibility in the area of organic photovoltaics (OPV) [1–4]. One archetype donor:acceptor (D:A) OPV system is based on poly(3-hexylthiophene) (P3HT) and phenyl-C61-butyric acid methyl ester (PCBM). Since P3HT:PCBM-based OPV was successfully demonstrated in 2002 [5], this archetype system has been intensively investigated to understand the effects of the morphology of bulk heterojunction on the performance of OPVs. Fabrication of the bulk-heterojunction OPVs involves solution processing of the D:A layer followed by appropriate annealing to construct a nanoscale morphology in the D:A layer [6, 7]. This provides a large interfacial area between the donor and acceptor to promote exciton disassociation and charge extraction. However, long-term annealing eventually leads to a large macroscopic phase separation of the donor and the acceptor due to their immiscibility [8–10]. Some approaches using gradient or block copolymers have been reported to localize the phase segregation of the two dissimilar molecules [11, 12]. Palermo *et al*. reported an improved thermal stability of P3HT:PCBM bulk heterojunction OPVs when a gradient copolymer was incorporated as an additive [13]. However, a systematic analysis to correlate the OPV performance with the effect of the presence of a copolymer in terms of the blend morphology of P3HT:PCBM is still lacking.

6.2. Results & Discussion

In this work, we demonstrated that addition of a thiophene-fullerene copolymer to P3HT:PCBM based organic photovoltaics (OPVs) largely affect their performance and thermal stability. The blended 8 wt% copolymer in the active layer of P3HT:PCBM (50:50 wt%) increases the initial power conversion efficiency (*PCE*) of the OPV from 2.6±0.2 % to 3.1±0.2 %. Upon applying continuous thermal annealing to the OPVs, we found strong phase segregation of P3HT and PCBM from optical microscopy and atomic force microscopy (AFM) analysis. The phase segregation results in the decrease of *PCE* of conventional P3HT:PCBM OPVs from 2.6±0.2 % to 1.2±0.2 % after 90 min of the thermal annealing. However, the added copolymer effectively suppressed the phase segregation during the thermal annealing by compatibilizing P3HT-rich and PCBM-rich domains, resulting in a much smaller decrease in *PCE* from 3.1±0.2 % to 2.7±0.2 % after the same 90 min of the thermal annealing. More importantly, we found that the fullerene units within the copolymer promoted charge extraction. Conductive-tip atomic force microscopy (c-AFM) analysis showed that electron current of the P3HT:PCBM OPVs with 8 wt% copolymer was more than two times larger than that of the P3HT:PCBM OPVs without the copolymer. The difference in the charge extraction capability appeared in the series resistance of the OPVs. While the series resistance of the P3HT:PCBM OPVs with 8wt% copolymer stayed below 10 $\Omega\times cm^2$ regardless of the duration of the thermal annealing up to 90 min, that of the OPVs without the copolymer was larger than 15 ($\Omega\times cm^2$) and showed drastic increase to 47 $\Omega\times cm^2$ after 90 min annealing. The variation in the series resistance was accordingly reflected in the fill factor (*FF*) of the OPVs. Furthermore, the copolymer could also facilitate charge recombination because its highest occupied molecular orbital (HOMO) and lowest unoccupied molecular orbital (LUMO) lie between those of P3HT and PCBM, respectively. This resulted in the increase in the reverse

bias saturation current (J_0) of OPVs. We verified that the difference in J_0 would result in the change in V_{OC} based on the ideal diode equation for organic heterojunction [14].

6.2.1. Synthesis of thiophene-fullerene functionalized copolymer

The synthesis of the fullerene functionalized dibenzooctyne (PCB-DIBO, molecule **9** in Figure 6.1) took five steps from commercially available fullerenes (see section 6.4 for more details) by our collaborator, Prof. McNeil group in the chemistry department of the University of Michigan. A metal-free click reaction was adapted to achieve higher fullerene loading since previous copper-catalyzed azide alkyne cycloaddition (CuAAC) based reaction could result in cross-linked polymers with metal residue [13]. Instead of using metal catalysis, the driving force of the cycloaddition was sought from the cyclic alkyne to release the strain. The strain-promoted alkyne azide cycloaddition (SPAAC) of **P2** and PCB-DIBO afforded the target copolymers with complete conversion and a single peak in the gel permeation chromatography (GPC) trace. This indicates that no cross-linking occurred even under ambient atmosphere. SPAAC enables high fullerene loading up to 100 mol % without cross-linking, however, 20 mol % loading of fullerene in copolymer was chosen considering the solubility of the copolymer.

6.2.2. Performance of P3HT:PCBM bulk heterojunction OPVs with copolymer

Figures 6.2a,b show the *J-V* characteristics of the P3HT:PCBM OPVs and the P3HT:PCBM OPVs having 8 wt% copolymer under the simulated AM 1.5G illumination. Both OPVs have an inverted architecture where ZnO and MoO_3 are used as an electron and a hole selective layer, respectively [15]. Under constant thermal annealing at 150 °C, while the *J-V* characteristics of the P3HT:PCBM OPVs degrades significantly after 45 min of annealing (Figures

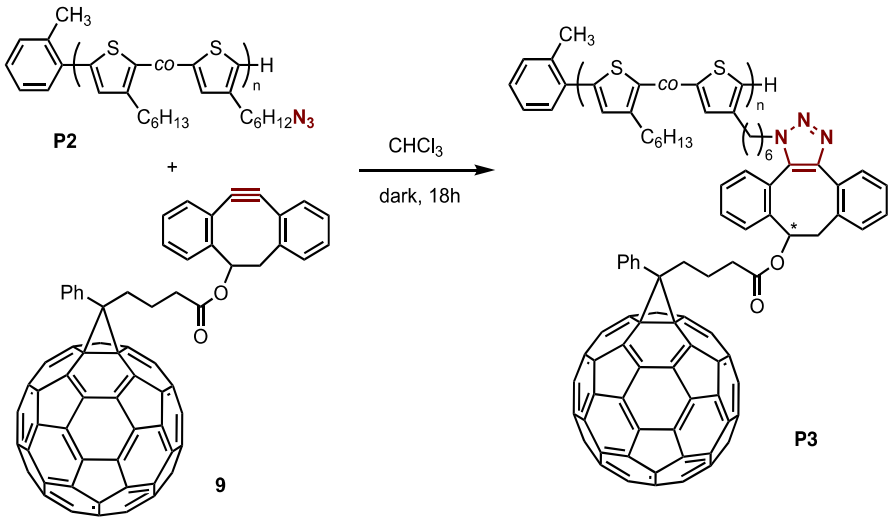

Figure 6.1. Synthetic scheme of thiophene-fullerene functionalized copolymer.

6.2 a and f), the OPVs with 8 wt% copolymer show more stable *J-V* curves over 90 min thermal annealing (Figures 6.2 b, f). Figures 6.2 c-f summarize the figure of merits of the two different OPVs under various thermal annealing times. The short-circuit current (J_{sc}) of the P3HT:PCBM OPVs experiences significant degradation: After 90 min of the thermal annealing, J_{sc} drops to almost half of its pristine device's J_{sc}, whereas J_{sc} of the P3HT:PCBM OPVs with 8 wt% copolymer changes only marginally (Figure 6.2c). The open circuit-voltage (V_{OC}) of the OPVs with the copolymer is slightly lower (from 0.02 to 0.07 *V*) than that of the OPVs without the copolymer as shown in Figure 6.2d. While *FF* of the OPVs containing the copolymer is more than 0.5, *FF* of the P3HT:PCBM OPVs is at least 20% lower (Figure 6.2e). Overall, the initial *PCE* of the P3HT:PCBM OPVs with 8 wt% copolymer is 3.1±0.2 %, larger than 2.6±0.2 % of the P3HT:PCBM OPV. After the thermal annealing, the difference in *PCE* of the two types of OPVs is much larger (>1% absolute) than the initial PCE difference as shown in Figure 6.2f.

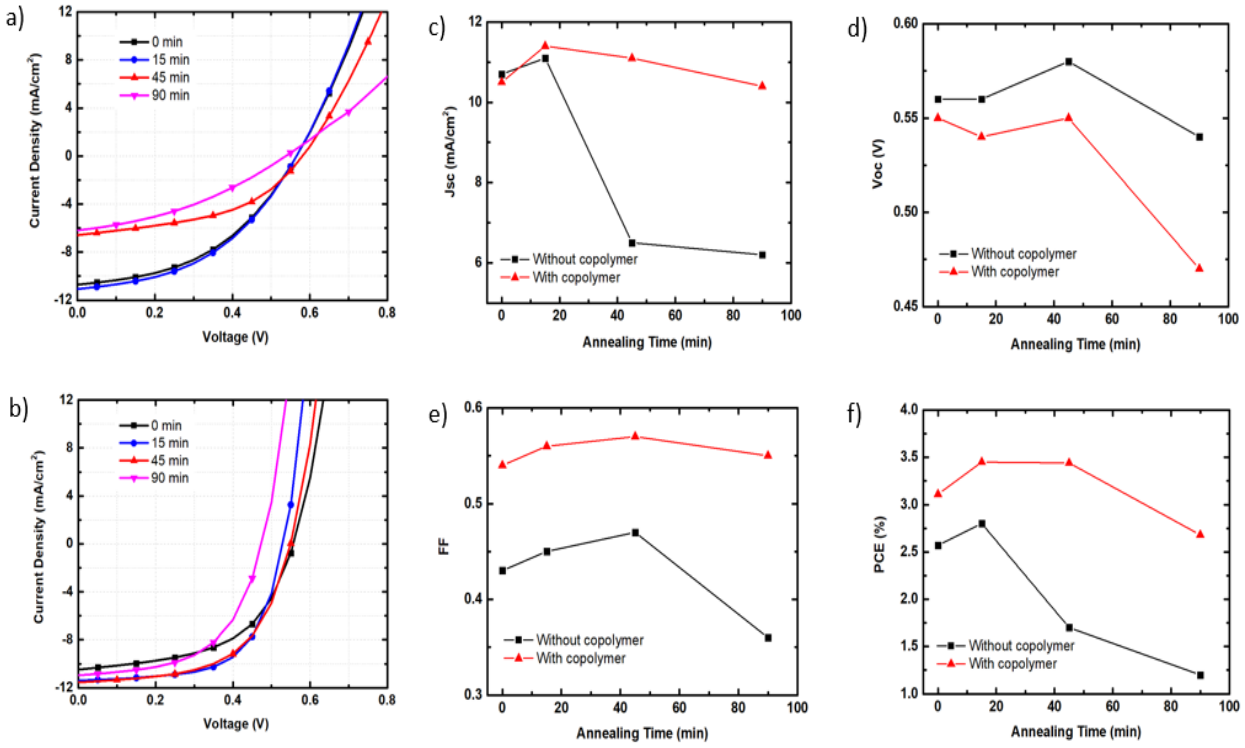

Figure 6.2**.** Current density-voltage (*J-V*) characteristics of (a) P3HT:PCBM bulk-heterojunction OPVs and (b) the OPVs with copolymer under different thermal annealing time (0, 15, 45, 90 min). Performance of the OPVs depending on thermal annealing time is summarized: (c) current density *Jsc*, (d) open-circuit voltage V_{oc}, (e) fill factor *FF*, and (f) power conversion efficiency *PCE*.

6.2.3. Morphology of P3HT:PCBM bulk heterojunction with copolymer

We analyzed the morphology of the P3HT:PCBM blend and the P3HT:PCBM blend with 8 wt% copolymer by AFM and optical microscopy as shown in Figure 6.3. Without any thermal annealing, the P3HT and PCBM domains of the blend film without the copolymer are clearly visible in the AFM phase images (Figure 6.3a). Figure 6.3b implies that P3HT and PCBM become much more miscible with the addition of the copolymer. The optical microscopy image of the P3HT:PCBM blend shows strong phase segregation of the P3HT and PCBM domains after the

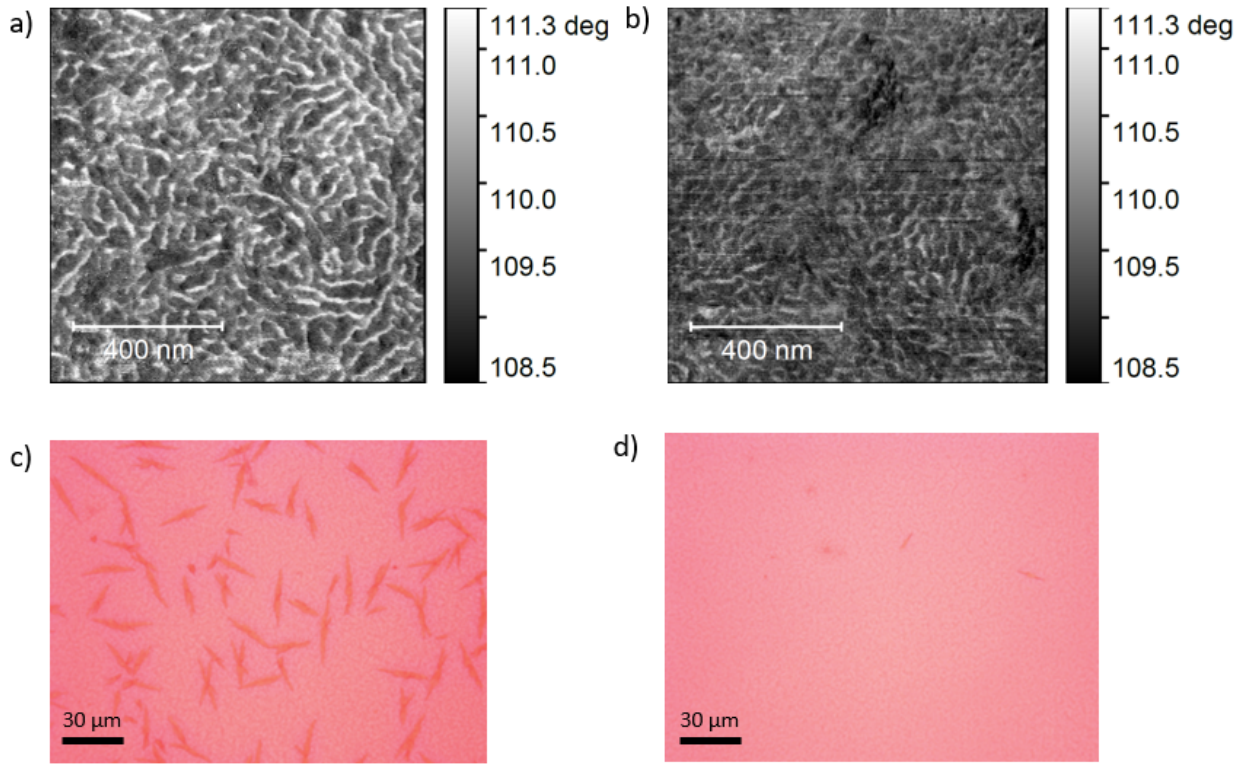

Figure 6.3**.** AFM phase image of (a) 180 nm thick P3HT:PCBM or (b) 180 nm thick P3HT:PCBM with 8 wt% copolymer on ITO/ZnO (40 nm) substrate. Optical microscopy image of (c) 180 nm thick P3HT:PCBM or (d) P3HT:PCBM with 8 wt% copolymer on glass substrate after 90 min of thermal annealing at 150 ^{o}C. Scale bar is included in each figure.

thermal annealing at 150 °C for 90 min (Figure 6.3c). This large scale (µm) phase segregation will reduce the interfacial area between P3HT and PCBM, thereby impairing exciton disassociation and consequential drop in J_{SC} (see Figure 6.2c). However, the phase segregation is effectively suppressed in the P3HT:PCBM blend film having the copolymer (Figure 6.3d). Thus, we can regard the copolymer as a 'morphological compatibilizer' to maintain the nanoscale blend morphology of P3HT and PCBM even after a long-term thermal treatment.

To understand the origin of the *FF* improvement in the P3HT:PCBM OPVs with the copolymer, c- AFM analysis was conducted in two different configurations: by using either MoO_3

or ZnO as the charge transporting layer, we could collect separately the hole current and the electron current (See section 6.4 for the details).

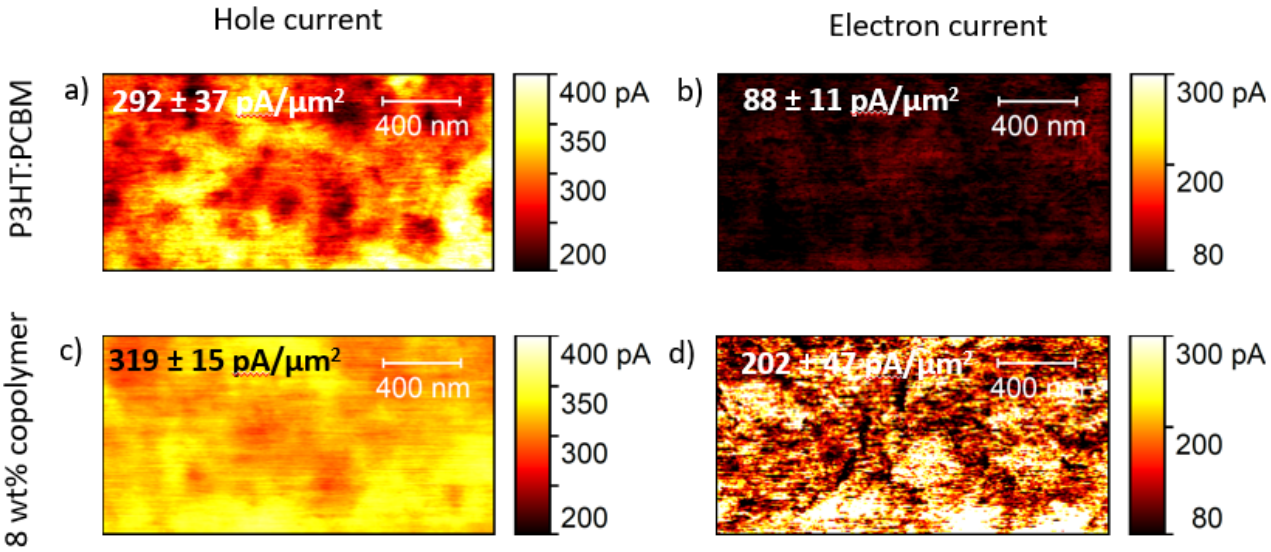

Figure 6.4. Conductive-AFM (c-AFM) image of 180 nm thick P3HT:PCBM on (a) ITO/MoO_3 (20 nm) or (b) ITO/ZnO (40 nm) substrate. C-AFM image of 180 nm thick P3HT:PCBM with 8 wt% copolymer on (c) ITO/MoO_3 (20 nm) or (d) ITO/ZnO (40 nm) substrate. Average current obtained from current distribution over 1×2 μm is included in each image. The conductive AFM images were obtained through collaboration with Jill Wenderott.

Figure 6.4 shows hole and electron current of the P3HT:PCBM and the P3HT:PCBM with 8 wt% copolymer. While the hole current does not show any significant difference (Figure 6.4a and 6.4c), the electron current of the P3HT:PCBM blend with 8 wt% copolymer is more than twice larger (202±47 pA/μm^2) than that of the P3HT:PCBM without the copolymer (88±11pA/μm^2) as shown in Figure 6.4b,d. We attribute the increase in the electron current to the fullerene units dangling along the copolymer backbone (see Figure 6.1). We further investigated the hole and electron current of the P3HT:PCBM thin films having a higher wt% of copolymer (Figure 6.5). We found that the electron current of P3HT:PCBM with 12 wt% copolymer was lower than that of the 8 wt% copolymer thin-film and the hole current was even lower than the pristine P3HT:PCBM films

without the copolymer. The largely reduced hole current could imply that when a large amount of copolymer is blended to the P3HT:PCBM matrix, the copolymer goes into the P3HT-rich domain and disrupts the polymer packing and ruins the original morphology of the P3HT:PCBM blend.

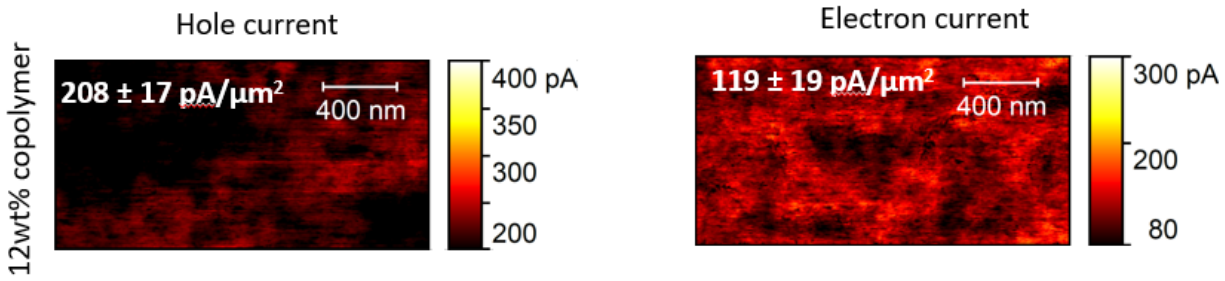

Figure 6.5. **c**-AFM image of 180 nm thick P3HT:PCBM with 12 wt% copolymer on (a) ITO/MoO_3 (20 nm) or (b) ITO/ZnO (40 nm) substrate. Average current obtained from current distribution over 1×2 μm is included in each image. The conductive AFM images were obtained through collaboration with Jill Wenderott.

6.2.4. V_{oc}, FF changes in P3HT:PCBM with copolymer bulk heterojunction OPV

The effect of the copolymer having a high electron conductivity appears in the *J-V* characteristics of OPVs. We extracted the series resistance (R_s) of each OPV from the inverse slope of the *J-V* curve at the V_{OC} point and plotted them in Figure 6.6. R_s of the P3HT:PCBM OPVs are much higher (at least above 15 Ω×cm^2 and increases to 47 Ω×cm^2 after 90 min annealing) than that of the P3HT:PCBM OPVs with 8 wt% copolymer (below 10 Ω×cm^2). The improved *FF* of the OPVs having the copolymer originates from the enhancement in electron conductivity. From the cyclic voltammetry (CV) measurement (Figure 6.7a), the HOMO of the copolymer was determined to be -5.48 eV, which is between the HOMO of P3HT and the HOMO of PCBM [16]. The LUMO of the copolymer, calculated by subtracting the HOMO energy from the optical energy gap (E_g) (Figure 6.7b), is -3.9 eV. Thus, the LUMO of the copolymer is also between the LUMOs of P3HT and PCBM. In this energy level alignment, the copolymer is in favor of the extraction of

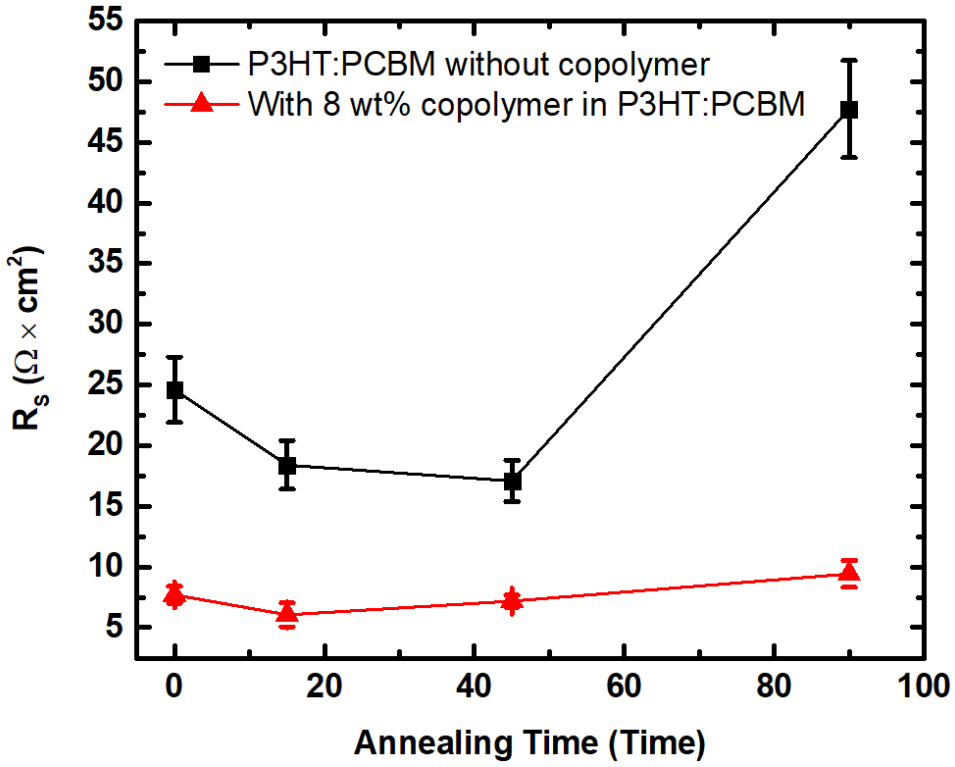

Figure 6.6. Series resistance (R_s) of P3HT:PCBM and P3HT:PCBM with 8 wt% copolymer bulk heterojunction OPVs under different thermal annealing time. Error bar is obtained from standard deviation of three different devices.

electron and hole polarons towards each electrode. However, while the copolymer facilitates the extraction of each charge polaron between P3HT and PCBM, charge recombination can also occur within the copolymer concurrently.

Specifically, V_{OC} of organic heterojunction is given by [14, 17]:

$$qV_{OC} = \Delta E_{HL} - nk_BT \ln[J_0/J_{SC}] \quad (6.1)$$

where, ΔE_{HL} is the energy level difference between HOMO of the donor and LUMO of the acceptor, n is the ideality factor of the diode, k_B is the Boltzmann constant, T is temperature, J_0 is

the reverse bias saturation current density, and J_{SC} is the short-circuit current density. The amount of recombined charge polarons is represented as J_0 in the Equation 6.1 [14, 17]. Figure 6.8 shows the dark *J-V* characteristics of the P3HT:PCBM OPVs and the P3HT:PCBM OPVs with 8 wt% copolymer after 45 and 90 min annealing. J_0 of the P3HT:PCBM OPVs is one order of magnitude lower than that of the P3HT:PCBM OPVs with the copolymer.

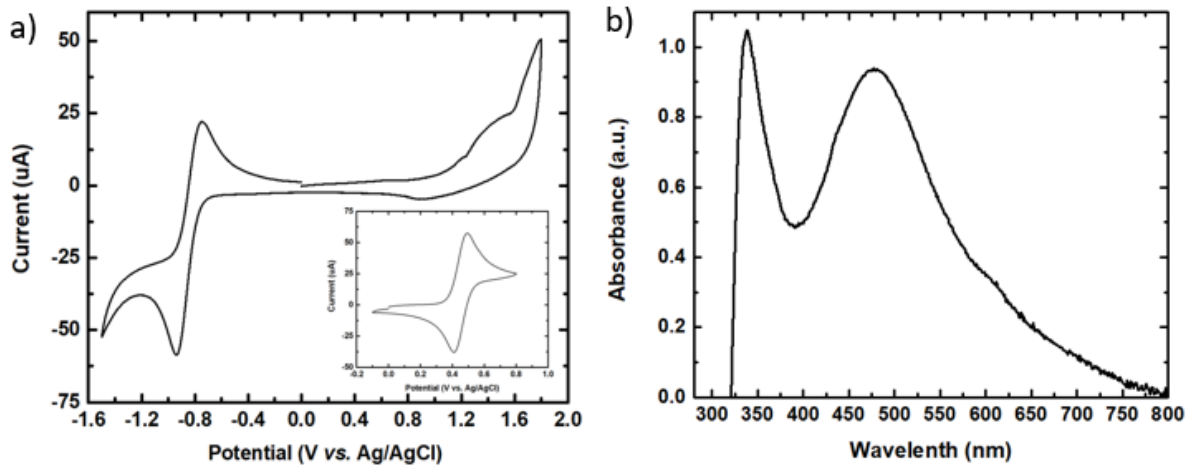

Figure 6.7. (a) Cyclic voltammetry (CV) curve of copolymer in acetonitrile solution. The inset is the CV curve of ferrocene as a standard reference at a scan rate of 50 mV/s. (b) Absorption of copolymer thin-film measured by UV-vis spectrometer.

The corresponding V_{OC} changes from the difference of J_0 is $nk_BT\ln[10J_{SC2}/J_{SC1}] \approx 0.07\ V$ (For simplicity, n ≈ 1.5 for P3HT:PCBM heterojunction [18], $k_BT \approx 25.7$meV, $J_{SC1} \approx 10$ mA/cm^2 for P3HT:PCBM with copolymer OPVs, and $J_{SC2} \approx 6$ mA/cm^2 for the P3HT:PCBM OPVs). This calculated value of 0.07 *V* is consistent with the V_{OC} difference observed from the two types of OPVs (cf. Figure 6.2).

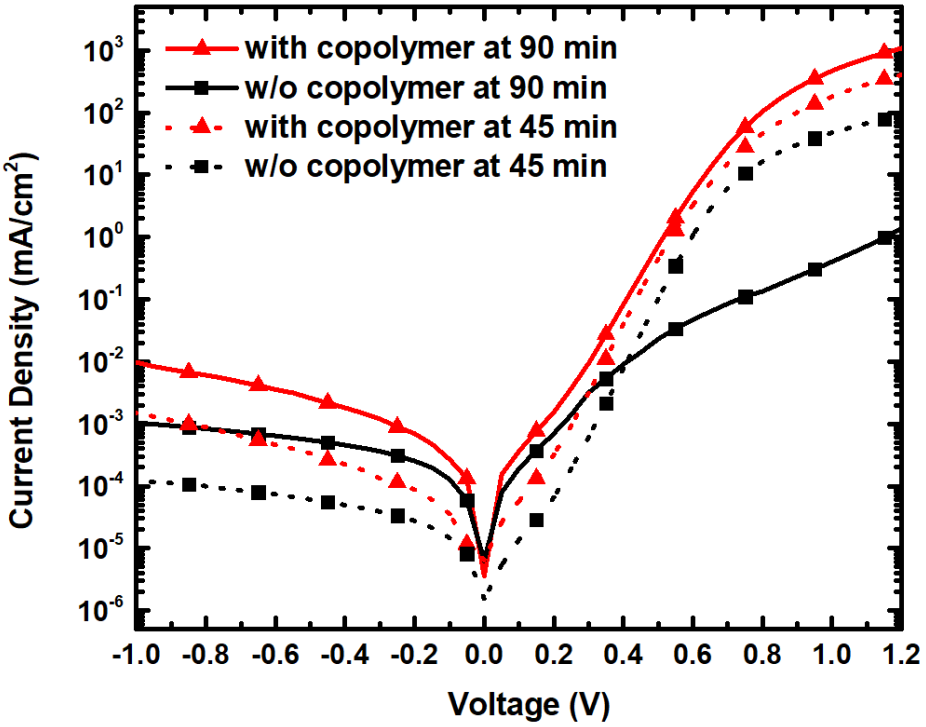

Figure 6.8. Dark *J-V* characteristics of P3HT:PCBM and P3HT:PCBM with 8 wt% copolymer bulk heterojunction OPVs after 45, 90 min of thermal annealing.

6.3. Conclusion

We demonstrated that performance and reliability of P3HT:PCBM bulk heterojunction OPV was improved with an addition of the fullerene functionalized thiophene copolymer. The copolymer effectively compatibilzes P3HT and PCBM, suppressing μm-size phase segregation of P3HT and PCBM under a long-term thermal treatment. Microscopy data show that P3HT and PCBM become more miscible by the copolymer, leading to more stable performance of OPVs. *PCE* of pristine P3HT:PCBM bulk heterojunction OPVs degrades from 2.6±0.2 % to 1.2±0.2 % , whereas *PCE* of the equivalent OPVs with 8 wt% copolymer drops only 0.4 % absolute after 90 min of the thermal annealing. Furthermore, the copolymer facilitates extraction of charge polarons in P3HT:PCBM blend with suitable HOMO and LUMO energy levels. The fullerene unit in the

copolymer helps to extract electron polarons, supported by the increase in the electron current of c-AFM measurement. R_s of OPVs with the copolymer remains below 10 Ω×cm^2 while R_s of the pristine P3HT:PCBM OPVs undergoes drastic increase to 48 Ω×cm^2 after 90 min of thermal annealing. Reverse bias saturation current J_0 of OPVs with the copolymer is one order of magnitude higher than J_0 of P3HT:PCBM OPVs without the copolymer. Although V_{oc} of OPVs with the copolymer is slightly lower due to the higher J_0 compared to the pristine P3HT:PCBM OPVs, overall *PCE* of OPVs with the copolymer is higher resulting from the *FF* enhancement through better charge extraction.

6.4. Experimental details

Synthesis of sub unit in thiophene-fullerene functionalized copolymer (Figure 6.9): All chemical synthesis was conducted by our collaborator, McNeil Group in the chemistry department of the University of Michigan. To prepare copolymers with precise controlled monomer sequences and ratios, a living chain-growth polymerization method known as catalyst transfer polymerization (CTP) was used. The method enables synthesis of polymers with controlled chain length (*M*n), low dispersity (Đ), high regioselectivity, and known end group. To ensure the precision of the claimed polymer sequence, we used a tolyl-functionalized nickel catalyst **3** to cap tol group on one side of the polymer chain for one-direction propagation and two monomers that only differ on the end of the hexyl side chain to minimize the reactivity difference during CTP. Using the efficient polymerization method, we prepared copolymers composed of 3-hexylthiophene (3HT) and 3(1-bromohexylthiophene) (3BHT) in random sequence with 80:20 ratio. Random sequence of copolymer was obtained by adding catalyst **3** to a mixture of monomer **1** and **2**. A feeding composition of 60:40 for monomer **1**:**2** was used for polymerization model. The 20 mol% of

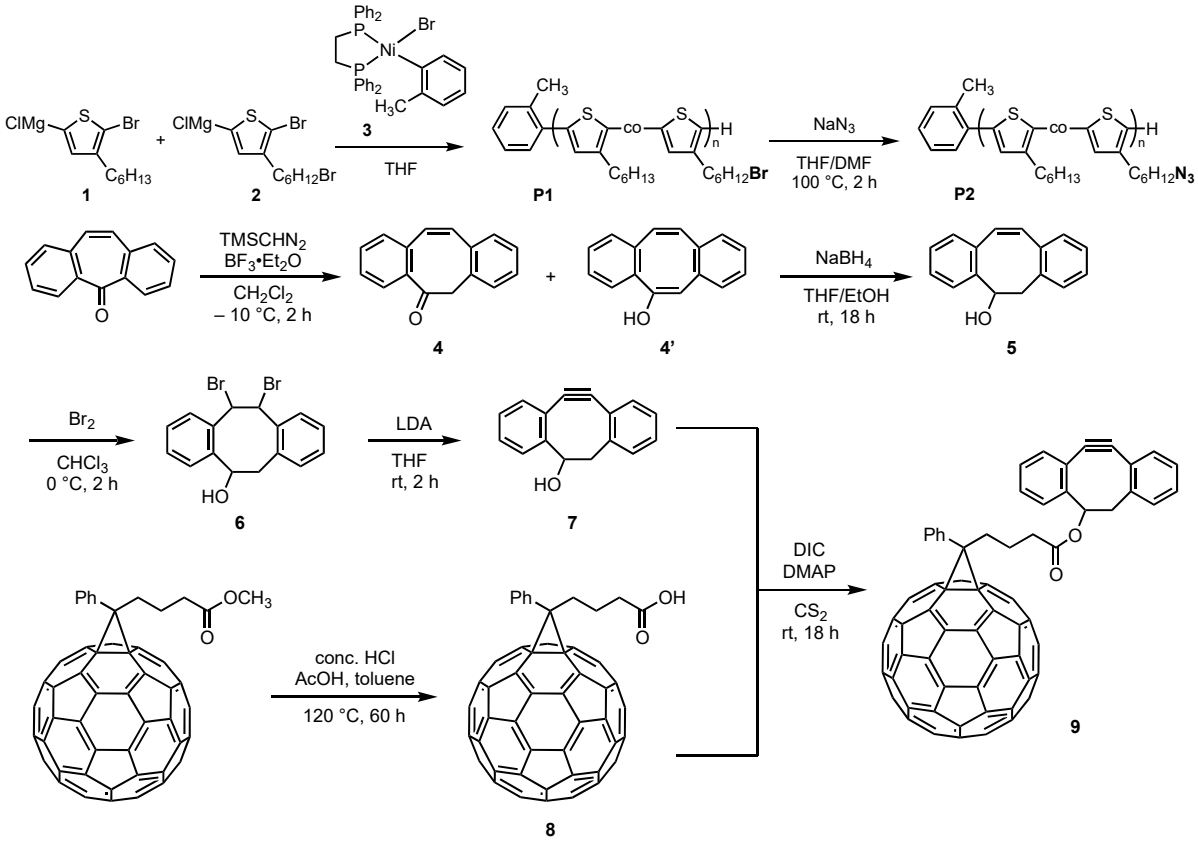

Figure 6.9**.** Synthetic scheme of sub units in thiophene-fullerene functionalized copolymer.

3BrHT was incorporated in random sequence copolymer, and it showed a consistent copolymer composition that matched with the monomer feeding ratio (~ 40% of 3BrHT). Polymer chain length was aimed at 80 repeating units (synthesized by adding 1.25 mol% catalyst with 80/1 monomer/catalyst mole ratio). Obtained 20 mol% random sequence copolymer has a number-average molecular weight M_n of 21.7 kDa, narrow dispersity Đ of 1.22, and high regioregularity. Then post-polymerization functionalization was performed to convert the side chain bromide to azide, which is widely used in click chemistry for convenient combination with another functionalized unit.

Ring expansion of the starting material afforded dibenzocyclooctenone **4** and it's enol form **4'** by carbene insertion in quantitative yield. Both isomers **4** and **4'** can be reduced to

dibenzocyclooctenol **5**. Bromination of the double bond and the following reduction with lithium diisopropyl amide (LDA) afforded dibenzocyclooctynol (DIBO) **7**, which acts as a linker for polymer and fullerene. DIBO **7** was then used to couple with PCBA **8**, which is prepared from hydrolysis of commercial PCBM, affording PCB-DIBO **9** via esterification.

Device fabrication**:** All OPV devices have the following inverted structure: glass/ITO/ZnO(40 nm)/Polymer layer/MoO_3 (20 nm)/Ag(100 nm). The ITO substrate was first-cleaned with detergent, DI water, acetone, and iPrOH for 10 min each, followed by the exposure to 245 nm ultraviolet light source under oxygen flow for 15 min. ZnO sol-gel solution was prepared as described in the literature [19]. The prepared ZnO solution was spin-coated at 3000 rpm for 60 s, followed by thermal annealing in air at 150 °C for 20 min. All polymer solutions were prepared at 30 mg/mL concentration of P3HT, PCBM, and the copolymer in *o*-DCB. The prepared solutions were heated at 60°C for 12 h before the spin-casting in ultra-high purity (<1ppm of H_2O and O_2) N_2 glovebox. Spin-casting of the polymer solution at 800 rpm for 180 s gave 180±15 nm thick film. The thickness of the polymer thin-film was determined by variable-angle spectroscopic ellipsometry. J.A. Woollam M-2000 ellipsometer was used to record near-infrared (1100 nm – 1600 nm) spectroscopic data, followed by Cauchy-model fitting for thickness measurement [20]. After spin-casting the polymer solution, the films were subsequently transferred to an Angstrom AMOD thermal evaporation chamber integrated with the N_2 glovebox system. Molybdenum masks with 1 mm radius circular openings were placed on the sample, determining 3.14 mm^2 of the device size. MoO_3 and Ag were evaporated at a rate of 1 Å/s under the base pressure of 3×10^{-7} torr inside the chamber.

Measurement of the device characteristics: *J-V* characteristics of the devices were recorded by a HP 4156a semiconductor parameter analyzer. The transparent glass/ITO side of the devices

was illuminated with simulated AM 1.5G solar spectrum at 1 sun intensity (100 mW/cm^2). The intensity of the solar simulator was calibrated by the National Renewable Energy Laboratory (NREL)-traceable Si reference cell.

AFM and c-AFM measurement: Jill Wenderott in Peter Green group provided helps for the measurement. Asylum Research MFP-3D atomic force microscope was used for both phase images and conductive-tip atomic force microscopy (c-AFM) images. Phase images of the spin-casted polymer (180 nm) on ITO/ZnO (40nm) were obtained under tapping mode. The c-AFM images were obtained under the contact-mode using a Pt-Ir5-coated tip (spring constant 0.2 N/m). For the hole and electron current measurement, the spin-casted polymer films (180 nm) on ITO/MoO_3 (20 nm) or ITO/ZnO (40 nm) were scanned under 1.5 V of applied bias in reference to an ITO substrate. The average current and standard deviation were obtained from the current distribution over 1×2 μm scanned area.

6.5. References

[1] J. J. M. Halls *et al.*, "Efficient photodiodes from interpenetrating polymer networks," *Nature*, vol. 376, no. 6540. pp. 498–500, 1995.

[2] W. U. Huynh, J. J. Dittmer, and A. P. Alivisatos, "Hybrid Nanorod-Polymer Solar Cells," vol. 295, no. March, pp. 2425–2428, 2002.

[3] W. J. E. Beek, M. M. Wienk, and R. A. J. Janssen, "Efficient hybrid solar cells from zinc oxide nanoparticles and a conjugated polymer," *Adv. Mater.*, vol. 16, no. 12, pp. 1009–1013, 2004.

[4] C. R. McNeill and N. C. Greenham, "Conjugated-polymer blends for optoelectronics," *Adv. Mater.*, vol. 21, no. 38–39, pp. 3840–3850, 2009.

[5] P. Schilinsky, C. Waldauf, and C. J. Brabec, "Recombination and loss analysis in polythiophene based bulk heterojunction photodetectors," *Appl. Phys. Lett.*, vol. 81, no. 20, pp. 3885–3887, 2002.

[6] M. Campoy-Quiles *et al.*, "Morphology evolution via self-organization and lateral and vertical diffusion in polymer:fullerene solar cell blends," *Nat. Mater.*, vol. 7, no. 2, pp. 158–164, 2008.

[7] M. Seminar, R. Havemeyer, and A. J. Heeger, " Plastic Solar Cells ': Self-Assembly of Bulk Heterojunction Solar Cells by Spontaneous Phase Separation ", *Accounts of Chemical Research*, vol. 42, no. 2000, p. 2012, 2012.

[8] Y. Tao, A. H. Lebovitz, and J. M. Torkelson, "Compatibilizing effects of block copolymer mixed with immiscible polymer blends by solid-state shear pulverization: Stabilizing the dispersed phase to static coarsening," *Polymer (Guildf).*, vol. 46, no. 13, pp. 4753–4761, 2005.

[9] Y. Tao, J. Kim, and J. M. Torkelson, "Achievement of quasi-nanostructured polymer blends by solid-state shear pulverization and compatibilization by gradient copolymer addition," *Polymer (Guildf).*, vol. 47, no. 19, pp. 6773–6781, 2006.

[10] J. Kim, R. W. Sandoval, C. M. Dettmer, S. B. T. Nguyen, and J. M. Torkelson, "Compatibilized polymer blends with nanoscale or sub-micron dispersed phases achieved by hydrogen-bonding effects: Block copolymer vs blocky gradient copolymer addition," *Polymer (Guildf).*, vol. 49, no. 11, pp. 2686–2697, 2008.

[11] S. H. Anastasiadis, "Interfacial tension in binary polymer blends and the effects of

copolymers as emulsifying agents," in *Polymer Thermodynamics*, Springer, 2010, pp. 179–269.

[12] M. Chen *et al.*, "Side-chain substitution of poly(3-hexylthiophene) (P3HT) by PCBM via postpolymerization: an intramolecular hybrid of donor and acceptor," *Polym. Chem.*, vol. 4, no. 3, pp. 550–557, 2013.

[13] E. F. Palermo, S. B. Darling, and A. J. McNeil, "π-Conjugated gradient copolymers suppress phase separation and improve stability in bulk heterojunction solar cells," *J. Mater. Chem. C*, vol. 2, no. 17, p. 3401, 2014.

[14] N. C. Giebink, G. P. Wiederrecht, M. R. Wasielewski, and S. R. Forrest, "Ideal diode equation for organic heterojunctions. I. Derivation and application," *Phys. Rev. B*, vol. 82, no. 15, p. 155305, Oct. 2010.

[15] A. K. K. Kyaw, X. W. Sun, C. Y. Jiang, G. Q. Lo, D. W. Zhao, and D. L. Kwong, "An inverted organic solar cell employing a sol-gel derived ZnO electron selective layer and thermal evaporated MoO3 hole selective layer," *Appl. Phys. Lett.*, vol. 93, no. 22, pp. 2006–2009, 2008.

[16] M. D. Irwin, D. B. Buchholz, A. W. Hains, R. P. H. Chang, and T. J. Marks, "p-Type semiconducting nickel oxide as an efficiency-enhancing anode interfacial layer in polymer bulk-heterojunction solar cells," *Proc. Natl. Acad. Sci.*, vol. 105, no. 8, pp. 2783–2787, 2008.

[17] J. D. Zimmerman *et al.*, "Independent Control of Bulk and Interfacial Morphologies of Small Molecular Weight Organic Heterojunction Solar Cells," *Nano Lett.*, vol. 12, no. 8, p. 4366, Aug. 2012.

[18] E. Voroshazi, B. Verreet, T. Aernouts, and P. Heremans, "Long-term operational lifetime and degradation analysis of P3HT:PCBM photovoltaic cells," *Sol. Energy Mater. Sol. Cells*, vol. 95, no. 5, pp. 1303–1307, 2011.

[19] M. S. White, D. C. Olson, S. E. Shaheen, N. Kopidakis, and D. S. Ginley, "Inverted bulk-heterojunction organic photovoltaic device using a solution-derived ZnO underlayer," *Appl. Phys. Lett.*, vol. 89, no. 14, 2006.

[20] F. G. Celii, T. B. Harton, and O. F. Phillips, "Characterization of organic thin films for OLEDs using spectroscopic ellipsometry," *J. Electron. Mater.*, vol. 26, no. 4, pp. 366–371, 1997.

Chapter 7

Organic light-emitting diode (OLED) from metal-free organic phosphor

7.1. Introduction

Organic light-emitting diode (OLED), as an emerging high-end display, has been rapidly replacing liquid crystal displays (LCD) [1]. A significant improvement in the efficiency of OLED was achieved by the development and incorporation of phosphorescent organometallic compounds, which enables efficient intersystem-crossing (ISC) between singlet and triplet excitons [2, 3]. The strong spin-orbit coupling promoted by the heavy-metal atom at the center of the organometallic phosphors allows otherwise forbidden radiative ISC from the excited state of triplets to the ground state [4]. However, the organometallic phosphors particularly blue compounds are known to suffer from the metal-ligand bond-breakage during the OLED operation and the high cost of rare-earth metals. Room-temperature phosphorescence (RTP) from purely organic materials has gained much attention since they are composed of more stable covalent bonds and have a large molecular design window for property tuning [5]. Due to the absence of the heavy metal in the molecular structure, various molecular design strategies to achieve efficient phosphorescence must be implemented: efficient spin-orbit coupling [6–8], the heavy-atom effect by halogen bonding in molecular crystals [7, 9], and effective suppression of molecular vibration [8, 10]. Even though many such novel purely organic phosphors have been reported in the

literature, a systematic investigation and demonstration of OLED devices using purely organic phosphors have not yet been presented due to the lack of insightful understanding on material properties, device physics, and the device fabrication process.

7.2. Results & Discussion

We successfully built phosphorescent OLED employing a metal-free purely organic phosphor. 1-(7-bromo-9,9-diphenyl-9H-fluoren-2-yl)-2,2,2-trifluoroethan-1-one (BrPFL-TFK) shows significant phosphorescent photoluminescence owing to its triplet-producing aromatic aldehyde and the heavy-atom effect from its bromine. Bearing in mind the relatively-long triplet lifetime (~ms) of metal-free organic phosphors, a more careful consideration should be given to the OLED structure. Electroluminescent property of BrPFL-TFK together with different host materials was investigated first. BrPFL-TFK in *N,N'*-dicarbazolyl-4,4'-biphenyl (CBP) host undergoes exothermic energy transfer from BrPFL-TFK to CBP, showing spectral broadening in its phosphorescence emission as well as undesired fluorescence emission from CBP in OLED devices. *N,N'*-dicarbazolyl-3,5-benzene (mCP) host having a higher triplet energy (2.9 eV) prevents the exothermic energy transfer. However, the exciplex emission from mCP and BrPFL-TFK was observed in the electroluminescent spectra due to the rather shallow highest occupied molecular orbital (HOMO) level of mCP. When a new host of 2,8-bis(diphenylphosphoryl)dibenzo[b,d]thiophene (PPT) was used, only bright green phosphorescence emission (1430 cd/m^2 at 100 mA/cm^2) was achieved from BrPFL-TFK:PPT electroluminescence devices. The maximum external quantum efficiency (EQE) of the OLEDs with the PPT host is 2.5% at 1 mA/cm^2 compared to 0.4 %, 1.6% at 1 mA/cm^2 of the OLEDs with the CBP and mCP hosts, respectively. The single-carrier device under different doping

concentrations of BrPFL-TFK shows that PPT and BrPFL-TFK are responsible for electron and hole transport, respectively.

7.2.1. Synthesis and photo-physical property of BrPFL-TFK

Figure 7.1a shows the synthetic scheme of BrPFL-TFK. 2,7-Dibromo-9,9-diphenylfluorene was designed and synthesized first through collaboration with Jaehun Jung since spiro-annulated monomers have good thermal stability due to their steric hindrance [11]. A carbonyl group was

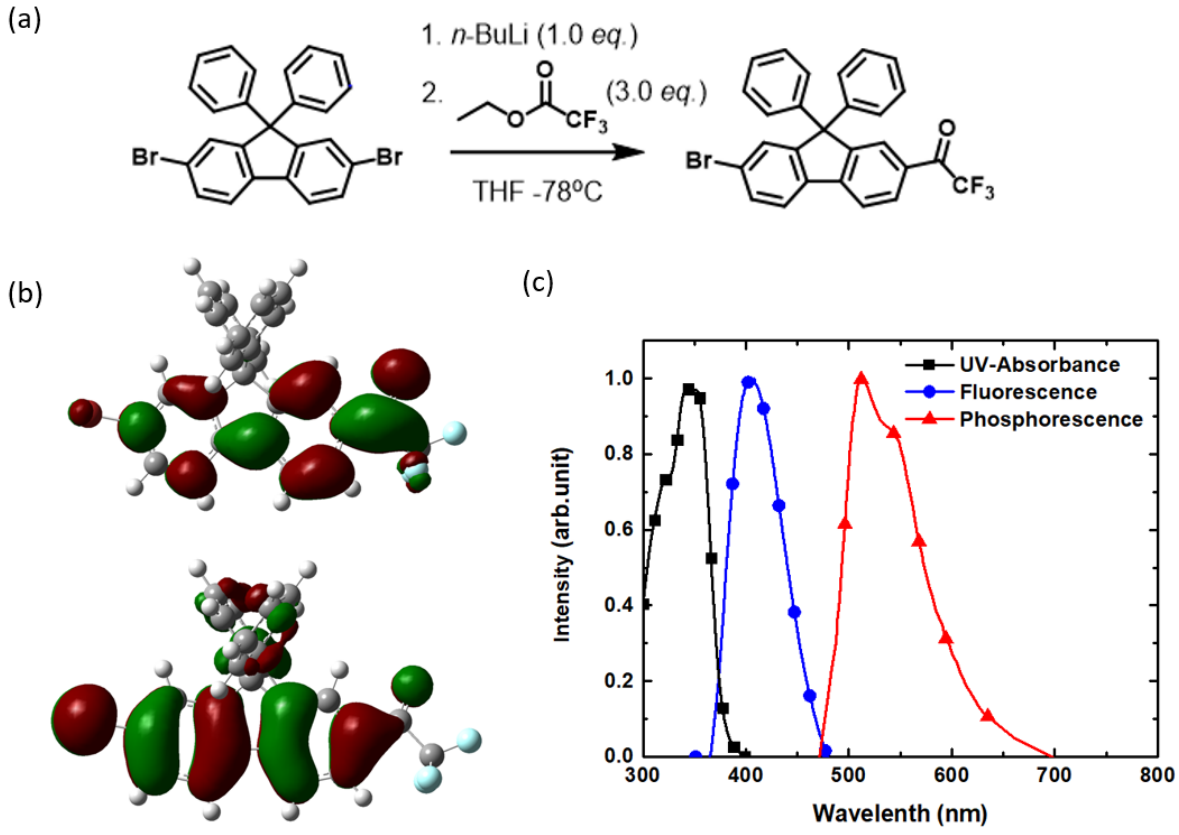

Figure 7.1. (a) Synthetic scheme of 1-(7-bromo-9,9-diphenyl-9H-fluoren-2-yl)-2,2,2-trifluoroethan-1-one (BrPFL-TFK). (b) (top) Lowest unoccupied molecular orbital (LUMO) distribution of BrPFL-TFK and (bottom) highest occupied molecular orbital (HOMO) distribution of BrPFL-TFK. B3LYP and 6-31G* basis set of Gaussian09 program are used. (c) UV-vis absorption (thin-film), fluorescence (thin-film), and phosphorescence (embedded in PMMA) spectra of BrPFL-TFK.

introduced considering that aromatic carbonyl molecules satisfy the El-Sayed rule and promote triplet electron formation [7]. The carbonyl and fluorine group allow the modulation of HOMO and lowest unoccupied molecular orbital (LUMO) energy levels.

Density functional theory (DFT) calculation results of BrPFL-TFK are shown in Figure 7.1b. The calculated HOMO energy level of BrPFL-TFK is -6.54 eV that is comparable to -6.34 eV obtained from a cyclic voltammetry measurement (Figure 7.2). The origin of this very deep HOMO is the electron-withdrawing carbonyl. It is also noted in Figure 7.1b that both HOMO and LUMO distribution include bromine and oxygen atoms, inducing large spin-orbit coupling as well as intramolecular halogen effects.

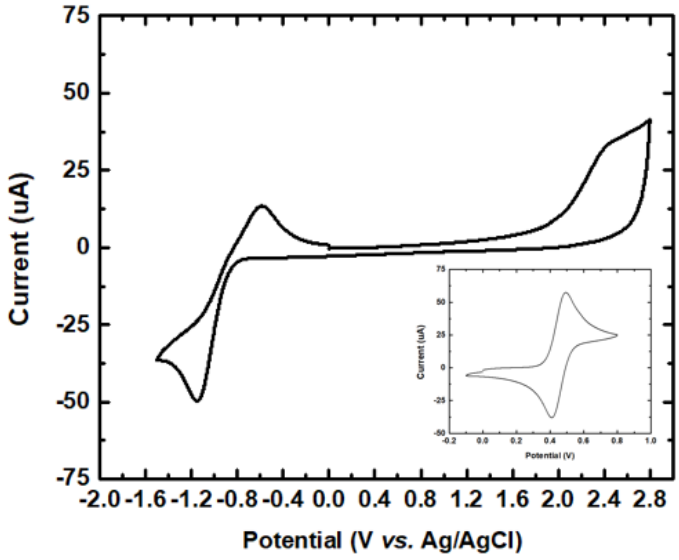

Figure 7.2**.** Cyclic voltammetry (CV) curve of BrPFL-TFK molecules in acetonitrile solution. The inset is the CV curve of ferrocene as a standard reference at a scan rate of 50 mV/s.

The absorption and emission properties of BrPFL-TFK are summarized in Figure 7.1c. The LUMO energy level of -3.25 eV is calculated from the difference between the HOMO energy level (-6.34 eV) and the optical band gap (3.09 eV). Photoluminescence (PL) measurement of a 50 nm

thick vacuum-deposited BrPFL-TFK film shows a fluorescence emission peak at 405 nm whose corresponding singlet energy (S_1) is 3.06 eV. Phosphorescence emission is observed from the PL measurement of poly(methyl 2-methylpropenoate) (PMMA) film having BrPFL-TFK under N_2 environment. From the onset of the phosphorescence spectrum, the triplet energy (T_1) of BrPFL-TFK is calculated to be 2.58 eV that is consistent with 2.56 eV from the DFT calculation. The phosphorescence photoluminescence quantum yield (PLQY) of BrPFK-TFK is Φ_{PL} = 23±1 %.

7.2.2. Spectrum of BrPFL-TFK doped in various host materials

An energy level diagram of the materials used in this study is shown in Figure 7.3. We doped MoO_3 in the hole-transporting layer of CBP or mCP to increase the hole conductivity [12] for all devices. CBP, mCP, PPT are used as a host material in the emissive layer. For the electron-transporting layer, 1,3,5-Tri(1-phenyl-1*H*-benzo[d]imidazol-2-yl)phenyl (TPBi), 3,5,3´,5´-tetra(m-pyrid-3-yl)phenyl[1,1´]biphenyl (BP4mPy) or PPT is used. PL measurements of 2% BrPFL-TFK doped in various host materials are shown in Figure 7.4a. Triplet lifetime of BrPFL-TFK in the three hosts is the same as 0.6 ± 0.1 ms from the mono-exponential fit in the transient PL measurement (Figure 7.4a. inset). BrPFL-TFK doped in CBP host, however, exhibits a broad emission starting from 460 nm compared to the emission of BrPFL-TFK doped in mCP or PPT host. This originates from the low triplet energy (2.56 eV) of CBP. Exothermic energy transfer from BrPFL-TFK triplet to CBP triplet occurs after BrPFL-TFK triplet is populated, resulting in phosphorescence of CBP starting from 460nm. A similar back-energy transfer process is also reported in an organometallic guest-host system [13, 14]. PL of BrPFL-TFK doped in mCP or PPT host, however, shows only phosphorescent emission from BrPFL-TFK, implying that the

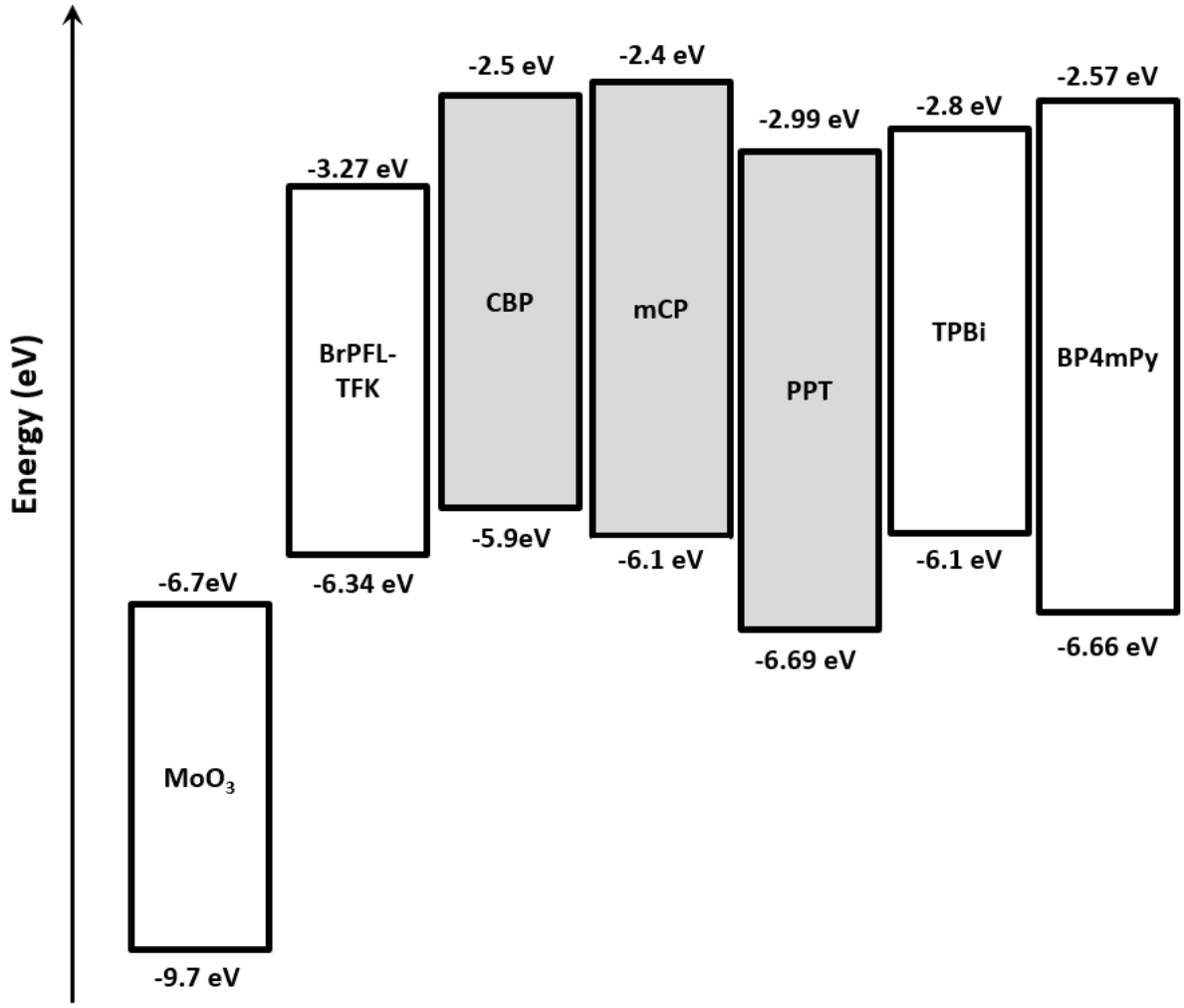

Figure 7.3**.** Energy level diagram of materials used in organic light emitting-diode (OLED) devices. HOMO and LUMO levels of each material are indicated. Shaded layers indicate host materials for emissive layers of the devices.

singlets of hosts are transferred to the singlets of BrPFL-TFK through Förster energy transfer process and subsequently phosphorescence emission is produced through intersystem crossing. Electroluminescent (EL) spectrum of 2% BrPFL-TFK doped CBP device (D1) is shown in Figure 7.4b. Florescent emission of CBP around 400 nm becomes stronger as the current density increases, resulting from inefficient energy transfer from CBP to BrPFL-TFK. The spectral overlap between the fluorescence of CBP and the absorption of BrPFL-TFK is small, making inefficient

Förster energy transfer similar to the CBP-Eupopium organometallic host-guest system [15]. The emission from BrPFL-TFK (λ_{max} = 510 nm) in CBP host is also relatively broad compared to that in mCP host (Figure 7.4c) and PPT host (Figure 7.4d), supporting the possible back-energy transfer process discussed earlier. More efficient energy transfer from host to guest is attained by replacing CBP with mCP having a higher triplet energy (2.9 eV) and a larger spectral overlap ($\lambda_{em.max}$ = 355 nm) [16] with the absorption of BrPFL-TFK. Figure 7.4c shows EL spectrum of the 2% BrPFL-

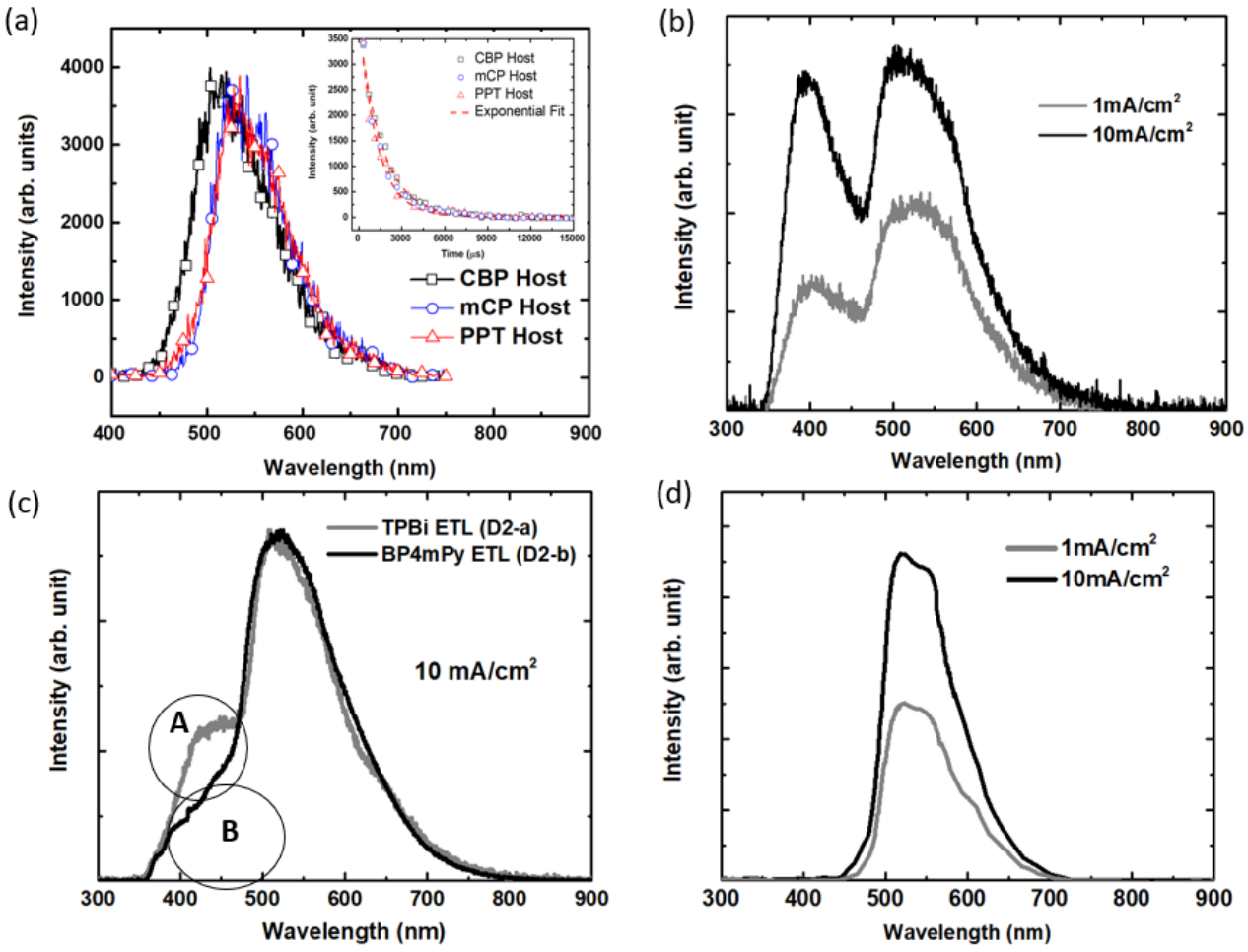

Figure 7.4. (a) Photoluminescence (PL) spectra of a 50 nm thick CBP, mCP, and PPT film having 2% BrPFL-TFK. (inset) Corresponding transient PL decay curve of the three thin-films. Dashed line indicates the mono-exponential fit of the PL decay. Electroluminescent spectra of OLED devices with 2% BrPFL-TFK doped in (b) CBP and (c) mCP with a TPBi or BP4mPy electron-transporting layer, and (d) PPT. Circled A and B areas in (c) indicate undesired residual emission from TPBi fluorescence and exciplex between mCP and BrPFL-TFK, outside of main phosphorescent emission (λ_{max} = 510 nm). The applied current densities are included.

TFK doped mCP host with TPBi (D2-a) or BP4mPy as the electron-transporting layer (D2-b). Both D2 devices show a sharp phosphorescence emission at λ_{max} = 510 nm from BrPFL-TFK and the undesired emission at 400 nm is largely suppressed. We believe that the emission at 400 nm circled in A is TPBi fluorescence due to its shallow HOMO energy level. It is expected that holes at the HOMO level of mCP are transferred to the HOMO of electron-transporting TPBi, generating singlets in TPBi. This TPBi fluorescence emission is eliminated by replacing TPBi with BP4mPy having a deeper HOMO energy level. However, there is still an undesired emission centered at 450 nm (circled B in Figure 7.4c). We attribute this residual emission to the exciplex formation between mCP host and BrPFL-TFK guest during the electroluminescent process in the emissive layer. Since the HOMO and LUMO level of mCP are shallower than those of BrPFL-TFK (cf. Figure 7.3), holes at the HOMO of mCP and electrons at the LUMO of BrPFL-TFK can form exciplex. This is further supported by comparing the theoretical exciplex energy (2.83 eV) with

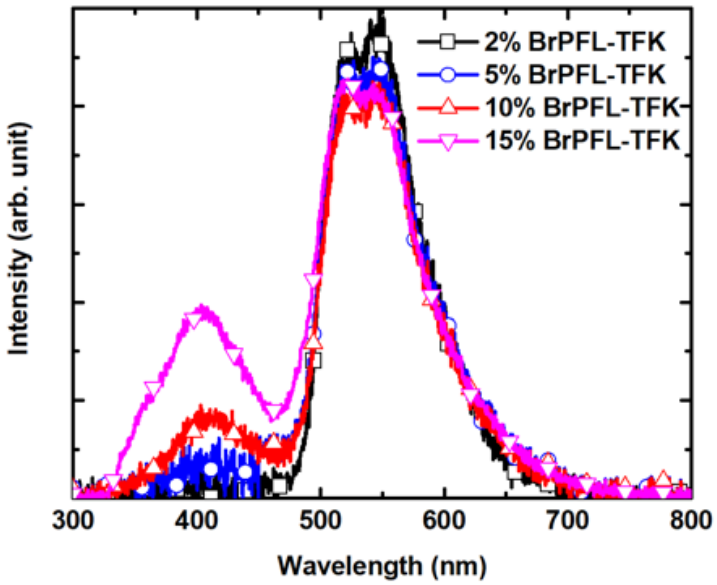

Figure 7.5. Electroluminescent spectra of OLED devices with BrPFL-TFK doped in PPT host emissive layer under different doping concentration of BrPFL-TFK.

the photon energy (2.76 eV) in the EL spectrum. Finally, mCP is replaced by PPT host where there is no possibility of exciplex formation based on the deeper HOMO energy level of PPT. Additionally, PPT has a high triplet energy (2.96 eV), which can prevent back energy transfer, and a large spectral overlap with the absorption of BrPFL-TFK for efficient Förster energy transfer [17]. PPT was also used as the electron-transporting layer (ETL) for D3 since the HOMO level of PPT is deeper than that of BP4mPy. The resulting EL spectrum of the device with PPT as the host molecule and for ETL nearly replicate phosphorescence of BrPFL-TFK regardless of the current density. It is noteworthy that increase in the doping concentration induces fluorescence of BrPFL-TFK (cf. Figure 7.1c) in D3 as shown in Figure 7.5. It is expected that the long triplet lifetime (~ms) of BrPFL-TFK makes accumulated triplet population when the concentration of BrPFL-TFK is high, which retards the intersystem crossing from singlet to triplet, producing fluorescence emission from BrPFL-TFK.

7.2.3. Performance of OLED with the purely organic emitter BrPFL-TFK

Current density-voltage-luminescence (*J-V-L*) characteristics and external quantum efficiency (EQE) of the devices are summarized in Figure 7.6. The devices of BrPFL-TFK doped in PPT host (D3) show the highest brightness of 58 cd/m^2 and EQE of 2.5 % at 1 mA/cm^2. The turn-on voltage of D3 is much lower (~2 V) than the devices made of CBP host (D1) or mCP host (D2) due to the deeper LUMO level of PPT ETL compared to the level of BP4mPy and TPBi. Therefore, electron injection from cathode to PPT ETL would be much more efficient owing to the smaller electron injection barrier. Figure 7.6b shows significant EQE drops when the current density is larger than 10 mA/cm^2 for all devices. Even though we minimized triplet-triplet annihilation (TTA) by keeping a low doping concentration (2%) of BrPFL-TFK, TTA is

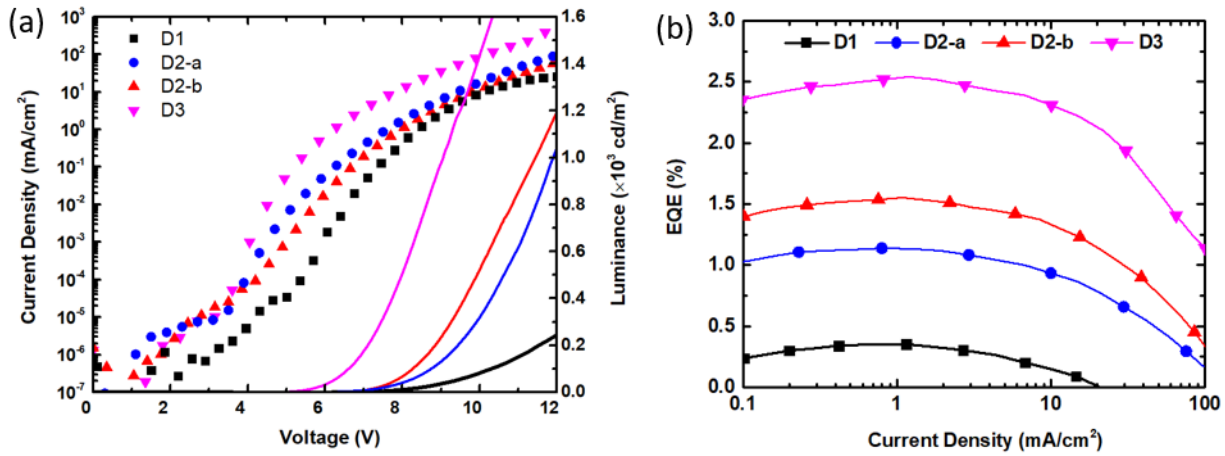

Figure 7.6. (a) Current density-voltage-luminance (*J-V-L*) characteristics of OLED devices having 2% BrPFL-TFK doped in CBP (D1) and mCP with TPBi (D2-a) or BP4mPy (D2-b) as the electron-transporting layer, and PPT (D3). (b) External quantum efficiency-current density (*EQE-J*) plot of the four devices.

unavoidable as the triplet lifetime of BrPFL-TFK is in the range of millisecond. From *J-V* characteristics of the hole-only device of D3 with different BrPFL-TFK concentrations, we find that holes in EML are mainly transported via BrPFL-TFK guest (Figure 7.7a). Figure 7.7b indicates that electron transport is unrelated to the concentration of BrPFL-TFK. As PPT has an

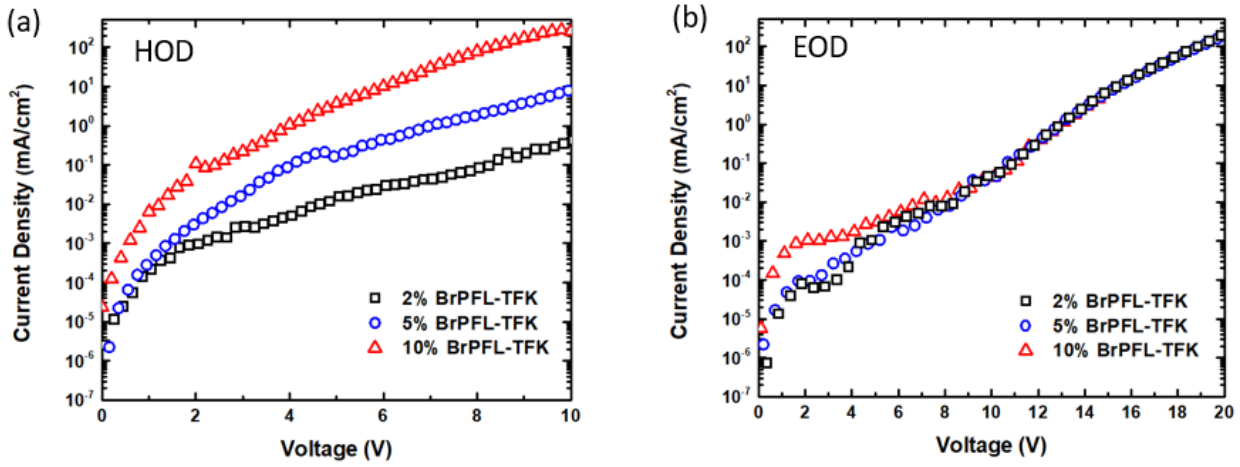

Figure 7.7. (a) *J-V* characteristic of hole-only device for D3 based on the following structure: ITO (UV-Ozone-treated)/15% of MoO_3 doped in mCP (20 nm)/BrPFL-TFK (5 nm)/x% of BrPFL-TFK doped in PPT (20 nm)/PPT (40 nm)/MoO_3 (10 nm)/Al (100 nm). (b) *J-V* characteristic of electron-only device for D3 based on the following structure: ITO (untreated)/BrPFL-TFK (5 nm)/x% of BrPFL-TFK doped in PPT (20 nm)/PPT (40 nm)/LiF (1 nm)/Al (100 nm).

electron deficient diphenylphosphine oxide structure and thereby is known to have a good electron-transporting property [17], majority of electrons are transported and subsequently trapped by BrPFL-TFK with a deeper LUMO energy level.

7.3. Conclusion

We successfully demonstrated phosphorescent OLEDs employing a metal-free purely organic phosphor, BrTFL-TFK. The carbonyl group of BrTFL-TFK satisfying an El-Sayed rule and the heavy atom effect from bromine synergistically allows efficient intersystem crossing, producing bright phosphorescence emission. BrPFL-TFK doped in CBP host suffers from the back-energy transfer, resulting in spectral broadening in PL spectrum as well as undesired fluorescence emission from CBP in the EL spectrum. Replacing CBP with mCP host eliminates the emission from the host due to the higher triplet energy of mCP. However, the singlet emission from TPBi ETL remains due to its shallow HOMO energy level. The ETL emission was removed by using BP4mPy as ETL due to its deeper HOMO energy level while an exciplex emission between BrPFL-TFK and mCP still exists. Finally, pure phosphorescent emission from BrPFL-TFK in EL was realized when PPT was used as the host because PPT has a high triplet energy, a large spectral overlap with the guest, and suitable HOMO-LUMO energy levels. The maximum EQE of 2.5 % was achieved from OLEDs having BrPFL-TFL doped in PPT host at 1 mA/cm^2. However, significant EQE roll-off behavior was observed at the current density higher than 10 mA/cm^2. The long triplet lifetime (~ms) of BrPFL-TFK is the primary reason of the EQE roll-off. We also conclude that holes are transported by BrPFL-TFK and electrons are transported by PPT judging from the *J-V* characteristics of single-carrier devices.

7.4. Experimental details

Synthesis of BrPFL-TFK**:** The chemical synthesis was conducted by Jaehun Jung in Kim group. 2,7-Dibromo-9,9-diphenyl-9*H*-fluorene was synthesized as the starting material described in the literature [11]. The synthesized 2,7-Dibromo-9,9-diphenyl-9*H*-fluorene (1g) was placed into a flame-dried reaction flask under argon purging. Anhydrous tetrahydrofuran was added (20 ml) and the reaction flask was cooled to -78 ^{0}C. n-BuLi (2.5 M) was added dropwise and the reaction flask was stirred for 1 hr, followed by the addition of ethyl perfluororacetate. After 1 hr of stirring, the resulting mixture was let warm up to room temperature. The reaction was quenched carefully with NH_4Cl and extracted with ethyl acetate. The extracted organic layer was dried over $MgSO_4$ with cycles of filtering and evaporation under vacuum at ~10^{-2} torr. Purification was done by silica column chromatography with dichloromethane and hexane. ^{1}H NMR (300 MHz, DMSO-d_6): δ 7.99-7.91 (m, 2H); 7.66-7.61 (m, 5H); 7.29-7.23 (m, 6H); 7.10-7.07 (m, 4H). 1H-NMR spectrum was recorded by a Varian, MR 400 (400 MHz) in dimethyl sulfoxide-*d6* (DMSO-*d6*) solution. Chemical shift values were recorded as parts per million relative to tetramethylsilane as an internal standard, and coupling constants in Hertz.

DFT calculations**:** Single molecule calculations were performed at the density functional theory (DFT) level via the Gaussian09 software [18]. Herein, the ground state geometry in the gas phase and the HOMO and LUMO distributions were fully optimized using the B3LYP function and 6-31G* basis set.

Cyclic voltammetry (CV) measurement: The electrochemical measurements were performed on CH instruments electrochemical analyzer. Glassy carbon electrode, Pt wire, and Ag/AgCl electrode were used as working, counter, and reference electrodes, respectively. A

ferrocene/ferrocenium (Fc/Fc+) redox couple was used as the internal standard which is assumed to have an absolute energy level of -4.8 eV [19].

Photo-physical property of BrPFL-TFK: UV-vis absorption of a 50 nm thick BrPFL-TFK thin film on a quartz substrate was recorded with a Varian Cary 50 Bio spectrometer. Photoluminescence (PL) emission spectra were obtained with a Photon Technologies International (PTI) Quantamaster system. The excitation wavelength was adjusted to the maximum absorption of the host material used, which was between 280 and 350 nm. Phosphorescent lifetime data were collected with a PTI LaserStrobe. The quantum yields of BrPFL-TFK in PMMA were obtained using an integrating sphere. A neutral density filter was inserted near the photomultiplier tube detector to prevent the saturation of the detector with the excitation light source while maximizing the emission signal intensity.

Device Fabrication: The glass/ITO substrate were cleaned with detergent, DI water, aceton, isopropanol for >5 min, respectively. Substrates were subsequently treated with ultraviolet (UV)-ozone for 15 minutes to remove surface-contaminant and lower the work-function of ITO. Substrates were loaded into an ultra-high purity (<1 ppm of O_2, H_2O) glovebox system integrated with a vacuum thermal evaporation chamber. All layers were grown inside the chamber with the base pressure of 2×10^{-7} torr. The device structure was glass/ITO/HIL (20 nm)/EML (20 nm)/ETL/LiF(1 nm)/Al (100 nm). For D1, 15 % MoO_3 doped in CBP, 2% BrPFL-TFK doped in CBP, 60 nm thick TPBi were used as HIL, EML, ETL, respectively. For D2-a, 15 % MoO_3 doped in mCP, 2% BrPFL-TFK doped in mCP, and 60 nm thick TPBi were used as HIL, EML and ETL, respectively. A 40 nm thick BP4mPy layer was used instead of 60 nm thick TPBi as an ETL for D2-b. For D3, 15 % MoO_3 doped in mCP, 5 nm thick BrPFL-TFK, 2% BrPFL-TFK doped in PPT, 40 nm thick PPT were used as HIL, HTL, EML, ETL, respectively. Prior to LiF and Al depositions,

a molybdenum shadow mask with 2 mm diameter circles (3.14 mm^2 area opening) was placed on the sample surface to define the area of the devices. For hole-only devices, ITO was treated with UV-ozone as a substrate and 20 nm thick 15% MoO_3 doped in mCP, 5 nm-thick BrPFL-TFK, 20 nm thick *x*% BrPFL-TFK doped in PPT, 40 nm thick PPT, 10 nm thick MoO_3, and 100 nm thick Al were deposited sequentially to complete the device structure. For electron-only devices, the device structure is as follows: ITO (w/o UV-ozone treatment)/BrPFL-TFK (5 nm)/*x*% BrPFL-TFK doped in PPT (20 nm)/PPT (40 nm)/LiF (1 nm)/Al (100 nm).

Performance analysis of OLED devices: The current density-voltage-luminance (*J*-*V*-*L*) was measured by an HP 4156a semiconductor parameter analyzer attached with a FDS1010 calibrated photodiode from Thorlab, following the standard procedure of OLED measurement [20]. Electroluminescent spectra were recorded with a HR2000+ES from Ocean Optics coupled to the OLED devices via a 300 um-diameter optical fiber.

7.5. References

[1] R. Waser, “Nanoelectronics and Information Technology, 3rd Edition,” p. 1040, 2012.

[2] M. A. Baldo, M. E. Thompson, and S. R. Forrest, “High-efficiency fluorescent organic light-emitting devices using a phosphorescent sensitizer,” *Nature*, vol. 403, no. 6771, pp. 750–753, 2000.

[3] C. Adachi, M. A. Baldo, M. E. Thompson, and S. R. Forrest, “Nearly 100% internal phosphorescence efficiency in an organic light emitting device,” *J. Appl. Phys.*, vol. 90, no. 10, pp. 5048–5051, 2001.

[4] M. A. Baldo *et al.*, “Highly efficient phosphorescent emission from organic electroluminescent devices,” *Nature*, vol. 395, no. September, pp. 151–154, 1998.

[5] S. Mukherjee and P. Thilagar, “Recent advances in purely organic phosphorescent materials,” *Chem. Commun.*, vol. 51, no. 55, pp. 10988–11003, 2015.

[6] D. Chaudhuri *et al.*, “Tuning the singlet-triplet gap in metal-free phosphorescent π-conjugated polymers,” *Angew. Chemie - Int. Ed.*, vol. 49, no. 42, pp. 7714–7717, 2010.

[7] O. Bolton, K. Lee, H. J. Kim, K. Y. Lin, and J. Kim, “Activating efficient phosphorescence from purely organic materials by crystal design,” *Nat. Chem.*, vol. 3, no. 3, pp. 205–210, 2011.

[8] J. Xu, A. Takai, Y. Kobayashi, and M. Takeuchi, “Phosphorescence from a pure organic fluorene derivative in solution at room temperature,” *Chem. Commun.*, vol. 49, no. 76, p. 8447, 2013.

[9] Q. J. Shen, X. Pang, X. R. Zhao, H. Y. Gao, H.-L. Sun, and W. J. Jin, “Phosphorescent cocrystals constructed by 1,4-diiodotetrafluorobenzene and polyaromatic hydrocarbons based on C–I···π halogen bonding and other assisting weak interactions,” *CrystEngComm*, vol. 14, no. 15, p. 5027, 2012.

[10] D. Lee, O. Bolton, B. C. Kim, J. H. Youk, S. Takayama, and J. Kim, “Room temperature phosphorescence of metal-free organic materials in amorphous polymer matrices,” *J. Am. Chem. Soc.*, vol. 135, no. 16, pp. 6325–6329, 2013.

[11] W. Y. Huang, M. Y. Chang, Y. K. Han, and P. T. Huang, “Sterically encumbered poly(arylene ether)s containing spiro-annulated substituents: Synthesis and thermal properties,” *J. Polym. Sci. Part A Polym. Chem.*, vol. 48, no. 24, pp. 5872–5884, 2010.

[12] M. Kröger, S. Hamwi, J. Meyer, T. Riedl, W. Kowalsky, and A. Kahn, “P-type doping of

organic wide band gap materials by transition metal oxides: A case-study on Molybdenum trioxide," *Org. Electron.*, vol. 10, no. 5, pp. 932–938, 2009.

[13] Y. Kawamura, K. Goushi, J. Brooks, J. J. Brown, H. Sasabe, and C. Adachi, "100% phosphorescence quantum efficiency of Ir (III) complexes in organic semiconductor films," *Appl. Phys. Lett.*, vol. 86, no. 7, pp. 1–3, 2005.

[14] I. Tanaka, Y. Tabata, and S. Tokito, "Observation of phosphorescence from tris(8-hydroxyquinoline) aluminum thin films using triplet energy transfer from iridium complexes," *Phys. Rev. B - Condens. Matter Mater. Phys.*, vol. 71, no. 20, pp. 2–7, 2005.

[15] C. Adachi, M. A. Baldo, and S. R. Forrest, "Electroluminescence mechanisms in organic light emitting devices employing a europium chelate doped in a wide energy gap bipolar conducting host," *J. Appl. Phys.*, vol. 87, no. 11, pp. 8049–8055, 2000.

[16] B. S. Kim and J. Y. Lee, "Engineering of mixed host for high external quantum efficiency above 25% in green thermally activated delayed fluorescence device," *Adv. Funct. Mater.*, vol. 24, no. 25, pp. 3970–3977, 2014.

[17] S. H. Jeong and J. Y. Lee, "Dibenzothiophene derivatives as host materials for high efficiency in deep blue phosphorescent organic light emitting diodes," *J. Mater. Chem.*, vol. 21, no. 38, p. 14604, 2011.

[18] M. J. Frisch *et al.*, "Gaussian 09, revision A. 2," 2009.

[19] Z. Liu *et al.*, "Effects of gradual oxidation of aromatic sulphur-heterocycle derivatives on multilevel memory data storage performance," *J. Mater. Chem. C*, vol. 3, no. 9, pp. 2033–2039, 2015.

[20] S. R. Forrest, D. D. C. Bradley, and M. E. Thompson, "Measuring the Efficiency of Organic Light-Emitting Devices," *Adv. Mater.*, vol. 15, no. 13, pp. 1043–1048, 2003.

Chapter 8
Outlook

8.1. Roll-to-roll fabrication of all vacuum-deposited organic photovoltaics

A practical challenge for commercialization of OPVs is whether organic photovoltaics cells can be volume-manufactured at a very low cost. While considerable research has focused on polymer-based OPVs due to their amenable large area coating capability by simple spin casting, high efficiency OPVs often require a multilayer structure that are not easily achievable by spin coating because finding multiple solvents having an orthogonal solubility for polymers is always challenging as described in Section 2.1.3. In contrast, multilayer structures based on small molecular-weight organic materials have a proven record in the OLED industries for delivering a high performance through simple fabrication procedures. Following the success of small molecular-weight organic materials in OLED, roll-to-roll (R2R) processing of multilayer solar cells using a combination of VTE and OVPD could accelerate the development progress toward a low manufacturing cost of OPVs. As explained throughout Chapters 3-5, OVPD can provide a precise control of the organic thin-film morphology, a high material utilization efficiency and manufacturing yield, so as to achieve high-performance and reliable OPVs. One limitation of OVPD is a narrow range of material selectivity. Since OVPD requires an accurate temperature control inside the chamber, using various materials with a large boiling point range is rather challenging. There has been an attempt to evaporate metals in OVPD. However, because the

typical boiling point of metals is above 2000 ^{0}C, maintaining the substrate temperature low enough (<50 ^{0}C) during the deposition is turned out to be extremely difficult [1]. Thus, alternatively it is desirable to employ OVPD as a deposition system for organic materials while using VTE for evaporation of metal or metal-oxide (ex. MoO_3, Ag, Al, etc.). A schematic diagram of entire R2R sytstem combining VTE and OVPD is shown in Figure 8.1.

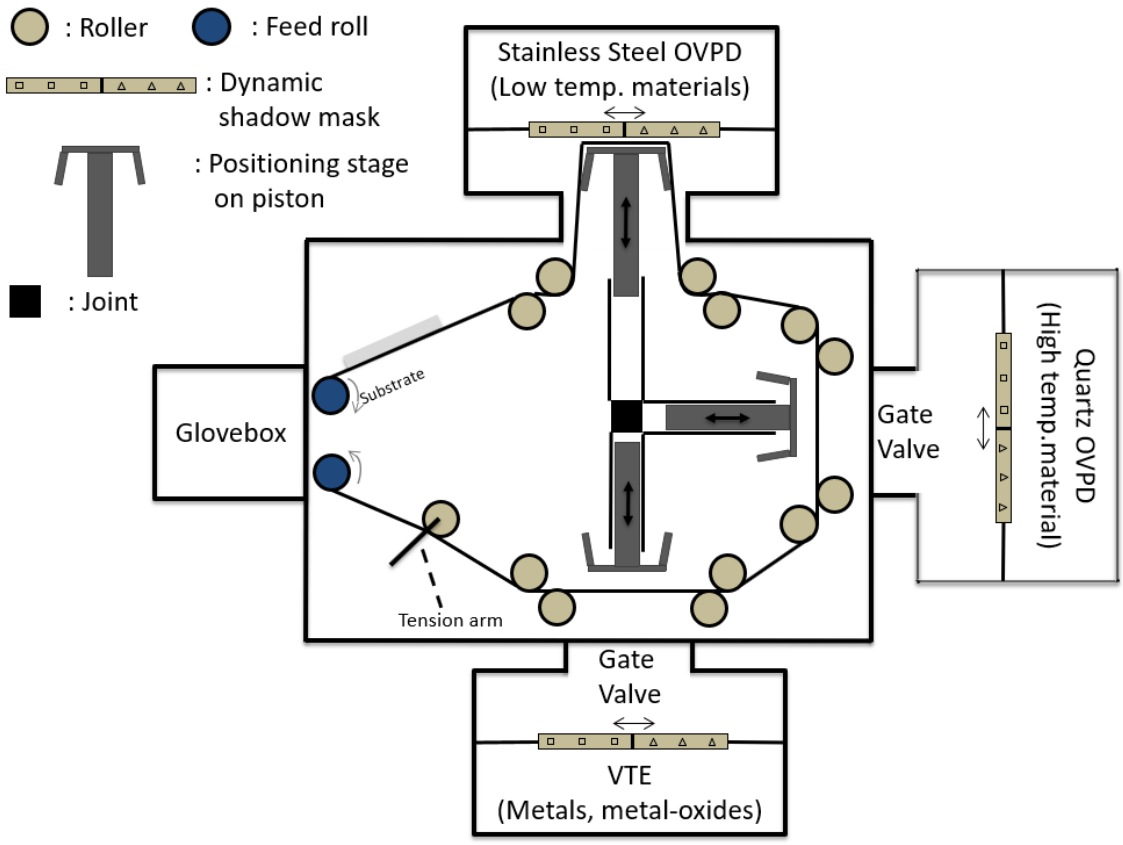

Figure 8.1. Schematic diagram of the multi-chamber R2R deposition system.

As described in the above diagram, sheets of patterned ITO on a flexible substrate are loaded into the roll-to-roll process line with a glovebox attachment. The substrate is rolled into the production line from the glovebox and it starts the roll-to-roll process by rotating the starting feed

roll. Depending on the materials needed for the device architecture, the rollers will move the substrate around the chamber to one of the three positions: the VTE for metals and metal-oxides, the quartz OVPD for high boiling point materials (350 ^{0}C ~ 500 ^{0}C) such as fullerenes, and the stainless steel OVPD for lower boiling point (< 350 ^{0}C) organic materials. The tension arm plays a role in minimizing the sheer stress when the stage is raised. Each chamber contains so called dynamic shadow masks that has multiple shadow masks in them. Between the growth chamber and the deposition tools, there are gate valves in each plane such that only one deposition tool is exposed to the substrate at a time. This allows for the proper control of the vacuum level during each processing step. A pressure of 10^{-3} torr will be used in the growth chamber when not depositing, while 10^{-1} torr is needed for OVPD deposition, and ~10^{-7} torr for VTE deposition. The connecting glovebox will be kept slightly above the atmospheric pressure of N_2, and will enable transfer of substrates and devices in and out of the growth chamber. Once the rollers position the substrate in front of the desired deposition tool, a substrate positioning stage will move the substrate into the position toward the deposition machine, where it will contact aligned shadow masks to define the deposition area. After rapid deposition of the desired material (more than 2 nm/s) to the proper layer thickness, the substrate is pulled away from the mask by the positioning stage, and can be proceeded on to the next stage. The other feed roll rotates in opposite way with the starting feed roll to move substrate back to the load/unload position next to the glovebox.

8.2. Increase lifetime of OLED employing a thick emissive layer

Although OLED technology has been a great success in lighting industries, the short operational lifetime of blue OLED still restricts realization of long-term full RGB color spectrum from OLED. Table 8.1 shows that the lifetime of blue fluorescent OLEDs is more than 10 times

shorter than that of green or red fluorescent OLEDs. The lifetime of blue phosphorescent OLED is even too short (<100 hr of T_{50}) to report based on the industrial standard. The primary reason for the short lifetime of blue OLEDs is strong exciton-polaron annihilation. Giebink et al. showed that annihilation occurred between excited excitons and polarons introduces defect formation, resulting in luminance loss and voltage rise over time [2, 3]. To reduce the exciton-polaron quenching event, graded doping concentration of guest molecules is proposed as illustrated in Figure 8.2. This strategy effectively distributes excitons uniformly within the emissive layer to lower exciton-polaron annihilation. With a 13 % (by vol.) of uniform doping concentration (D1, D2), large density of excitons is detected near the electron transporting layer (near mCBP in Figure 8.2). By gradually reducing the doping concentration of the guest from 18 % to 8 %, exciton density is more evenly distributed throughout the emissive layer. This results in the improvement

Table 8.1 OLED performance chart from Idemitsu Kosan Co, Ltd.

Color	CIE (x,y)	Efficiency (cd/A)	T_{50} (hrs)
Blue (Fluorescence)	(0.14, 0.12)	9.9	11,000
Green (Fluorescence)	(0.29, 0.64)	37	200,000
Red (Fluorescence)	(0.67, 0.33)	11	160,000
Green (Phosphorescence)	(0.33, 0.63)	64	200,000
Red (Phosphorescence)	(0.67, 0.33)	22	200,000

1) CIE and efficiency are obtained when OLED operates at 10 mA/cm^2.
2) T_{50} is the time when brightness of OLED becomes half during continuous operation. (Initial luminance is 1,000 cd/m^2)
3) Source: http://www.idemitsu.com/products/electronic/el/performance.html.

of operational lifetime of the corresponding blue phosphorescent OLED by three times [4].

Judging from the OLED degradation model based on exciton-polaron annihilation, a more intuitive and simpler way to achieve extended operational lifetime of OLED could be using a thicker emissive layer. Generally, the thickness of emissive layer is determined primarily based on charge transport properties of host and guest materials. The thickness of the emissive layer of

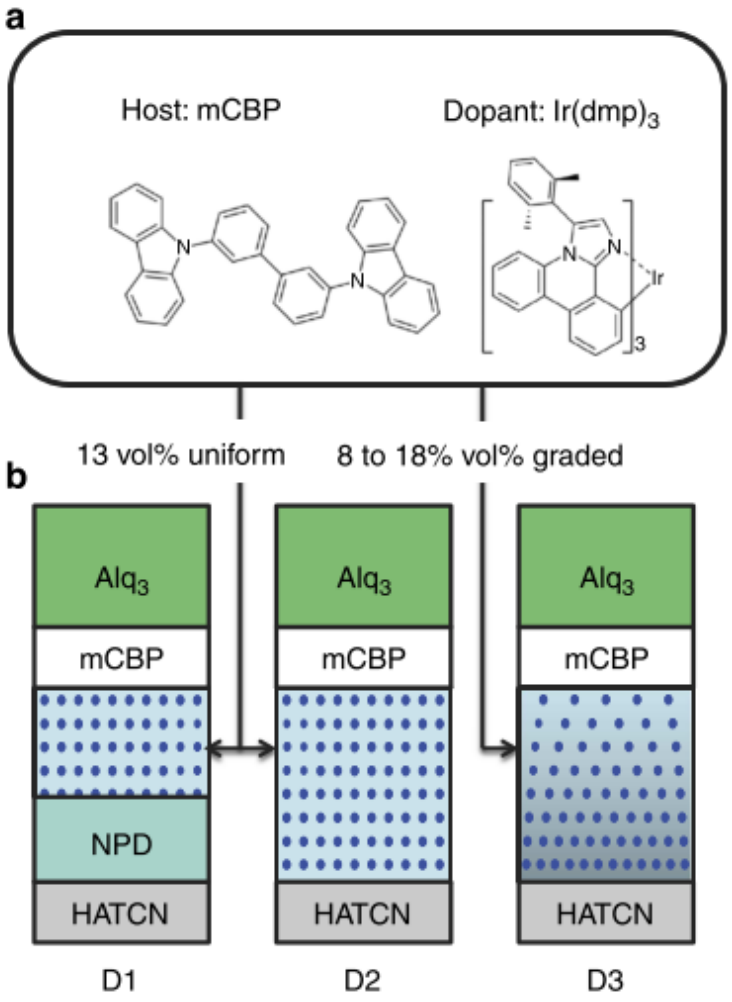

Figure 8.2. (a) Chemical structure of the host mCBP and phosphorescent guest $Ir(dmp)_3$ used in the emissive layer of the OLED. (b) Structure of the three OLEDs. HATCN, NPD, Alq_3 are used for hole injection layer, hole transporting layer, electron transporting layer, respectively. D1, D2 has 13 % of uniform doping concentration while the emissive layer of D3 has the doping concentration graded from 18 to 8 % by vol. [4].

OLEDs is typically 15-30 nm, considering charge carrier transport and optical coupling at a given wavelength of photons. In Chapter 3, we showed that charge transport in a mixed layer organic thin-film can be largely enhanced by the formation of nanocrystalline morphology via OVPD. Thus, a thicker emissive layer grown by OVPD having a better charge transport property could replace the conventional emissive layer grown by VTE. A thicker emissive layer will eventually reduce overall exciton density in the emissive layer, directly increasing operational lifetime of the OLED as the slope of luminance *vs.* time is proportional to the exciton density [2, 4]. It would give a substantial impact on the phosphorescent OLED research if blue OLEDs with an OVPD-grown emissive layer shows significant improvement in the operational lifetime.

8.3. Possible research direction in metal-free organic phosphorescent OLED

Phosphorescent OLED built with a metal-free purely organic phosphor was successfully demonstrated in Chapter 7. The efficiency of the purely organic phosphorescent OLED is limited by a low photoluminescence quantum yield of the phosphor used, BrPFL-TFK, and the long triplet lifetime in millisecond regime. One simple yet possibly challenging way to improve the performance of the OLED with purely organic phosphors is the development of organic phosphors with a high quantum yield and a fast triplet lifetime. BrPFL-TFK phosphor introduced in Chapter 7 still have a flexibility in molecular design by replacing the functional groups on the fluorene core [5]. A few examples of the modified molecular structure of BrPFL-TFK under development are shown in Figure 8.3b. Once BrPFL derivatives with a high quantum yield are available, we can re-configure the OLED structure based on the obtained device design strategies described in Chapter 7 to demonstrate a high-efficiency OLED from the purely organic phosphors.

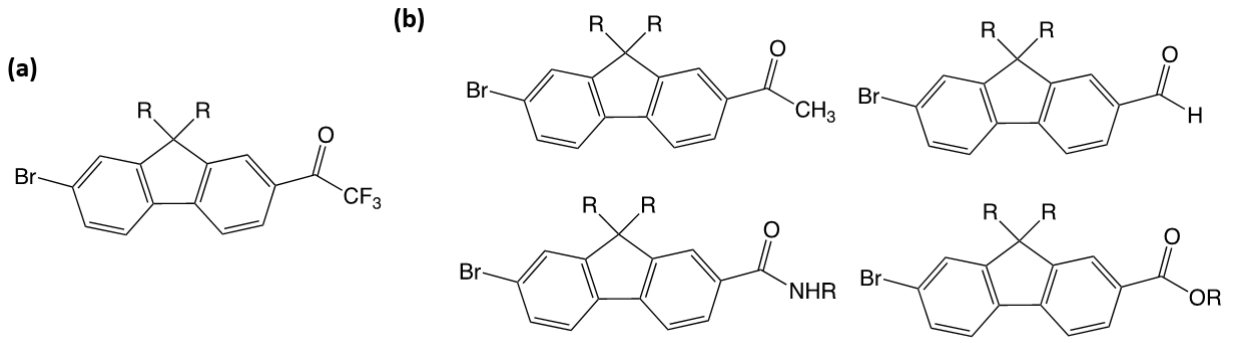

Figure 8.3. Chemical structure of (a) 1-(7-bromo-9,9-diphenyl-9H-fluoren-2-yl)-2,2,2-trifluoroethan-1-one (BrPFL-TFK) and (b) A few purely organic phosphors having the fluorene core with various functional groups. Here, R is a phenyl or an alkyl chain.

Due to the long lifetime of triplet excitons, it is expected that triplet-triplet annihilation (TTA) is a major source of the *EQE* roll-off behavior in the purely organic phosphor OLED. However, a direct evidence based on *EQE* roll-off model has not been presented yet. For organometallic compounds having a microsecond triplet lifetime, it is verified that TTA is the dominant mechanism for the *EQE*-drop at a high current density as shown in Figure 8.4 [6]. It is possible that other annihilation mechanisms such as triplet-polaron annihilation (TPA) affect significantly the *EQE* roll-off behavior since triplet excitons in the purely organic phosphor will stay much longer than those of organometallic counterparts. A similar model-fit to *EQE vs.* current density characteristics of purely organic phosphor OLEDs would be helpful to understand the fundamental mechanism of the EQE roll-off.

Appling the design strategy of the purely organic phosphors to the host material design would be another interesting research topic. The basic design strategy of the purely organic phosphors is to employ halogens in the molecular structure to enhance spin-orbit coupling, thereby enabling efficient intersystem mixing between singlets and triplets. Since the incorporation of molecules with heavy-atom effects in thermally activated delayed fluorescence (TADF) OLEDs

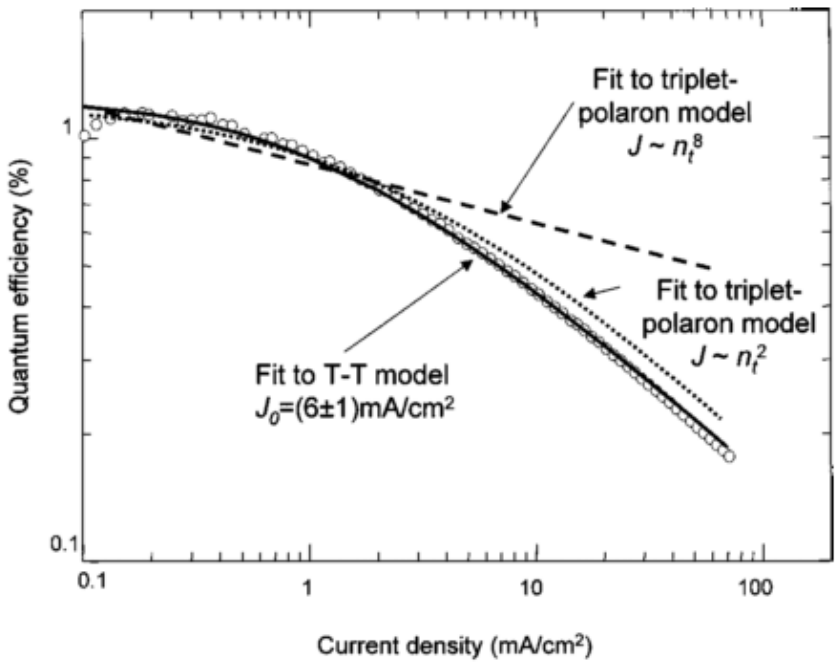

Figure 8.4. The external quantum efficiency versus current density characteristics of the $Eu(TTA)_3phen$:CBP device. The behavior of triplet-polaron quenching for bulk-limited transport ($J \propto n_t^8$) does not fit the data while triplet-polaron quenching model where $J \propto n_t^2$ gives relatively good fit. Triplet-triplet quenching model with onset current density of $J_0 = 6 \pm 1$ mA/cm^2 describes the roll-off characteristics of the device most accurately [6].

was demonstrated [7, 8], recent literature proposed a substitution of atoms in host molecules with a halogen atom Br to enhance spin-orbit coupling as shown in Figure 8.5 [9]. Although EQE of the corresponding device does not show much improvement (from 17.1 % to 17.9%), it showed a lower population of triplets owing to the increased reverse intersystem crossing rate via the heavy-atom effect. It is possible that the triplet population of a given host material is significantly reduced by applying the design rule used in the purely organic phosphors. More available singlets in host materials could be transferred to purely organic phosphor guests via Förster energy transfer mechanism, generating more radiative triplets in the organic phosphor guest in the end. In this way, phosphorescent emission from triplets of purely organic phosphors could be further increased.

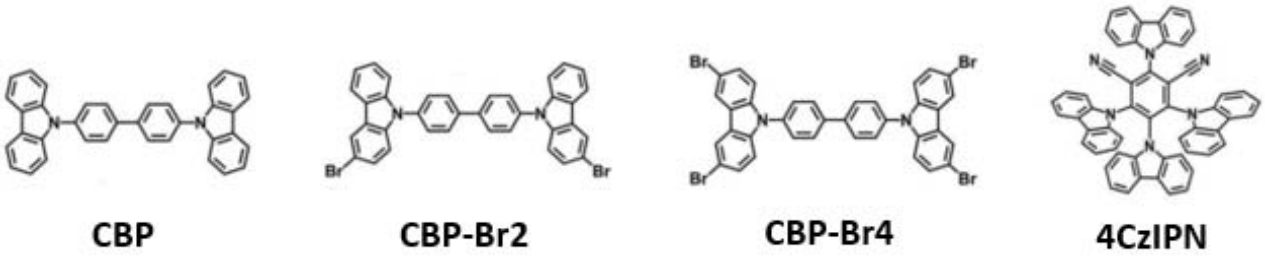

Figure 8.5**.** Molecular structure of host materials (CBP, CBP-Br2, CBP-Br4) and guest material (4CzIPN) [9].

8.4. References

[1] F. F. Navarro, P. I. Djurovich, and M. E. Thompson, "Metal deposition for optoelectronic devices using a low vacuum vapor phase deposition (VPD) system," *Org. Electron.*, vol. 15, no. 11, pp. 3052–3060, Nov. 2014.

[2] N. C. Giebink *et al.*, "Intrinsic luminance loss in phosphorescent small-molecule organic light emitting devices due to bimolecular annihilation reactions," *J. Appl. Phys.*, vol. 103, no. 4, p. 44509, 2008.

[3] N. C. Giebink, B. W. D'Andrade, M. S. Weaver, J. J. Brown, and S. R. Forrest, "Direct evidence for degradation of polaron excited states in organic light emitting diodes," *J. Appl. Phys.*, vol. 105, no. 12, 2009.

[4] Y. Zhang, J. Lee, and S. R. Forrest, "Tenfold increase in the lifetime of blue phosphorescent organic light-emitting diodes," *Nat. Commun.*, vol. 5, pp. 1–7, 2014.

[5] J. Xu, A. Takai, Y. Kobayashi, and M. Takeuchi, "Phosphorescence from a pure organic fluorene derivative in solution at room temperature," *Chem. Commun.*, vol. 49, no. 76, p. 8447, 2013.

[6] M. Baldo, C. Adachi, and S. R. Forrest, "Transient analysis of organic electrophosphorescence.II. Transient analysis of triplet-triplet annihilation," *Phys. Rev. B*, vol. 62, no. 16, pp. 10967–10977, 2000.

[7] W. Zhang, J. Jin, Z. Huang, S. Zhuang, and L. Wang, "A new way towards high-efficiency thermally activated delayed fluorescence devices via external heavy-atom effect," *Sci. Rep.*, vol. 6, no. April, pp. 1–8, 2016.

[8] D. Zhang, L. Duan, Y. Zhang, M. Cai, D. Zhang, and Y. Qiu, "Highly efficient hybrid warm white organic light-emitting diodes using a blue thermally activated delayed fluorescence emitter: exploiting the external heavy-atom effect," *Light Sci. Appl.*, vol. 4, no. 1, p. e232, 2015.

[9] M. Einzinger *et al.*, "Shorter Exciton Lifetimes via an External Heavy-Atom Effect: Alleviating the Effects of Bimolecular Processes in Organic Light-Emitting Diodes," *Adv. Mater.*, vol. 29, no. 40, pp. 1–7, 2017.